Tampere University

TIMO STOLT

Nonlinear Optics Using Resonant Metamaterials

Tampere University Dissertations 991

Tampere University Dissertations 991

TIMO STOLT

Nonlinear Optics Using Resonant Metamaterials

ACADEMIC DISSERTATION
To be presented, with the permission of
the Faculty of Engineering and Natural Sciences
of Tampere University,
for public discussion in the TB109 Auditorium
of the Tietotalo, Korkeakoulunkatu 1, Tampere,
on 22nd of March 2024, at 12 o'clock.

ACADEMIC DISSERTATION
Tampere University, Faculty of Engineering and Natural Sciences
Finland

Responsible supervisor and Custos	Professor Martti Kauranen Tampere University Finland	
Supervisor	Doctor Mikko Huttunen Tampere University Finland	
Pre-examiners	Assistant Professor Viktoriia Babicheva University of New Mexico United States	Adjoint Professor Gustavo Grinblat University of Buenos Aires Argentina
Opponent	Professor Rupert Oulton Imperial College London United Kingdom	

The originality of this thesis has been checked using the Turnitin OriginalityCheck service.

Cover design: Roihu Inc.

ISBN 978-952-03-3368-3 (print)
ISBN 978-952-03-3369-0 (pdf)
ISSN 2489-9860 (print)
ISSN 2490-0028 (pdf)
http://urn.fi/URN:ISBN:978-952-03-3369-0

HIILINEUTRAALI PAINOTUOTE
ClimateCalc CC-000025/FI
PunaMusta Printing

Carbon dioxide emissions from printing Tampere University dissertations have been compensated.

PunaMusta Oy – Yliopistopaino
Joensuu 2024

Elsa Hietalan ja Eine Stoltin muistolle.

PREFACE

This work was conducted in the Nonlinear Optics Group in the Photonics Laboratory of Tampere University. To begin, I want to acknowledge all financial supporters for enabling this research. First, I acknowledge the Photonics Research and Innovation (PREIN) Flagship project by the Research Council of Finland for covering numerous conference attendances and other networking events. Second, I thank the Emil Aaltonen Foundation for their travel grant for my research visit to France. Most importantly, I gratefully acknowledge the Jenny and Antti Wihuri Foundation and the Magnus Ehrnrooth Foundation for their doctoral research grants, which allowed me to work full-time as a doctoral researcher.

Beyond the financial support, also the personal support from supervisors and other colleagues is paramount in research. Therefore, I offer my sincere thanks to my supervisors Prof. Martti Kauranen and Dr. Mikko Huttunen. Ever since Martti hired me as a research assistant in 2016, I have always been able to rely on his guidance, support, and expertise. The biggest thanks, however, goes to Mikko. As the principal investigator for my doctoral research, he provided me with research ideas to work on, helped me to deepen my understanding of nonlinear optics and metamaterials, and made my dissertation work possible. Outside of Tampere, I want to thank Profs. Junsuk Rho and Tommi Hakala, with their respective teams, for fabricating the samples for my studies. I especially want to thank Prof. Patrice Genevet for his collaboration in various projects and for hosting me in his group in Valbonne. In addition to the big names above, I heartfully thank my colleagues in the Nonlinear Optics Group: Mrs. Anna Puumala, Ms. Madona Mekhael, Mr. Jussi Kelavuori, Ms. Kiia Arola, Mr. Niklas Järvelin, Ms. Shambhavee Annurakshita, Ms. Riya Varghese, and Dr. Ali Panah Pour. I especially want to thank Anna for her great help with the measurements and for simply being the best colleague

imaginable.

Important for good research is also a good workplace atmosphere. For this, I sincerely thank Dr. Caroline Amiot, Dr. Rafael Barros, Dr. Piotr Ryczkowski, Dr. Jan Viljanen, Mr. Kim Kalmankoski, Ms. Jiaqi Li, and all other current and former members of the SK1 gang. I thank also my other friends in Tampere for the numerous parties, fine-dine dinners, and overall good times. Especial thanks go to my dear friends Dr. Markus Hiekkamäki, Dr. Jussi Isokuortti, Dr. Tommi Mikkonen, Ms. Sofia Suomala, and Ms. Riina Ulkuniemi, whose friendship made my ten years in Tampere the great years they were.

For my entire life, I have had the luxury of unwavering support and love from my family. Both in good and bad times. For this, I am forever grateful to my mother Riitta, my father Tauno, and my brother Eero. My only wish is that my late grandmothers, Elsa and Eine, would have been here to see this day.

Finally, and most importantly, I thank my dearest fiancée Anastasiia. Your kindness, sense of humor, support, and love have made my heart feel at home. Let us now build a life and home worthy of two doctors and one overgrown little kitten.

Tampere, February 2024
Timo Stolt

ABSTRACT

Nonlinear optics is the study of the interaction between matter and intense laser light, which can result in frequency conversion and modulation of the interacting laser light. Consequently, nonlinear optical processes have enabled numerous technologies, such as frequency-tunable and pulsed laser sources. However, efficient nonlinear optical components are bulky and limited in functionality, making them unsuitable for modern photonic devices with microscopic dimensions. Recent advances in nanoscale fabrication have opened up avenues for replacing bulky nonlinear crystals with much smaller components. One example of these is metamaterials.

Metamaterials are artificial structures consisting of nanoscale building blocks, such as metal nanoparticles in plasmonic metamaterials. Through careful design of the individual building blocks, metamaterials can exhibit properties not often found in natural materials. These properties enable novel methods to boost and control optical responses of metamaterials. In particular, nonlinear responses of such structures have been heavily investigated due to their potential for flat nonlinear photonic components.

In this Thesis, novel plasmonic metamaterials for nonlinear optics were designed. The aim was to bring conventional enhancement methods of nonlinear processes, i.e., phase matching and multiply-resonant field-enhancement, to sub-wavelength metamaterials. Furthermore, the capabilities of nonlinear materials were broadened by proposing methods for tunable and broadband frequency conversion processes that are extremely difficult to realize with traditional materials. The presented findings pave the way towards tunable and multi-functional nonlinear components for a large variety of flat photonic devices.

TIIVISTELMÄ

Epälineaarinen optiikka tutkii aineen ja voimakkaan laservalon välistä vuorovaikutusta. Epälineaarisilla optisilla prosesseilla voidaan muokata vuorovaikuttavan laservalon ominaisuuksia, kuten sen aallonpituutta. Täten niitä käytetään monissa laserlaitteistoissa, kuten aallonpituudeltaan säädettävissä ja pulssitoimisissa lasereissa. Epälineaariset optiset komponentit ovat kuitenkin suurikokoisia ja toiminnalisuuksiltaan rajoittuneita, mikä rajoittaa niiden käyttöä moderneissa, mikroskooppisen kokoisissa, fotoniikan komponenteissa. Viime vuosikymmenten kehitys nanomittakaavan valmistustekniikoissa on mahdollistanut uudenlaisten mikroskooppisten komponenttien valmistuksen, joilla tulevaisuuden voidaan korvata epälineaarisia kuituja ja kiteitä fotoniikan laitteistoissa. Yksi esimerkki näistä komponenteista ovat metamateriaalit.

Metamateriaalit ovat keinotekoisia rakenteita, jotka koostuvat nanoskaalan kappaleista ja joilla voi olla ominaisuuksia, joita luonnonllisilla materiaaleilla ei ole. Näiden ominaisuuksien avulla metamateriaalien optisia vasteita voidaan vahvistaa ja muokata. Erityisesti metamateriaalien epälineaarisia ominaisuuksia on tutkittu laajalti, sillä metamateriaalit ovat varteenotettavia kandidaatteja äärimmäisen ohuiksi epälineaarisiksi optisiksi komponenteiksi.

Tässä väitöskirjassa käsitellään plamonisten metamateriaalien kehittämistä epälineaarisen optiikan tarkoituksiin. Erityisenä tavoitteena oli soveltaa perinteisiä epälineaaristen vasteiden vahvistusmenetelmiä, eli vaihesovitusta ja moniresonanttivahvistusta metamateriaaleissa. Tämän lisäksi laajensimme epälineaaristen metamateriaalinen ominaisuuksia tapauksiin, joissa niiden epälineaariset vasteet ovat säädettäviä ja laajakaistaisia, mikä on vaikea toteuttaa perinteisillä epälineaarisilla materiaaleilla. Työssä esitettyjä tuloksia voidaan vastaisuudessa hyödyntää säädeltävien ja monitoimisien epälineaaristen komponenttien kehityksessä modernin, mikrofotoniikan komponentteihin.

CONTENTS

SYMBOLS AND ABBREVIATIONS

A_b	Laser beam cross-section area
$A_j(z)$	Spatial amplitude of electric field
B_0	Scalar amplitude of magnetic-flux density
$D(\omega)$	Denominator function
E_0	Scalar amplitude of electric field
E_{far}	Far-field emission
I	Irradiance
L	Nanoparticle arm length
$L(\omega, \mathbf{r})$	Local-field corrections
L_c	Length of a nonlinear crystal
L_{coh}	Coherence length
N	Density of atoms
Q	Quality factor
S	Surface
T	Transmittance
V	Volume
Δ	Miller's delta
$\Delta\lambda$	Wavelength bandwidth
Δk	Wavevector mismatch
Λ	Poling period for a quasi-phase-matching crystal
$\chi^{(1)}$	Linear susceptibility

$\chi^{(2)}$	Second-order susceptibility
$\chi^{(n)}$	Susceptibility of nth order
δ	Resonance-induced phase shift
ϵ_0	Vacuum permittivity
γ	Damping constant
λ	Wavelength in vacuum
λ_0	Resonance wavelength
$\mathcal{P}$	Power
i	Imaginary unit
μ_0	Vacuum permeability
ν	Frequency
ν_{rep}	Repetition rate
ω	Angular frequency
ω_0	Resonance frequency
ϕ	Azimuthal angle
τ_p	Pulse duration
θ	Incidence angle
φ	Propagation-induced phase shift
$\mathbf{B}$	Magnetic-flux density
$\mathbf{B}_0$	Magnetic-flux density amplitude
$\mathbf{E}$	Electric field
$\mathbf{E}_0$	Electric field amplitude
$\mathbf{E}_{\text{inc}}$	Incident electric field
$\mathbf{E}_{\text{loc}}$	Local electric field
$\mathbf{P}$	Material polarization
$\mathbf{P}_{\text{loc}}$	Local material polarization
$\mathbf{k}$	Wave vector

$\mathbf{r}$	Position vector
$\hat{\mathbf{n}}$	Surface normal vector
$\hat{\mathbf{p}}$	Polarization vector of light
$\hat{\mathbf{t}}$	Surface tangent vector
$\hat{\mathbf{x}}, \hat{\mathbf{y}}, \hat{\mathbf{z}}$	Cartesian-coordinate unit vectors
a	Nonlinear parameter of Lorentz model
c	Speed of light
c.c.	Complex conjugate
c_0	Speed of light in vacuum
d	Nanoparticle thickness
e	Elementary charge
h	Separation layer thickness
k	Wavenumber
m_e	Mass of an electron
n	Refractive index
p	Lattice periodicity
t	Time
t	Transmission coefficient
w	Nanoparticle arm width
x, y, z	Cartesian coordinates
BC	Boundary condition
DFG	Difference-frequency generation
DG	Diffraction grating
ELA	Empty-lattice approximation
FDTD	Finite-difference time-domain
FEM	Finite element method
IR	Infrared

LP	Linear polarization
LSPR	Localized plasmon metasurface
NIR	Near-infrared
NLST	Nonlinear scattering theory
NP	Nanoparticle
OPO	Optical parametric oscillator
OSA	Optical spectrum analyzer
PBS	Polarizing beam splitter
PML	Perfectly matched layer
PMT	Photomultiplier tube
QPM	Quasi-phase-matching
RA	Rayleigh anomaly
SFG	Sum-frequency generation
SHG	Second-harmonic generation
SLR	Surface lattice resonance
THG	Third-harmonic generation
UV	Ultraviolet
VIS	Visible

ORIGINAL PUBLICATIONS

Publication I **Timo Stolt**, Jeonghyun Kim, Sébastien Héron, Anna Vesala, Younghwan Yang, Jungho Mun, Minkyung Kim, Mikko J. Huttunen, Robert Czaplicki, Martti Kauranen, Junsuk Rho, and Patrice Genevet. "Backward Phase-Matched Second-Harmonic Generation from Stacked Metasurfaces". In: *Physical Review Letters* 126 (2021), p. 033901. DOI: 10.1103/PhysRevLett.126.033901.

Publication II **Timo Stolt**, Anna Vesala, Heikki Rekola, Petri Karvinen, Tommi K. Hakala, and Mikko J. Huttunen. "Multiply-resonant second-harmonic generation using surface lattice resonances in aluminum metasurfaces". In: *Optics Express* 30.3 (2022), pp. 3620–3631. DOI: 10.1364/OE.449198.

Publication III **Timo Stolt** and Mikko J. Huttunen. "Broadband frequency conversion of ultrashort pulses using high-Q metasurface resonators". In: *New Journal of Physics* 24.2 (2022), p. 025004. DOI: 10.1088/1367-2630/ac4a14.

Author's contribution

Publication I The author carried out the experimental work with A. Vesala and handled the data analysis. The author wrote the majority of the manuscript, except the description of sample fabrication which was written by J. Kim. The manuscript was edited and proofed by all the coauthors.

Publication II The author carried out the experimental work with A. Vesala and handled the data analysis. The author wrote the major-

ity of the manuscript, except the description of sample fabrication which was written by H. Rekola. The manuscript was edited and proofed by all the coauthors.

Publication III — The author carried out all the simulations and computational work, and wrote the majority of the manuscript. M. J. Huttunen provided the research idea and helped with the writing of the manuscript.

1 INTRODUCTION

Photonics studies light–matter interactions and their applications in technology. Such studies have been a significant part of the human endeavor for millennia. Based on reflections from metal mirrors, we have modified our appearances, and lenses in telescopes have helped us to navigate the seas and gaze at the stars. Additionally, the science of light has been a matter of great interest for numerous famous scientists such as Isaac Newton and Albert Einstein, who have laid the very foundations for photonics [1, 2]. To this day, photonics remains an ever-growing field progressed by researchers such as the recent Nobel Laureates Donna Strickland and Anne L'Huillier [3, 4].

These days, our entire global society is touched by photonics. Internet is expanded across oceans and continents via laser pulses in optical fibers [5]. The information coded in these pulses can be visualized on screens made of light-emitting diodes or liquid crystals [6–8]. Sometimes, the image on the screen is unclear, and our eyesight must be aided with glasses or fixed by laser surgery. Beyond these few everyday examples, numerous fields of science rely on lasers and other optical technologies. Optical sensing is used to monitor greenhouse gases, entangled photons show promise for quantum technologies, and powerful lasers pave the path towards fusion reactors [9–13].

The foundations of many laser technologies lie in nonlinear optics [14]. It studies the interactions between matter and intense laser light, through which the optical properties of the interacting material can change [15, 16]. For example, nonlinear processes can change the refractive index for the interacting laser light, enabling large propagation lengths in optical fibers and generation of ultrashort laser pulses, via formation of solitons and the process of self-focusing [17]. Alternatively, nonlinear interaction can result in frequency conversion of laser light through processes such as the second-harmonic generation (SHG), sum-frequency generation (SFG), difference-frequency genera-

tion (DFG), and their quantum counter-part of spontaneous parametric down-conversion [18–21]. These processes can be used to realize a broad variety of light sources, varying from tunable lasers to photon pair sources [22, 23], and they allow very accurate probing of nanoscale structures and interfaces [24, 25].

Unfortunately, nonlinear optical processes are, by their very nature, extremely inefficient. To reach practical efficiency levels, conventional nonlinear optical technologies rely on phase-matching schemes that enable the coherent build-up of the nonlinear signal during propagation in a nonlinear material [26, 27]. The most efficient devices also utilize optical resonators that enhance the nonlinear interaction dramatically [28, 29]. The downside of these techniques is that they make nonlinear optical components large, energy-intensive, and limited in functionality. As a result, most nonlinear optical components are incompatible with modern microphotonic devices and poorly suited for novel technologies that would benefit from optical nonlinearities.

One promising avenue towards solving the problems listed above is to design nonlinear optical metamaterials, i.e., artificial structures consisting of subwavelength building blocks and exhibiting properties not typically found in natural materials [30]. Majority of the early work on nonlinear metamaterials focused on plasmonic metasurfaces consisting of metal nanoparticles (NPs) fabricated on a glass substrate [31]. These structures utilized relatively large surface nonlinear responses of metals, and boosted them even further through the optical response of individual metal NPs known as localized surface plasmon resonances (LSPRs). Unfortunately, LSPRs are associated with high ohmic losses, which results in low damage thresholds. This limits the achievable nonlinear conversion efficiencies, as nonlinear processes scale superlinearly with the pump laser intensities. Therefore, a lot of the recent work has focused on metamaterials where nanostructures are made of materials with low losses and high bulk nonlinearities, such as lithium niobate and gallium arsenide [32–35].

Another paradigm shift in the field of nonlinear metamaterials has been to move away from using individual nanoparticle responses, such as LSPRs and Mie-type resonances, to using collective resonances, such as surface lattice resonances (SLRs), guided-mode resonances, and bound states in the continuum [36–39]. These responses are particularly interesting for nonlinear optics, due to the associated narrow spectral features and strong local-field enhancements

that dramatically boost nonlinear responses [40–42].

1.1 Aim and Scope of This Work

This Dissertation work is in the field of nonlinear metamaterials. The work aims to progress the field by designing novel metamaterial components to both improve their current efficiencies and open new functionalities. All presented approaches rely on resonant phenomena of plasmonic structures, more speficially, on LSPRs and SLRs. The findings of this work are detailed in **Publications I**, **II**, and **III**.

In **Publication I**, the phase-engineering capabilities of plasmonic structures were utilized to achieve phase matching in stacks of evenly spaced metasurfaces. Especially, the phase shifts of optical fields induced by LSPRs of individual plasmonic NPs were utilized. Furthermore, the studied samples were designed for the non-conventional back-propagating SHG, which demonstrates the flexibility of our approach for even more complex processes.

In **Publication II**, multiply-resonant aluminum metasurfaces for SHG were designed and characterized. This work is the proof-of-principle demonstration of multiply-resonant operation based solely on SLRs. Additionally, the incident angle dependence, i.e., spatial dispersion of SLRs was utilized to modify the multiply-resonant conditions of our samples. This highlights the potential of SLR-based metasurfaces for tunable photonic components.

In **Publication III**, a metasurface-based method for frequency conversion of ultrashort laser pulses was proposed. A temporal focusing scheme, and the strong local-field enhancements and spatial dispersion of SLRs were utilized to enable broadband frequency conversion via SFG. Based on the performed simulations, this approach surpasses the time–bandwidth limit typically associated with narrowband resonators. Thus, the proposed method is applicable in addition to nonlinear optics to any optical processes involving ultrashort laser pulses.

1.2 Structure of the Thesis

This Thesis consists of 6 chapters that act as a introductory discussion for the three publications presented at the end. First, we have the introductory chapter with the more general background to photonics, nonlinear optics, and metamaterials. In Chapter 2, we discuss the theoretical background of nonlinear optics. We focus on second-order processes of SHG and SFG, and introduce phase matching as the conventional enhancement method of nonlinear responses. Chapter 3 discusses plasmonic metasurfaces and their intrinsic responses, namely, LSPRs and SLRs. We also discuss how these resonances can be used to boost nonlinear optical processes. In Chapter 4, we describe the computational and experimental methods used in this work. In Chapter 5, we summarize the results and findings of the three **Publications** in this Thesis. The sixth and final chapter before the publications themselves discusses the conclusions of the work. There, we summarize the work and take an outlook to possible future directions of this research area.

2 NONLINEAR OPTICS

Soon after the invention of laser, the field of nonlinear optics was born with the demonstration of SHG in 1961 [18]. Since then, it has been the cornerstone of numerous modern photonic technologies, ranging from simple laser pointers to high-power pulsed lasers and photon-pair sources for emerging quantum technologies [16, 43]. In this chapter, we introduce the theoretical basis for the nonlinear light–matter interactions. We especially focus on the second-order processes that form the foundation of the application examples mentioned above. We also describe how nonlinear processes are governed by phase-matching considerations. We show how phase matching can be used to build-up otherwise weak nonlinear signals to a strong-enough level for practical applications.

2.1 Vector Description of Light

Classical physics describes light as a propagating electromagnetic (EM) wave with electric and magnetic field components. Commonly, these components are described as combinations of harmonic plane waves with wavelength in vacuum λ, frequency ν, and velocity in vacuum $c_0 = \lambda\nu$. The time and space-dependent electric $\tilde{\mathbf{E}}(\mathbf{r}, t)$ and magnetic $\tilde{\mathbf{B}}(\mathbf{r}, t)$ components of such waves can be written using the following formalism:

$$\tilde{\mathbf{E}}(\mathbf{r}, t) = \mathbf{E}_0 \mathrm{e}^{\mathrm{i}(\mathbf{k}\cdot\mathbf{r}-\omega t)} + c.c.\,, \tag{2.1}$$

$$\tilde{\mathbf{B}}(\mathbf{r}, t) = \mathbf{B}_0 \mathrm{e}^{\mathrm{i}(\mathbf{k}\cdot\mathbf{r}-\omega t)} + c.c.\,, \tag{2.2}$$

where $\mathbf{E}_0$ and $\mathbf{B}_0$ are the amplitudes of electric and magnetic field components, respectively, $\mathbf{k}$ is the wave vector, $\mathbf{r}$ is the position vector, $\omega = 2\pi\nu$ is the angular frequency, t is time, i is the imaginary unit, and *c.c.* denotes the complex conjugate. The tilde ($\tilde{}$) notation on $\tilde{\mathbf{E}}(\mathbf{r}, t)$ and $\tilde{\mathbf{B}}(\mathbf{r}, t)$ marks the fact that they vary rapidly in time. We note here that $\mathbf{k} \cdot \mathbf{r} - \omega t$ describes the phase of the

EM wave, which is of paramount importance for numerous optical processes, including nonlinear interactions, as we will especially see when discussing phase matching.

We start our analysis with $\mathbf{k}$ which defines the propagation direction of the EM wave. It is written in term of its Cartesian components k_x, k_y, and k_z as

$$\mathbf{k} = k_x\hat{\mathbf{x}} + k_y\hat{\mathbf{y}} + k_z\hat{\mathbf{z}}\,, \tag{2.3}$$

where $\hat{\mathbf{x}}$, $\hat{\mathbf{y}}$, and $\hat{\mathbf{z}}$ are the unit vectors along the Cartesian coordinates. The magnitude of $\mathbf{k}$, i.e., the wavenumber k, is connected to the Cartesian components and λ by

$$k = |\mathbf{k}| = \sqrt{k_x^2 + k_y^2 + k_z^2} = \frac{2\pi}{\lambda}n\,, \tag{2.4}$$

where n is the refractive index of the surrounding medium.

Next, we look into the oscillation direction of the electric and magnetic field components, starting with the electric field. We can define that the amplitude vector of the electric field is given by the equation

$$\mathbf{E}_0 = E_0\hat{\mathbf{p}}, \tag{2.5}$$

where E_0 is the scalar amplitude of the electric field and $\hat{\mathbf{p}}$ is the unit vector that defines the oscillation direction of the electric field, i.e., the polarization of the EM wave.

In homogeneous media, plane waves do not diverge ($\boldsymbol{\nabla}\cdot\tilde{\mathbf{E}}) = 0$). From this we can get that

$$\boldsymbol{\nabla}\cdot\tilde{\mathbf{E}} = \mathrm{i}\mathbf{k}\cdot\tilde{\mathbf{E}} = 0\,. \tag{2.6}$$

This means that the electric field of an electromagnetic plane wave is perpendicular to the propagation direction (see Fig 2.1). Consequently, $\hat{\mathbf{p}}$ is also perpendicular to $\mathbf{k}$, and thus, the electric field oscillates on the plane that is orthogonal to the propagation direction (see Fig. 2.1 a). The most common type of such polarization is linear polarization (LP), where the electric field oscillates along a single line on the aforementioned plane (see Fig. 2.1 b). We note that many other polarization types, such as azimuthal, radial, and circular polarization exist, and that they are very important for various technologies. However, in all research done for this Thesis, we used only linearly polarized

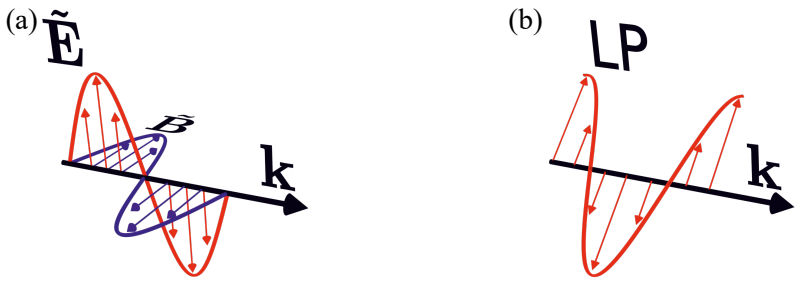

Figure 2.1 (a) Light can be described as combinations of electromagnetic plane waves, for which, the electric field component $\tilde{\mathbf{E}}$ and magnetic field component $\tilde{\mathbf{B}}$ are orthogonal to the wave propagation direction, described by wave vector $\mathbf{k}$. (b) For linearly polarized light, $\tilde{\mathbf{E}}$ oscillates along a single line.

light. Therefore, we assume linearly polarized light in the forthcoming discussion.

From well-known Maxwell's equations [44], the connection between plane-wave like $\tilde{\mathbf{B}}(\mathbf{r},t)$ and $\tilde{\mathbf{E}}(\mathbf{r},t)$ can be derived to be

$$\tilde{\mathbf{B}}(\mathbf{r},t) = \frac{\mathbf{k}}{\omega} \times \tilde{\mathbf{E}}(\mathbf{r},t)\,. \tag{2.7}$$

The equation above illustrates that electric and magnetic field components are perpendicular to each other and also to the propagation direction. In other words, this means that planar EM waves are transverse waves (see Fig. 2.1 a). Furthermore, the magnitudes of the electric and magnetic field components are connected by the equation

$$\left|\tilde{\mathbf{B}}(\mathbf{r},t)\right| = B_0 = \frac{n}{c_0} E_0\,. \tag{2.8}$$

We can now write an equation for the irradiance, i.e., the average power per unit area carried by the EM wave. Commonly it is given as [45]

$$I = \left\langle c_0^2 \epsilon_0 \left| \tilde{\mathbf{E}}(\mathbf{r},t) \times \tilde{\mathbf{B}}(\mathbf{r},t) \right| \right\rangle_T = \frac{n c_0 \epsilon_0}{2} |E_0|^2\,, \tag{2.9}$$

where $\langle\,\rangle_T$ is the temporal average. Equation above connects the power of the EM wave to E_0, allowing us to neglect the magnetic components and focusing on the electric field components in our following derivations. This selection is valid for most of cases, as the magnetic interactions typically have negligible

impact on the overall light–matter interactions.

2.2 Nonlinear Material Response

When light propagates through a material, it induces an electric polarization field $\tilde{\mathbf{P}}(\mathbf{r},t)$ inside the material. With the commonly valid assumption of current-free and non-magnetic material, we can write a general wave equation for such situation as

$$\nabla^2\tilde{\mathbf{E}}(\mathbf{r},t) = \frac{1}{c_0^2}\frac{\partial^2\tilde{\mathbf{E}}(\mathbf{r},t)}{\partial t^2} + \mu_0\frac{\partial^2\tilde{\mathbf{P}}(\mathbf{r},t)}{\partial t^2}\,, \tag{2.10}$$

where μ_0 is the vacuum permeability.

With weak incident light, we can assume that $\tilde{\mathbf{P}}(\mathbf{r},t)$ is linearly dependent on the interacting electric field and given by the following convolution integral [15]

$$\tilde{\mathbf{P}}(\mathbf{r},t) = \epsilon_0\int_{-\infty}^{\infty}\int_{-\infty}^{\infty}\chi^{(1)}(\mathbf{r}-\mathbf{r}',t-t')\cdot\tilde{\mathbf{E}}(\mathbf{r}-\mathbf{r}',t-t')d\mathbf{r}'dt'\,, \tag{2.11}$$

where $\chi^{(1)}(\mathbf{r},t)$ is the linear susceptibility.

Often, the different field components are considered in terms of $\mathbf{k}$ and ω, rather than in terms of $\mathbf{r}$ and t. In other words, the electric field is considered as $\mathbf{E}(\mathbf{k},\omega)$ and the susceptibility as $\chi^{(1)}(\mathbf{k},\omega)$, which can be calculated from the $\tilde{\mathbf{E}}(\mathbf{r},t)$ and $\chi^{(1)}(\mathbf{r},t)$ through Fourier transformations. Similarly, we can use Fourier transforms and the convolution theorem to get the material polarization as

$$\mathbf{P}(\mathbf{k},\omega) = \epsilon_0\chi^{(1)}(\mathbf{k},\omega)\cdot\mathbf{E}(\mathbf{k},\omega)\,. \tag{2.12}$$

To simplify our following procedure, we make the common assumption that $\chi^{(1)}$ is independent on $\mathbf{r}$ and $\mathbf{k}$. Thus, we only consider the quantities t and ω from now on.

By inserting the $\mathbf{P}(\omega)$ in to Eq. (2.10), we can solve for the speed of light in an optical material as

$$c = \frac{1}{\sqrt{\epsilon_0\mu_0}}\frac{1}{\sqrt{1+\chi^{(1)}(\omega)}} = \frac{c_0}{n(\omega)}, \tag{2.13}$$

where we have defined $n(\omega) = \sqrt{1+\chi^{(1)}(\omega)}$ as the refractive index of the mate-

rial. The ω dependence of n is commonly known as refractive index dispersion.

With strong enough incident light, the linear assumption in Eq. (2.11) becomes inadequate, and the material polarization has to be considered as a power series of higher-order components:

$$\begin{aligned}\tilde{\mathbf{P}}(t) =&\epsilon_0\Bigg(\int_{-\infty}^{\infty}\chi^{(1)}(t-t')\cdot\tilde{\mathbf{E}}(t-t')dt' \\ &+\int_{-\infty}^{\infty}\chi^{(2)}(t-t_1;t-t_2):\tilde{\mathbf{E}}(t_1)\tilde{\mathbf{E}}(t_2)dt_1dt_2 \\ &+\int_{-\infty}^{\infty}\chi^{(3)}(t-t_1;t-t_2;t-t_3)\vdots\tilde{\mathbf{E}}(t_1)\tilde{\mathbf{E}}(t_2)\tilde{\mathbf{E}}(t_2)dt_1dt_2dt_3+\cdots\Bigg),\end{aligned} \tag{2.14}$$

where $\chi^{(2)}$ and $\chi^{(3)}$ are the second- and third-order susceptibilities, respectively.

By performing Fourier transformations to the equation above, we can write $\mathbf{P}(\omega)$ as the sum of different frequency components as

$$\mathbf{P}(\omega)=\mathbf{P}^{(1)}(\omega)+\mathbf{P}^{(2)}(\omega)+\mathbf{P}^{(3)}(\omega)+\cdots \tag{2.15}$$

In the equation above, $\mathbf{P}^{(1)}(\omega)$ is given by Eq. (2.12), while

$$\mathbf{P}^{(2)}(\omega)=\epsilon_0\chi^{(2)}(\omega=\omega_1+\omega_2):\mathbf{E}(\omega_1)\mathbf{E}(\omega_2) \tag{2.16}$$

is the second-order nonlinear polarization component, and

$$\mathbf{P}^{(3)}(\omega)=\epsilon_0\chi^{(3)}(\omega=\omega_1+\omega_2+\omega_3)\vdots\mathbf{E}(\omega_1)\mathbf{E}(\omega_2)\mathbf{E}(\omega_3) \tag{2.17}$$

is the third-order nonlinear polarization component. We note that the frequencies ω_i can also have negative signs for nonlinear processes such as DFG.

Equations (2.16) and (2.17) describe how second-order and third-order nonlinear responses correspond to three-wave-mixing and four-wave-mixing processes, respectively. In such processes, multiple EM waves participate in the light–matter interaction in a nonlinear manner, allowing unique modifications of interacting optical fields. For example, both second- and third-order interactions can result in changes in the refractive index of the nonlinear material that the incident laser light experiences. In this Thesis, however, we focus on second-order effects that are more commonly used in frequency conversion

processes.

2.3 Second-order Nonlinear Responses

As mentioned in the previous section, second-order nonlinear optical processes involve three interacting waves. We shall now consider a situation, where the incident electric field has two frequency components, and is therefore given by

$$\mathbf{E} = \mathbf{E}_1 \mathrm{e}^{-\mathrm{i}\omega_1 t} + \mathbf{E}_2 \mathrm{e}^{-\mathrm{i}\omega_2 t} + c.c. \tag{2.18}$$

The second-order polarization is then given by

$$\mathbf{P}^{(2)} = \epsilon_0 \chi^{(2)} \mathbf{E}^2, \tag{2.19}$$

and also as a sum of its frequency components:

$$\mathbf{P}^{(2)} = \sum_n \mathbf{P}(\omega_n) e^{-\mathrm{i}\omega_n t}\,. \tag{2.20}$$

Here, the various second-order polarization components can be written as [16]

$$\mathbf{P}^{(2)}(2\omega_1) = \epsilon_0 \chi^{(2)}(2\omega_1; \omega_1, \omega_1) : \mathbf{E}_1^2\,, \tag{2.21}$$

$$\mathbf{P}^{(2)}(2\omega_2) = \epsilon_0 \chi^{(2)}(2\omega_2; \omega_2, \omega_2) : \mathbf{E}_2^2\,, \tag{2.22}$$

$$\mathbf{P}^{(2)}(\omega_1 + \omega_2) = 2\epsilon_0 \chi^{(2)}(\omega_1 + \omega_2; \omega_1, \omega_2) : \mathbf{E}_1 \mathbf{E}_2\,, \tag{2.23}$$

$$\mathbf{P}^{(2)}(\omega_1 - \omega_2) = 2\epsilon_0 \chi^{(2)}(\omega_1 - \omega_2; \omega_1, -\omega_2) : \mathbf{E}_1 \mathbf{E}_2^*\,, \tag{2.24}$$

$$\mathbf{P}^{(2)}(0) = 2\epsilon_0 \left(\chi^{(2)}(0; \omega_1, -\omega_1) : \mathbf{E}_1 \mathbf{E}_1^* + \chi^{(2)}(0; \omega_2, -\omega_2) : \mathbf{E}_2 \mathbf{E}_2^* \right)\,. \tag{2.25}$$

The complex conjugates are connected to the frequency components with negative frequencies by $\mathbf{E}^*(\omega) = \mathbf{E}(-\omega)$. Therefore, we do not write down the negative frequency counterparts of Eqs. (2.21)–(2.24), as they are the complex conjugates of the shown frequency components.

$\mathbf{P}^{(2)}(0)$ corresponds to optical rectification, a process where a static electric field is created into the medium. The other four polarization components in Eqs. (2.21)–(2.24) correspond to the physical processes where new frequency components are created. $\mathbf{P}^{(2)}(2\omega_1)$ and $\mathbf{P}^{(2)}(2\omega_2)$ correspond to SHG, $\mathbf{P}^{(2)}(\omega_1+$

ω_2) to SFG, and $\mathbf{P}^{(2)}(\omega_1 - \omega_2)$ to DFG. Even though DFG is commonly used in many laser devices, such as optical parametric oscillators (OPOs), we focus here on SHG, and its non-degenerate version SFG.

2.3.1 Second-harmonic Generation

SHG is a nonlinear optical process during which energy from two waves oscillating at frequency ω is partially converted to a signal wave oscillating at a doubled frequency 2ω (see Fig. 2.2 a). Its polarization components are given by

$$P_i(2\omega) = \epsilon_0 \sum_{jk} \chi^{(2)}_{ijk}(2\omega;\omega,\omega) E_j(\omega) E_k(\omega)\,, \tag{2.26}$$

where indices i, j, and k correspond to the Cartesian components. Very often the two incident fields for the process of SHG are from the same light source and are in the same polarization state, i.e., $j = k$. In such a case, Eq. (2.26) simplifies into

$$P_i(2\omega) = \epsilon_0 \chi^{(2)}_{ijj}(2\omega;\omega,\omega) E^2_j(\omega). \tag{2.27}$$

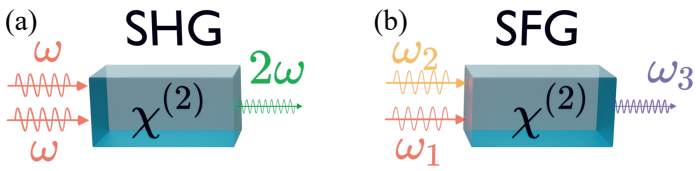

Figure 2.2 (a) During second-harmonic generation (SHG), two pump photons with frequency ω are annihilated and a signal photon with the doubled frequency 2ω is generated. (b) Sum-frequency generation (SFG) is the non-degenerate version of SHG, where the two incident photons have different frequencies ω_1 and ω_2, and the generated signal photon has the summed frequency ω_3.

The simplicity of SHG associated with $P_i(2\omega)$ in Eq. (2.27) explains why it was SHG that was the first realized frequency conversion process [18]. It also demonstrates why SHG is most convenient for converting infrared (IR) laser light into the visible (VIS) region [16, 46]. Furthermore, the irradiance of the SHG field is proportional to the square of the absolute value of $P_i(2\omega)$ (which holds for any process where polarization acts as a source of radiation):

$$I_i(2\omega) \propto |P_i(2\omega)|^2 \propto \left|\chi^{(2)}_{ijj}(2\omega;\omega,\omega)\right| I^2(\omega). \tag{2.28}$$

The equation above tells us also that the emitted SH power depends quadratically on the power of the pump beam. This illustrates the fact that nonlinear processes scale with higher powers of the incident power, resulting in stronger nonlinear optical responses when pulsed laser light with large peak intensity is used. In addition, the quadratic power dependence is a key characteristic of SHG, and it is thus commonly used to confirm that the detected signal is indeed of second-order origin [47–50].

2.3.2 Sum-frequency Generation

SFG is the non-degenerate version of SHG, where the two incident fields oscillate at different frequencies ω_1 and ω_2 and the signal field oscillates at the sum frequency $\omega_3 = \omega_1 + \omega_2$ (see Fig. 2.2 b). It corresponds to $\mathbf{P}(\omega_3)$, given by Eq. (2.23), for which the Cartesian components are given by

$$P_i(\omega_3 = \omega_1 + \omega_2) = \epsilon_0 \sum_{jk} \sum_{(1,2)} \chi^{(2)}_{ijk}(\omega_3; \omega_1, \omega_2) E_j(\omega_1) E_k(\omega_2)\,. \tag{2.29}$$

Consequently, the SFG irradiance becomes

$$I_i(\omega_3) \propto |P_i(\omega_3)|^2 \propto \left|\chi^{(2)}_{ijk}(\omega_3; \omega_1, \omega_2)\right| I(\omega_1) I(\omega_2). \tag{2.30}$$

Similar to SHG, SFG is also used for up-conversion of IR and VIS region laser light [16]. Especially, SFG is used to realize wavelength-tunable laser sources, by having a tunable IR laser and a wavelength-fixed IR laser as inputs. Additionally, subsequent SFG and SHG processes can be used to frequency-triple laser light [46, 51, 52]. This process is also known as cascaded third-harmonic generation (THG), and it can be used to convert IR laser light into the ultraviolet (UV) region.

2.4 Second-order Susceptibility

We now look into the properties of the second-order susceptibilities. For simplicity, we consider the SFG susceptibility $\chi^{(2)}(\omega_3; \omega_1, \omega_2)$ in a lossless medium. With this approach, we define the typical symmetry and birefringence aspects for nonlinear materials, and provide order-of-magnitude estimations for non-

linear susceptibilities. We note that the following considerations are valid for other second-order, and furthermore, all even-order nonlinear optical processes.

2.4.1 Second-order Responses in Centrosymmetric Materials

Second-order processes, as any even-order nonlinear processes, are highly impacted by the structural symmetry of the nonlinear material. To illustrate this impact, we consider the general case of SHG in a centrosymmetric material, given by

$$\mathbf{P}(2\omega) = \epsilon_0 \chi^{(2)}(2\omega;\omega,\omega)\mathbf{E}^2(\omega)\,. \tag{2.31}$$

The spatial inversion $\mathbf{r} \to -\mathbf{r}$ changes the signs of both $\mathbf{E}(\omega)$ and $\mathbf{P}^{(2)}(2\omega)$. By investigating the nonlinear polarization, we find that

$$-\mathbf{P}(2\omega) = \epsilon_0 \chi^{(2)}(2\omega;\omega,\omega)(-\mathbf{E})^2(\omega) = \epsilon_0 \chi^{(2)}(2\omega;\omega,\omega)\mathbf{E}^2(\omega) = \mathbf{P}(2\omega)\,, \tag{2.32}$$

which is true only if $\chi^{(2)}(2\omega;\omega,\omega) = 0$, indicating that centrosymmetric materials do not exhibit second-order nonlinear responses. Therefore, the conventional second-order nonlinear materials, such as lithium niobate ($LiNbO_3$) and beta barium borate (β-BaB_2O_4, BBO), have crystal structures with broken inversion symmetry.

2.4.2 Miller's Rule

One approach to describe optical properties of materials is to use the Lorentz atom model [53]. It describes the linear susceptibility as

$$\chi^{(1)}(\omega) = \frac{N(e^2/m_e)}{\epsilon_0 D(\omega)}, \tag{2.33}$$

where N is the atomic number density of the material, while e and m_e are the charge and mass of an electron. The denominator function $D(\omega)$ is given by

$$D(\omega) = \omega_0^2 - \omega^2 - 2i\omega\gamma, \tag{2.34}$$

where ω_0 is the resonance frequency of the material and γ is the damping constant of the resonance.

With the equations above we can make an order-of-magnitude estimations for $\chi^{(1)}$ in typical lossless optical materials. We assume that $N \sim 1/d^3$, where $d \approx 3\,\text{Å}$ is the separation between atoms in the material. Second, we assume non-resonant conditions, i.e., $\omega_0 \gg \omega$, where $D(\omega) \approx \omega_0^2$ and making $\chi^{(1)}(\omega)$ positive and real-valued. By using typical solid matter values $e = 1 \times 10^{-19}\,\text{C}$, $m_e = 9.1 \times 10^{-31}\,\text{kg}$, and $\omega_0 \approx 1 \times 10^{16}\,\text{rad/s}$, we get that

$$\chi^{(1)}(\omega) = \frac{e^2}{\epsilon_0 m_e \omega_0^2 d^3} \approx 1.2\,. \tag{2.35}$$

This results in a refractive index value of $n(\omega) = \sqrt{1 + \chi^{(1)}(\omega)} \approx 1.5$, which is in accordance with the measured refractive indices for typical optical glasses.

The Lorentz model can be generalized to describe also the nonlinear susceptibilities. Particularly, the second-order susceptibility is given by

$$\chi^{(2)}(\omega_3; \omega_1, \omega_2) = \frac{N(e^3/m_e^2)a}{\epsilon_0 D(\omega_1) D(\omega_2) D(\omega_3)}, \tag{2.36}$$

where a is a nonlinear parameter for the Lorentz model [16]. Comparing Eqs. (2.33) and (2.36) allows us to rewrite the second-order susceptibility in terms of linear susceptibilities as

$$\chi^{(2)}(\omega_3; \omega_1, \omega_2) = \frac{\epsilon_0^2 m_e a}{N^2 e^3} \chi^{(1)}(\omega_3) \chi^{(1)}(\omega_1) \chi^{(1)}(\omega_2). \tag{2.37}$$

From the equation above we can define *Miller's delta* [54]

$$\Delta = \frac{\epsilon_0^2 m a}{N^2 e^3} = \frac{\chi^{(2)}(\omega_3; \omega_1, \omega_2)}{\chi^{(1)}(\omega_3) \chi^{(1)}(\omega_1) \chi^{(1)}(\omega_2)}, \tag{2.38}$$

which is nearly constant for most solids.

We can use the Miller's rule in Eq. (2.38) to estimate the magnitude of the second-order susceptibility. Similar to the order-of-magnitude estimations of $\chi^{(1)}(\omega)$, we again assume an off-resonant conditions in a typical optical material and that $a \sim \frac{\omega_0^2}{d}$. Now, we get that

$$\chi^{(2)}(\omega_3; \omega_1, \omega_2) = \frac{e^3}{\epsilon_0 m_e^2 \omega_0^4 d^4} \approx 6.9\,\text{pm/V}, \tag{2.39}$$

which agrees well with measured susceptibility values for common nonlinear crystals [16].

The first conclusion from the discussion above, is that in lossless nonlinear materials, second-order nonlinearities are extremely weak. This can be seen from the ratio between the linear and second-order polarization magnitudes given by

$$\frac{P^{(2)}}{P^{(1)}} = \frac{\chi^{(2)}}{\chi^{(1)}} E \approx 5.8 \times 10^{-12}\,\mathrm{m/V}E \tag{2.40}$$

For $P^{(2)}$ to have as strong contribution as the linear polarization, the incident electric field should have an amplitude of $E \approx 1.7 \times 10^{11}\,\mathrm{V/m}$ corresponding to $I \approx 6\,\mathrm{PW/cm^2}$. Such irradiance levels can be achieved only with extremely powerful pulsed lasers, and would be destructive for majority of common optical materials. Furthermore, in such extreme conditions, the material responses could not be described with the perturbative power series in Eq. (2.14).

The second conclusion from Miller's rule is that highly refractive materials have larger $\chi^{(2)}$. This is due to the fact, that materials get more refractive near resonant conditions ($\omega \rightarrow \omega_0$), where $D(\omega)$ decreases and $\chi^{(1)}(\omega)$ increases. Naturally, $\chi^{(2)}$ reaches its maximum value under resonant conditions ($\omega = \omega_0$), which is commonly exploited to enhance nonlinearities in nanoscale materials [31, 55]. Although material resonances increase $\chi^{(2)}$, they also induce considerable losses limiting the overall nonlinear responses. Therefore, conventional nonlinear optical devices are based on highly transparent materials and compensate for the weak nonlinearities with phase-matching techniques (see below) and optical resonators.

2.4.3 Birefringence and Second-order Susceptibilities

Similar to nonlinear susceptibilities, also the linear susceptibility $\chi^{(1)}(\omega)$ is a tensor. Particularly, it is a second-rank tensor, for which the tensor components $\chi^{(1)}_{ij}(\omega)$ connect $\mathbf{E}(\omega)$ to $\mathbf{P}^{(1)}(\omega)$. Accordingly, the linear material polarization components can be written as

$$P^{(1)}_i(\omega) = \epsilon_0 \sum_j \chi^{(1)}_{ij}(\omega) E_j(\omega). \tag{2.41}$$

Now, the refractive index of the material along the ith component of $\mathbf{P}^{(1)}(\omega)$, with the incident field along the direction j, can be solved as

$$n_i(\omega) = \sqrt{1 + \chi_{ij}^{(1)}(\omega)}. \tag{2.42}$$

In the case of non-magnetic materials, $\chi^{(1)}(\omega)$ can be diagonalized, i.e., $\chi_{ij}^{(1)} = 0$ for $i \neq j$. For example, this property is associated with uniaxial materials, for which the refractive index becomes

$$n_i(\omega) = \sqrt{1 + \chi_{ii}^{(1)}(\omega)}. \tag{2.43}$$

From the equations above, we can see that for an anisotropic material, the refractive index depends on the polarization of incident light. This property is commonly known as birefringence.

Anisotropy has impact also on the nonlinear properties of the material. First off all, the fact whether $\chi_{ijk}^{(2)}$ is zero or not depends on both material symmetry properties (arising from its crystalline structure) and the polarization of the interacting fields [16]. Consequently, second-order processes are commonly divided into three types in terms of polarization states: type 0, type I, and type II (see Fig. 2.3). In type 0, all three interacting fields have the same polarization. For such processes, the relevant susceptibility component is $\chi_{iii}^{(2)}$. In type I, two incident fields have the same polarization which is orthogonal to the polarization of the nonlinear signal field. Consequently, the relevant susceptibility component for type I processes is $\chi_{ijj}^{(2)}$. Finally, the type II processes have the two incident fields associated with orthogonal polarizations with respect to each other, while the signal field polarization is aligned with one of the incident field polarizations. The relevant susceptibility components for type II processes therefore are $\chi_{iji}^{(2)}$ and $\chi_{iij}^{(2)}$.

Birefringence also affects the magnitude of the nonzero tensor components through Miller's rule. For example, uniaxial crystals have Miller's delta written as

$$\Delta_{ijk} = \frac{\chi_{ijk}^{(2)}(\omega_3; \omega_1, \omega_2)}{\chi_{ii}^{(1)}(\omega_3)\chi_{jj}^{(1)}(\omega_1)\chi_{kk}^{(1)}(\omega_2)}. \tag{2.44}$$

From the equation above, it is now obvious that the nonlinear response of the material depends on both dispersion and birefringence, i.e., the frequency- and

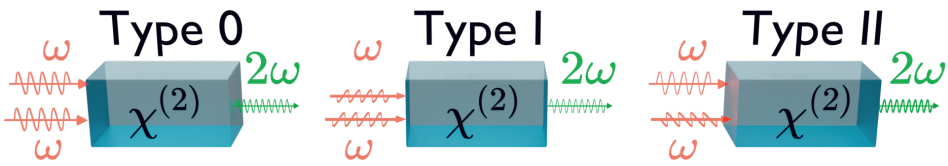

Figure 2.3 Three types of second-order processes in terms of polarization states of the three interacting waves. In type 0 processes, all interacting waves have the same polarization. In type I processes, the two fundamental waves have the same polarization which is orthogonal to the signal polarization. In type II processes, the two fundamental waves are orthogonally polarized.

polarization-dependence of the refractive indices at the interacting frequencies.

2.4.4 Second-order Susceptibility of Interfaces

In addition to anisotropic crystal structures, inversion symmetry breaks also at interfaces between two optically different materials [56]. Therefore, SHG and SFG are often used to investigate surface properties [24, 25, 57, 58]. To illustrate this point further, we consider interfaces on the xy-plane, for which the nonlinear processes are associated with surface susceptibilities $\chi^{(2)}_{\text{surf}}$. We focus here on two types of interfaces. The first type is an isotropic interface ($C_{\infty v}$ symmetry class). The second type is an interface with the yz-plane as its only mirror plane, i.e., an interface belonging to the C_{1v} symmetry class.

For an isotropic interface, the inversion symmetry is broken only along the z-axis, i.e., the surface normal. For such interfaces, the nonzero tensor components of $\chi^{(2)}_{\text{surf}}$ are $\chi^{(2)}_{xxz} = \chi^{(2)}_{xzx} = \chi^{(2)}_{yyz} = \chi^{(2)}_{yzy}$, $\chi^{(2)}_{zxx} = \chi^{(2)}_{zyy}$, and $\chi^{(2)}_{zzz}$. For a non-zero second-order response, it is thus required that at least one of the interacting fields has components along the z-axis. This results in the fact that isotropic interfaces do not have responses with normally incident pump and signal fields, but with non-zero pump or signal propagation angles, the response becomes nonzero.

For anisotropic interfaces, the inversion symmetry is broken along to the mirror planes. For such plane, second-order processes do not anymore require nonzero incidence angles. For the C_{1v} symmetry class interfaces, the yz-plane is the mirror plane, and the nonzero tensor components for pump and signal field propagating along the z-axis are $\chi^{(2)}_{yyy}$, $\chi^{(2)}_{yxx}$, and $\chi^{(2)}_{xxy} = \chi^{(2)}_{xyx}$. We list all

the nonzero tensor components for an isotropic and a C_{1v} interface in Table 2.1.

Symmetry class	Mirror plane	Independent nonzero elements
Isotropic ($C_{\infty v}$)		$xxz = xzx = yzy = yyz$, $zxx = zyy$, zzz
C_{1v}	yz-plane	yyy, yxx, $xxy = xyx$, $yyz = yzy$, $xxz = xzx$, zyy, zxx, yzz, $zyz = zzy$, zzz

Table 2.1 Independent nonzero $\chi^{(2)}_{\mathrm{surf}}$ components for an isotropic interface and an interface belonging to the C_{1v} symmetry class [56]. Both interfaces are along the xy-plane.

2.5 Nonlinear Scattering Theory

So far, we have considered how material properties ($\chi^{(2)}$), and incident power levels (see Eqs. (2.30) and (2.28)) impact the nonlinear responses. This consideration however lacks in the wave-mixing aspect. To fully consider the interaction between incident and generated fields, we can utilize nonlinear scattering theory (NLST). Instead of an uniform bulk material, NLST considers an optical medium as a collection of point-like scatterers, each located at position $\mathbf{r}$ (see Fig. 2.4).

The starting point of NLST is the calculation of the local electric field $\mathbf{E}_{\mathrm{loc}}(\omega, \mathbf{r})$ induced by an incident electric field $\mathbf{E}_{\mathrm{inc}}(\omega, \mathbf{r})$. These two are connected by the local-field corrections $L(\omega, \mathbf{r})$ [59]:

$$\mathbf{E}_{\mathrm{loc}}(\omega, \mathbf{r}) = L(\omega, \mathbf{r})\mathbf{E}_{\mathrm{inc}}(\omega, \mathbf{r})\,. \tag{2.45}$$

We note that $L(\omega, \mathbf{r})$ is a tensor quantity, and thus, the $\mathbf{E}_{\mathrm{loc}}(\omega, \mathbf{r})$ is not necessarily aligned with $\mathbf{E}_{\mathrm{inc}}(\omega, \mathbf{r})$.

In accordance with the discussion in Section 2.2, $\mathbf{E}_{\mathrm{loc}}(\omega, \mathbf{r})$ induces local material polarization $\mathbf{P}_{\mathrm{loc}}(\omega, \mathbf{r})$, which can act as a source of radiation. To estimate the strength of this emission in the far-field domain, we need to use Lorentz reciprocity. It connects far-field emission $E_{\mathrm{far}}(\omega)$ from a single scatterer

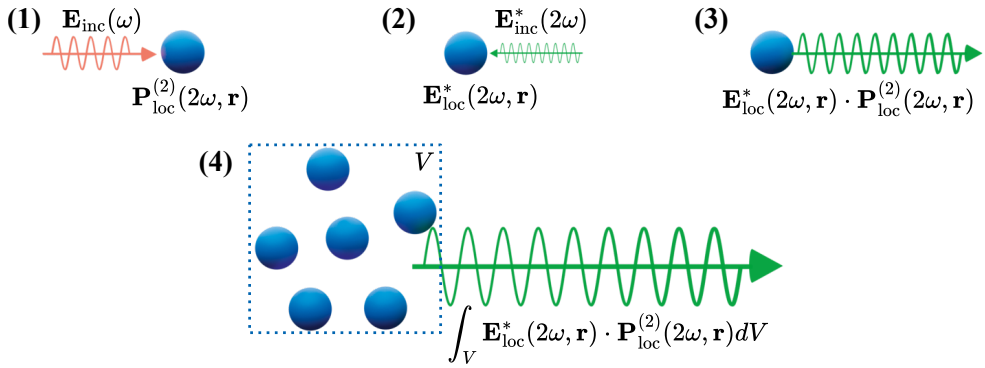

Figure 2.4 The four calculation steps in NLST: **(1)** The calculation of the local nonlinear polarization $\mathbf{P}^{2}_{\mathrm{loc}}(2\omega,\mathbf{r})$ induced by the pump field $\mathbf{E}_{\mathrm{inc}}(\omega)$ on an individual subwavelength scatterer. **(2)** The calculation of the local field at the signal wavelength $\mathbf{E}^{*}_{\mathrm{loc}}(2\omega,\mathbf{r})$ induced by a vacuum field from the detector $\mathbf{E}^{*}_{\mathrm{inc}}(2\omega)$ on the same scatterer. **(3)** The calculation of far-field emission from the scatterer, which is proportional to $\mathbf{E}^{*}_{\mathrm{loc}}(2\omega,\mathbf{r})\cdot\mathbf{P}^{(2)}_{\mathrm{loc}}(2\omega,\mathbf{r})$. **(4)** The calculation of the total response from a larger nonlinear material with the mode-overlap integral $\int_V \mathbf{E}^{*}_{\mathrm{loc}}(2\omega,\mathbf{r})\cdot\mathbf{P}^{(2)}_{\mathrm{loc}}(2\omega,\mathbf{r})dV$.

to the local material polarization as [60]

$$E_{\mathrm{far}}(\omega) \propto \mathbf{E}^{*}_{\mathrm{loc}}(\omega,\mathbf{r})\cdot\mathbf{P}_{\mathrm{loc}}(\omega,\mathbf{r})\,, \tag{2.46}$$

where $\mathbf{E}^{*}_{\mathrm{loc}}(\omega,\mathbf{r})$ corresponds to the local field induced by a vacuum field propagating from the detector $\mathbf{E}^{*}_{\mathrm{inc}}(\omega)$. Furthermore, the calculated $E_{\mathrm{far}}(\omega)$ gives the magnitude for the far-field-domain electric field component that is aligned with $\mathbf{E}^{*}_{\mathrm{inc}}(\omega)$.

The total far-field response of the studied material is then the superposition of all the scattered fields, which can be calculated with the following mode-overlap integral over the total volume V of the optical material:

$$E_{\mathrm{far,tot}}(\omega) \propto \int_V \mathbf{E}^{*}_{\mathrm{loc}}(\omega,\mathbf{r})\cdot\mathbf{P}_{\mathrm{loc}}(\omega,\mathbf{r})\,dV\,. \tag{2.47}$$

For nonlinear processes, Eq. (2.47) becomes an overlap integral between local field profiles at the interacting wavelengths. For SFG, it can be written as

$$E_{\mathrm{far,tot}}(\omega_3) \propto \int_V \mathbf{E}^{*}_{\mathrm{loc}}(\omega_3,\mathbf{r})\cdot\left(\chi^{(2)}(\omega_3;\omega_1,\omega_2):\mathbf{E}_{\mathrm{loc}}(\omega_1,\mathbf{r})\mathbf{E}_{\mathrm{loc}}(\omega_2,\mathbf{r})\right)\,dV\,, \tag{2.48}$$

and for SHG as

$$E_{\mathrm{far,tot}}(2\omega) \propto \int_V \mathbf{E}^*_{\mathrm{loc}}(2\omega, \mathbf{r}) \cdot \left(\chi^{(2)}(2\omega; \omega, \omega) : \mathbf{E}^2_{\mathrm{loc}}(\omega, \mathbf{r}) \right) \, dV \, . \tag{2.49}$$

From the equations above we can draw a few fundamental conclusions. First, they highlight even further that nonlinear processes can be made more efficient by increasing the incident laser powers (step **(1)** in Fig. 2.4). Therefore, many nonlinear technologies rely on ultrashort laser pulses with extreme peak power levels. Second, nonlinear responses are also affected by the properties of the field oscillating at the signal frequency (step **(2)** in Fig. 2.4). Thus, a common enhancement technique is to increase irradiance levels at the interacting wavelengths by coupling pump and signal fields into an optical resonator or other resonant system. Third, Eq. (2.46) indicates that strong nonlinear responses require good alignment between $\mathbf{E}^*_{\mathrm{loc}}(\omega_3, \mathbf{r})$ and $\mathbf{P}^{(2)}_{\mathrm{loc}}(\omega_3, \mathbf{r})$ (step **(3)** in Fig. 2.4). In other words, $\mathbf{E}^*_{\mathrm{inc}}(\omega_3)$ arriving from the detection direction should induce the same dipole moments that $\mathbf{P}^{(2)}_{\mathrm{loc}}(\omega_3, \mathbf{r})$ is associated with. Fourth, the mode-overlap integral in Eqs. (2.48) and (2.49) illustrate the fact that nonlinear processes are highly dependent on the interference between the nonlinear signals generated in the different parts of a nonlinear material (step **(4)** in Fig. 2.4). Constructive interference can result in build-up of the nonlinear response, while destructive inference will shut it down. In conventional nonlinear devices, the constructive interference and signal build-up is ensured with a technique called phase matching, which we describe in more detail next.

2.6 Phase matching

Conventional nonlinear materials are transparent in the VIS and near-infrared (NIR) regions, where the majority of optical processes occur. As Miller's rule illustrates, transparency means also that nonlinear susceptibilities are only of the order of $\sim$1 pm/V. This intrinsic weakness can be overcome with phase-matching techniques that allow the nonlinear signal to build up during propagation in a nonlinear material. Next, we follow the procedure from Boyd's *Nonlinear Optics* [16] to show the basic concepts of phase matching.

2.6.1 Wavevector Mismatch

To start our derivation of phase-matching conditions, we consider three plane waves at two incident frequencies (ω_1 and ω_2) and a summed frequency ($\omega_3 = \omega_1 + \omega_2$) that propagate along the z-axis. Their electric field amplitudes can be written in the form of

$$E(\omega_j, z) = A_j(z)\mathrm{e}^{\mathrm{i}k_j z}, \tag{2.50}$$

where $A_j(z)$ is the spatial amplitude term associated with frequency ω_j, and $k_j = n_j \frac{2\pi}{\lambda_j}$.

The evolution of $A_j(z)$ while propagating through the nonlinear optical material can be described as:

$$\frac{\mathrm{d}A_j(z)}{\mathrm{d}z} = \mathrm{i}\frac{k_j}{2n_j^2\epsilon_0}P^{NL}(\omega_j, z)\mathrm{e}^{-\mathrm{i}k_j z}\,. \tag{2.51}$$

For SFG, the electric field components are $E(\omega_1, z) = A_1(z)\mathrm{e}^{\mathrm{i}k_1 z}$, $E(\omega_2, z) = A_2(z)\mathrm{e}^{\mathrm{i}k_2 z}$, and $E(\omega_3, z) = A_3(z)\mathrm{e}^{\mathrm{i}k_3 z}$. The corresponding nonlinear polarization at the signal frequency is $P^{NL}(\omega_3) = \epsilon_0\chi^{(2)}A_1(z)A_2(z)\mathrm{e}^{\mathrm{i}(k_1+k_2)z}$. To consider the growth of $A_3(z)$, we put these terms into Eq. (2.51) and get that

$$\frac{\mathrm{d}A_3(z)}{\mathrm{d}z} = \mathrm{i}\frac{k_3\chi^{(2)}}{n_3^2}A_1(z)A_2(z)\mathrm{e}^{\mathrm{i}\Delta k z}\,. \tag{2.52}$$

Here, we have defined *wavevector mismatch* $\Delta k = k_1 + k_2 - k_3$.

Next, we consider the evolution of the SFG field after propagating through a second-order nonlinear crystal of length L_c. We assume also that the pump amplitudes remain constant, i.e., $A_1(z) = A_1$ and $A_2(z) = A_2$. We start by integrating Eq. (2.52) from $z = 0$ to $z = L_c$, which yields

$$A_3(L_c) = \mathrm{i}\frac{k_3\chi^{(2)}A_1A_2}{n_3^2}\left(\frac{\mathrm{e}^{\mathrm{i}\Delta k L_c} - 1}{\mathrm{i}\Delta k}\right)\,. \tag{2.53}$$

By inserting $A_3(L_c)$ into Eq. (2.9), we get the SFG irradiance $I_3(L_c)$ in terms of pump irradiances I_1 and I_2, crystal length L_c, and the wavevector mismatch

Δk:

$$I_3(L_c) = \frac{2k_3^2\left|\chi^{(2)}\right|^2 I_1 I_2}{\epsilon_0 c_0 n_1 n_2 n_3^2} L_c^2 \mathrm{sinc}^2(\Delta k L_c/2)\,. \tag{2.54}$$

From Eq. (2.54) we can draw the following conclusions. First, the SF intensity scales linearly with the pump irradiances, emphasizing the importance of high-intensity pump lasers for nonlinear optics. Second, in perfect phase-matching conditions, i.e., $\Delta k = 0$, I_3 scales quadratically with the propagation distance (see Fig. 2.5). This is due to the fact that the sinc-term has its maximum value at zero. If $\Delta k \neq 0$, the generated signal does not build up during propagation, but rather oscillates periodically between a low value and zero (see Fig. 2.5) [61]. This oscillation occurs in periods of *coherence length* given by $L_{\mathrm{coh}} = 2/\Delta k$.

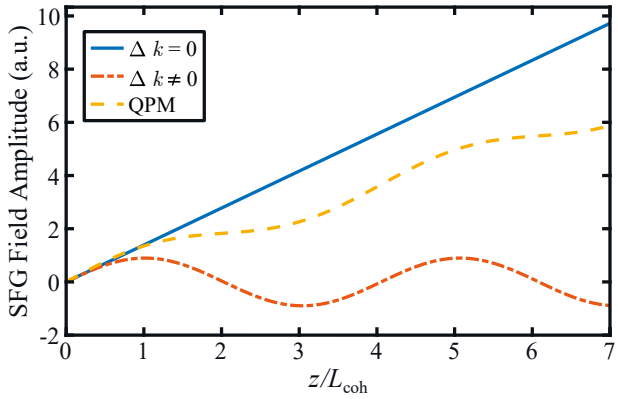

Figure 2.5 Evolution of SFG field amplitude over propagation distance in a nonlinear material. If the process is perfectly phase matched (blue line), i.e., $\Delta k = 0$, the field amplitude scales linearly with the propagation length. If $\Delta k \neq 0$ (red line), the signal does not build up, but rather keeps oscillating between two relatively small values. If $\Delta k = 0$ cannot be achieved, it can be circumvented by using quasi-phase-matching (QPM). With QPM (yellow line), the field amplitude increases quasi-linearly with the propagation.

2.6.2 Perfect Phase-matching Conditions

Unfortunately, perfect phase-matching conditions are hard to achieve in natural materials. This effect can be easily shown by looking more into Δk in terms of

interacting wavelengths and refractive indices. For SFG,

$$\Delta k_{SFG} = k_1 + k_2 - k_3 = \frac{2\pi n_1}{\lambda_1} + \frac{2\pi n_2}{\lambda_2} - \frac{2\pi n_3}{\lambda_3}\,. \tag{2.55}$$

and for SHG,

$$\Delta k_{SHG} = 2k_1 - k_3 = 2\frac{2\pi n_1}{\lambda_1} - \frac{2\pi n_3}{\lambda_1/2} = \frac{4\pi}{\lambda_1}\left(n_1 - n_3\right). \tag{2.56}$$

As we mentioned above, perfect phase matching requires that $\Delta k = 0$. For forward SHG, this would mean that $n_1 = n_3$, which is hard to fulfill in dispersive materials where refractive indices change with frequencies. The same can be concluded for SFG, for which the phase-matching condition turns out to be

$$n_3 - n_2 = (n_1 - n_2)\frac{\lambda_3}{\lambda_1}\,. \tag{2.57}$$

Yet again, dispersion raises problems, as $n_3 > n_2 > n_1$ for typical optical materials. Consequently, the two sides of Eq. (2.57) have opposite signs.

Perhaps the most common way to achieve perfect phase matching is to use type I or type II processes and utilize birefringence of nonlinear materials [26, 62]. When the interacting fields have different polarizations, they can experience refractive indices for which phase-matching conditions are fulfilled, overcoming the dispersion-caused problems. Since birefringence is highly dependent on the crystal orientation and temperature, both tilt and temperature of the nonlinear material are often used to tune, control, and stabilize phase-matching conditions [46, 63]

2.6.3 Quasi-phase-matching

Another common method to overcome nonzero Δk is known as quasi-phase-matching (QPM) [27, 64–66]. In QPM materials, the nonlinear crystal is periodically poled, i.e., one of the crystal axes is periodically inverted. Consequently, the sign of the relevant $\chi^{(2)}$ tensor is periodically changed along the propagation direction. This periodic inversion of the $\chi^{(2)}$ sign can be used to compensate the nonzero Δk. With fulfilled QPM, the signal amplitude will build up quasi-linearly during propagation, with some oscillatory features (see

Fig. 2.5). Next, we will explain the QPM mechanism in more detail.

As a simple example, we consider the situation where the sign of $\chi^{(2)}$ is changed twice within a poling period Λ. Then, $\chi^{(2)}(z)$ can be expressed as[16]

$$\chi^{(2)}(z) = \chi^{(2)} G_m \mathrm{e}^{\mathrm{i}k_m z}\,, \tag{2.58}$$

where $k_m = 2\pi m/\Lambda$ and $G_m = (2/m\pi)\sin(m\pi/2)$.

By substituting $\chi^{(2)}(z)$ into Eq. (2.53), we see that the wavevector mismatch now becomes

$$\Delta k_Q = k_1 + k_2 - k_3 + k_m\,. \tag{2.59}$$

As G_m, and consequently $\chi^{(2)}(z)$, decrease with increasing m, it is wise to achieve QPM for the first-order interaction with $m = -1$. The wavevector mismatch then becomes

$$\Delta k_Q = k_1 + k_2 - k_3 - 2\pi/\Lambda\,, \tag{2.60}$$

which becomes zero, i.e., QPM is achieved when

$$\Lambda = 2\pi/(k_1 + k_2 - k_3) = 2L_{\mathrm{coh}}\,. \tag{2.61}$$

Similar to birefringent phase mathching, QPM can be modified by, e.g., tilting the nonlinear crystal, which changes Λ. Unlike birefringent phase matching, however, QPM can be used also for type 0 processes, allowing efficient use of materials, such as lithium niobate, for which a $\chi^{(2)}_{iii}$ tensor component is the largest one. QPM also allows phase matching more sophisticated processes, such as broadband and adiabatic frequency conversion [67, 68], and backward nonlinear processes [69–72], which we discuss next.

2.6.4 Backward Second-order Processes

So far, we have discussed forward nonlinear processes, where all interacting beams propagate along the same direction. Sometimes however, it is more beneficial to use so called backward processes, where the signal beam propagates to opposite to the direction of the pump beams. Such processes can be used, e.g., for cascaded third-order processes [73]. Cascaded THG, e.g., results from SFG

between pump and SH signal beams. Interestingly, cascaded THG becomes more efficient with backward SHG, as then both the pump and SH fields have their maximum amplitude at the input interface of the nonlinear crystal.

In backward processes, the sign of the signal wavenumbers changes, and the wavevector mismatch for backward SHG becomes

$$\Delta k_{\mathrm{SHG,bw}} = 2k_1 + k_2 \,, \tag{2.62}$$

and for backward SFG

$$\Delta k_{\mathrm{SFG,bw}} = k_1 + k_2 + k_3 \,. \tag{2.63}$$

From Eqs. (2.62) and (2.63), we can again derive the phase-matching conditions. For backward SHG, the condition becomes $n_1 = -n_3$, and $\frac{1}{\lambda_1}(n_2 - n_1) = \frac{1}{\lambda_3}(n_3 + n_2)$ for backward SFG. Both conditions are practically impossible to fulfill in transparent materials were refractive indices are all positive and relatively close to each other. Therefore, traditional nonlinear materials must rely on QPM for achieving efficient backward processes, through the additional momentum term k_m.

3 METAMATERIALS AND NONLINEAR OPTICS

Metamaterials are artificial structures consisting of subwavelength building blocks, typically metal or dielectric NPs, on a glass substrate [74]. With intelligent selection of the building block properties, such as their size, shape, and mutual orientation, the bulk metamaterial can be set to exhibit optical properties not often found in nature. For example, negative refractive index, subwavelength field-confinement, and nanoscale phase control of optical fields have been demostrated in metamaterials [75–80]. These unique properties enable a plethora of novel flat free-space components, such as metasurface lenses, polarizers, antireflectors, and holograms [81–88].

In this Chapter, we discuss the physical phenomena relevant for our research on metasurfaces. We start with the description of the individual NP responses, namely LSPRs. Then, we introduce the theory behind SLRs, which arise from interparticle coupling in periodic NP arrays. We finish the theoretical discussion of this Thesis with the description of nonlinear properties of plasmonic metasurfaces using the NLST.

3.1 Localized Surface Plasmon Resonances

The electromagnetic properties of metals are governed by the collective oscillations of their conduction electrons, also known as plasmons [89]. In the case of metallic NPs, plasmons are confined to the vicinity of the interfaces between the metal structure and the surrounding dielectric material, and are thus usually referred to as localized surface plasmons (LSPs) [90] (see Fig. 3.1 a). Under resonant conditions, incident light will be coupled to the LSP modes of the NPs. As a result, electric dipoles are formed, giving rise to strong electric fields at vicinity of the NP (see Fig. 3.1 b). This resonant behavior is known as localized surface plasmon resonance (LSPR), which can be seen as relatively broad

spectral features near the resonance wavelength λ_0 in, e.g., the transmission spectrum of a plasmonic structure (see Fig. 3.1 c).

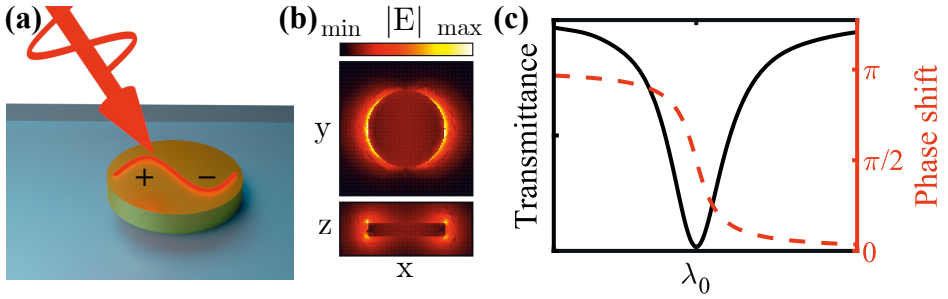

Figure 3.1 Schematic illustration of localized surface plasmon resonance (LSPR). (a) When light interacts with a metallic NPs, it induces plasmons on the NP surfaces. (b) LSPR occurs, when incident light is in resonance with the surface plasmons and is confined onto the NP surface. As a result, the electric field near the NP is increased dramatically. (c) LSPRs are visible in transmission spectra (black) as resonance dips at the resonant wavelength λ_0. NPs also induce a phase shift (red) to the light field interacting with the NPs. Near λ_0, the phase shift becomes very wavelength-dependent.

The spectral location of LSPR is tightly connected to the dimension along which plasmon oscillations occur, also known as the plasmon length [91]. It depends on mumerous factors, including refractive index of the material surrounding the NPs, and the material choice of the NPs themselves. Most importantly, the plasmon length is related to the NP shape and size. The most obvious conclusion from this is that larger NPs have longer resonance wavelengths. The plasmon length can also vary along different directions of the NP shape in, e.g., triangular, rectangular, or ellipsoidal NPs. In other words, this happens with anisotropic NP shapes. As plasmon oscillations follow the polarization of the incident light, the plasmon length and λ_0 become polarization dependent.

One example of aninsotropic NP shapes is the V-shape (see Fig. 3.2), where two NP arms are opened symmetrically with respect to the NP symmetry axis (y-axis). When incident light is y-polarized, the plasmon oscillations occur symmetrically with respect to y-axis and along the two NP arms. For x-polarized light, plasmon oscillations occur along the whole length of the combined two arms. Consequently, the LSPR for x-polarized light occurs at significantly longer wavelength than the LSPR for y-polarized light. This polarization-dependence is also highly tunable through, e.g., modifying the angle between the two NP arms.

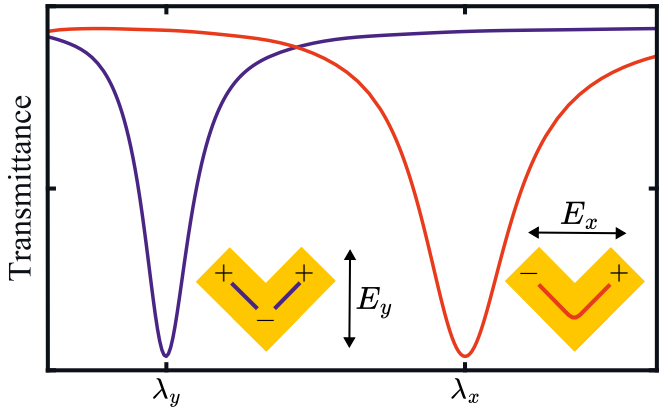

Figure 3.2 In V-shaped NPs, plasmon oscillation directions associated with x- and y-polarized light differ considerably. Consequently, LSPRs in such NPs are polarization dependent, with different resonance wavelengths λ_x and λ_y, for x- and y-polarized light, respectively.

In addition to resonant coupling and local field enhancements, plasmonic NPs also scatter incident light, which induces phase shifts δ into the interacting light field. The magnitude of δ is highly wavelength-dependent, especially near λ_0 (see Fig. 3.1 c). In a simplified singly-resonant system, $\delta = \pi$ if $\lambda \ll \lambda_0$, $\delta = \pi/2$ if $\lambda = \lambda_0$, and $\delta = 0$ if $\lambda \gg \lambda_0$. As λ_0 is highly dependent on the NP shape and size, the NP geometry provides a flexible method for varying δ. This enables nanoscale phase-control, which has been used in, e.g., holography and beam steering [92–94]. In this Thesis, we utilized the wavelength-dependence of δ to achieve phase matching for SHG from stacked metasurfces in **Publication I**.

3.2 Surface Lattice Resonances

The most typical type of plasmonic metasurface is a NP grating, where the NPs are arranged in a periodic lattice, such as square, rectangular, or honeycomb lattice [95]. In such cases, the NP array also acts as a diffraction grating, and light scattered by the NPs can be coupled to the diffraction modes of the grating. When the coupling happens along the metasurface plane, the NPs induce propagating surface waves that intensify local-field hotspots on the NP surfaces (see Fig. 3.3 a). This phenomenon is known as SLR, which occurs near the Rayleigh anomaly (RA) wavelength of the lattice, at which the diffracted

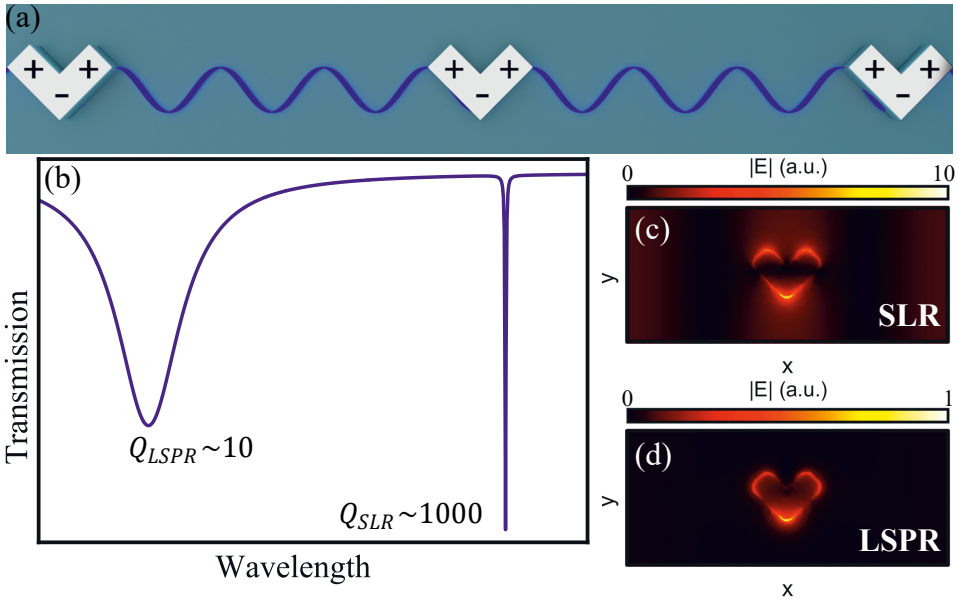

Figure 3.3 (a) When plasmonic NPs are arranged in a periodic array, their light-induced dipoles can couple constructively, resulting in a propagating surface wave. Incident light can couple into these surface modes, giving rise to a collective response known as surface lattice resonance (SLR). (b) SLRs have much higher quality factors (Q-factors) than the individual nanoparticle responses, such as localized surface plasmon resonances (LSPRs), have. (c)-(d) High-Q SLRs result in much stronger local-field enhancements than low-Q LSPRs.

wave propagates along the diffraction grating [96]. For one dimensional grating and normally incident illumination, the RA wavelength is given as

$$\lambda_{RA} = np, \tag{3.1}$$

where p is the grating periodicity.

Similar to other collective responses, such as guided mode resonances and bound states in the continuum [38, 97], SLRs are very selective in terms of incident polarization states, incidence angle, lattice periodicity, and the surrounding refractive index profile [98–104]. Therefore, SLRs show high potential for, e.g., sensing and lensing [105–107]. This sensitivity of SLRs can be seen as spectral features that are much narrower than the ones associated with LSPRs (see Fig. 3.3 b). Such differences are often expressed in terms of quality factors (Q-factors), calculated by

$$Q = \frac{\lambda_0}{\Delta\lambda}, \tag{3.2}$$

where $\Delta\lambda$ is the full-width of half-maximum (FWHM) of a spectral resonance feature. Typical LSPRs have $Q \leq 10$ while SLRs often have Q of several hundreds [108], with the plasmonic SLR world record being $Q \approx 2400$ [109].

High Q-factors and narrow linewidths indicate long lifetimes for SLR states. Consequently, field amplitudes at the local-field hotspots near the NP interfaces build up stronger than in the case of LSPRs. Due to this strong local-field enhancement, SLRs have been utilized for example in photovoltaics and lasing [110, 111].

3.3 Polarization Dependence and Spatial Dispersion of Surface Lattice Resonances

The RA wavelengths in plasmonic metasurfaces can be estimated with the so called empty-lattice approximation (ELA), which simply considers the lattice geometry and wave vectors of incident and diffracted waves. It does not consider individual NP properties, which can shift, broaden, and weaken the occurring SLRs. To consider and optimize individual NP properties for the occurring SLRs, computational models such as discrete-dipole approximation or lattice-sum approach could be used [112–114]. However, the more rigorous and sophisticated tools need a lattice configuration as a starting point. For this purpose, ELA is a powerful and fast tool. Here, we utilize ELA to calculate RA wavelengths in rectangular NP lattices, which we used in **Publications II** and **III**.

Let us consider a rectangular NP array with periodicities p_x and p_y along the metasurface x- and y-coordinates, respectively (see Fig. 3.4 a). For such an array, the RA wavelengths are given by [115]

$$\lambda_{i,j} = -A + \sqrt{A^2 - B}, \tag{3.3}$$

where i and j are diffraction orders along x- and y- coordinates, respectively. The terms A and B are given by

$$A = \frac{\sin\theta}{(i/p_x)^2 + (j/p_y)^2}\left(\frac{i\sin\phi}{p_x} + \frac{j\cos\phi}{p_y}\right) \tag{3.4}$$

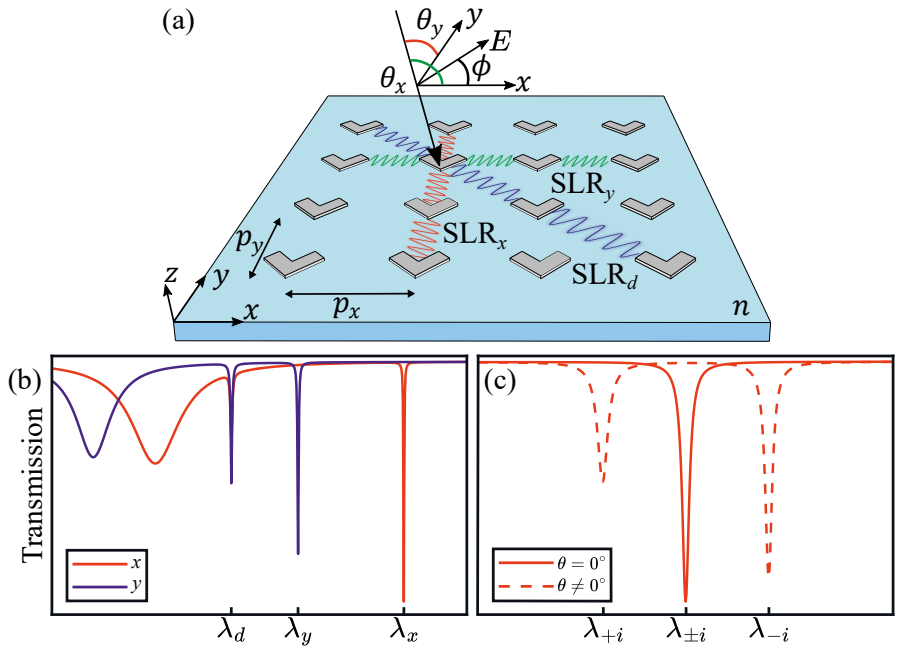

Figure 3.4 (a) Formation of surface lattice resonances on a rectangular array depends on numerous factors: incident angle θ, azimuthal angle ϕ, refractive index n, and lattice constants p_x and p_y. In-plane parallel SLRs form along the axis which is orthogonal to polarization of incident light. For x-polarized light (red waves), SLR wavelength λ_x depends on θ_y and p_y, and for y-polarized light, it depends on θ_x and p_x. Diagonal SLRs (blue waves) occur for both polarizations at the same wavelength λ_d. (b) With $p_x \neq p_y$, the formation of parallel SLRs becomes polarization-dependent as $\lambda_x \neq \lambda_y$. (c) SLR are also spatially dispersive, i.e., angle-dependent. With $\theta = 0°$ (solid line), SLRs corresponding to positive $(+i)$ and negative $(-i)$ diffraction orders occur at the same wavelength $\lambda_{\pm i}$. With $\theta \neq 0°$ (dashed line), λ_{+i} and λ_{-i} shift to opposite directions from $\lambda_{\pm i}$.

and

$$B = \frac{\sin^2\theta - n^2}{(i/p_x)^2 + (j/p_y)^2}\,. \tag{3.5}$$

In the equations above, n is the refractive index of the surrounding material, θ is the incident angle, and ϕ is the azimuthal angle, which in our consideration is the angle between the E-field of the incident light and the x-axis.

In this Thesis, we only consider in-plane SLRs that occur when the polarization of the incident light and the induced dipoles in the nanoparticles are parallel to the metasurface. This occurs for transverse electric light, i.e., for light whose polarization is orthogonal to the incident plane. Such SLRs can form only in directions that are not parallel to the incident polarization. The

most obvious direction is perpendicular to the polarization, i.e., along the incident plane. We name them parallel SLRs, referring to the fact that SLR waves form along the incident plane.

Here, our main focus is on the first-order SLRs for either x- or y-polarized light. Especially, we utilize SLRs corresponding to diffraction orders $(\pm 1, 0)$, $(0, \pm 1)$, and $(\pm 1, \pm 1)$. The diffraction order $(0, \pm 1)$ corresponds to x-polarized parallel SLR, for which $\phi = 0°$, and the incident plane is along the y-axis. Consequently, the parallel SLR for x-polarized light occurs near the corresponding RA wavelength

$$\lambda_x = \lambda_{0,\pm 1} = p_y(n \mp \sin\theta_y)\,, \tag{3.6}$$

where θ_y is the incident angle along the yz-plane.

Similar logic can be applied for y-polarized parallel SLR, which corresponds to $(0, \pm 1)$. Now, $\phi = 90°$, and the RA wavelength associated with y-polarized SLR becomes dependent on θ_x along the xz-plane:

$$\lambda_y = \lambda_{\pm 1,0} = p_x(n \mp \sin\theta_x)\,. \tag{3.7}$$

SLRs can form also along the diagonal of the metasurface, corresponding to the diffraction order $(\pm 1, \pm 1)$. We name them as diagonal SLRs, which occur similarly for both x- and y-polarized light. At normal incidence, the resonance wavelength for diagonal SLRs is given by

$$\lambda_d = \lambda_{\pm 1,\pm 1} = n\frac{p_x p_y}{p_d}, \tag{3.8}$$

where $p_d = \sqrt{p_x^2 + p_y^2}$ is the periodicity along the metasurface diagonal. We note that λ_d is dependent on both θ_x and θ_y.

Equations (3.6) and (3.7) illustrate how by changing p_x and p_y, the SLRs in simple rectangular lattices can be made polarization dependent (see Fig. 3.4 b). Equations (3.6) and (3.7) also indicate how SLRs are angle-dependent, i.e., spatially dispersive (see Fig. 3.4 c). At normal incidence, the parallel SLRs corresponding to positive and negative diffraction orders occur at the same wavelength. When the incidence angle is changed, these two diffraction orders shift to opposite directions, and the resonance peak splits into two peaks. It is also notable that orthogonal SLRs can be tuned independently from each other:

the x-polarized SLR depends only on θ_y and p_y, while y-polarized SLR depends only on θ_x and p_x. Overall, the polarization-dependence and dispersion of SLRs enable post-fabrication tunability that is not available with non-dispersive resonances, such as LSPRs. This tunability can be used in realizing [116] and modifying multiply-resonant metasurfaces, as we did in **Publication II**.

3.4 Nonlinear Responses of Plasmonic Metamaterials

The NLST introduced in Section 2.5 can be also used to estimate nonlinear responses of metasurfaces [117]. This is commonly done in three steps (see Fig. 3.5). First, the nonlinear polarization is estimated inside the metamaterial building block. Then, local-field profiles at the signal wavelength are evaluated. And finally, the mode overlap between the two is calculated. With metamaterials, the resonance enhancements for the local-field profiles are at the main focus, rather than pump power levels and phase-matching considerations.

In plasmonic metamaterials, hardly any EM field is inside the NPs and the nonlinear response arises largely from the fields near the metal–dielectric interfaces. Therefore, we do not use volume susceptibilities but rather surface susceptibilities $\chi^{(2)}_{\mathrm{surf}}$ to calculate nonlinear responses. Using $\chi^{(2)}_{\mathrm{surf}}$, we can rewrite NLST Eqs. (2.48) and (2.49) for plasmonic nanoparticles. For SFG, the far-field emission is calculated as

$$E_{\mathrm{far,tot}}(\mathbf{k}_3,\omega_3) \propto \int_S \mathbf{E}^*_{\mathrm{loc}}(\mathbf{k}_3,\omega_3,\mathbf{r})\cdot\Big(\chi^{(2)}_{\mathrm{surf}}(\mathbf{r}) : \mathbf{E}_{\mathrm{loc}}(\mathbf{k}_1,\omega_1,\mathbf{r})\mathbf{E}_{\mathrm{loc}}(\mathbf{k}_2,\omega_2,\mathbf{r})\Big)\, dS\,, \tag{3.9}$$

and for SHG as

$$E_{\mathrm{far,tot}}(\mathbf{k}_2,2\omega) \propto \int_S \mathbf{E}^*_{\mathrm{loc}}(\mathbf{k}_2,2\omega,\mathbf{r})\cdot\Big(\chi^{(2)}_{\mathrm{surf}}(\mathbf{r}) : \mathbf{E}^2_{\mathrm{loc}}(\mathbf{k}_1,\omega,\mathbf{r})\Big)\, dS\,. \tag{3.10}$$

Here, we calculate the mode-overlap integral only over the NP interface and not the entire volume, indicated with S. In the $\mathbf{E}_{\mathrm{loc}}(\mathbf{k},\omega,\mathbf{r})$ terms, $\mathbf{k}$ and ω are the wave vector and angular frequency of the incident light field, and $\mathbf{r}$ is the position vector on the NP interface.

The equations above also indicate that the SFG and SHG responses can be dramatically boosted with local-field-enhancing resonances, such as LSPRs. Especially, they highlight the potential of collective high-Q resonances, such as

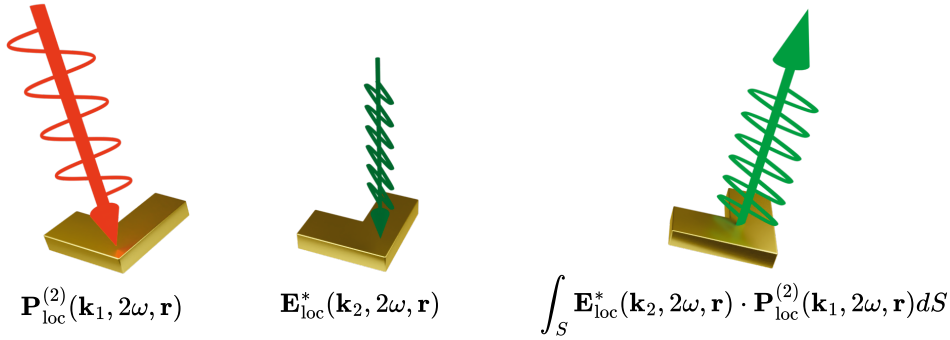

Figure 3.5 In the case of plasmonic NPs, the nonlinear responses arise mostly from the NP surface. Therefore, the calculation steps in NSLT, i.e., the calculation of local nonlinear polarization (left), local fields at the signal wavelength (middle), and the mode-overlap between the two (right) are performed over the NP surface S.

SLRs and guided mode resonances [118, 119]. Furthermore, they indicate also the usefulness of multiply-resonant structures that exhibit resonances at each of the interacting wavelengths [120–122].

3.5 Symmetry Considerations with Nonlinear Nanoparticles

The $\chi^{(2)}_{\mathrm{surf}}(\mathbf{r})$ in Eqs. (3.9) and (3.10) can be formed by modifying the surface susceptibility for an isotropic interface introduced in Section 2.4.4. Here, it is convenient to define the local tensor components in terms of the NP surface normal $\hat{\mathbf{n}}$ and tangent $\hat{\mathbf{t}}$. With this approach, the nonzero tensor components are $\chi^{(2)}_{nnn}$, $\chi^{(2)}_{ntt}$, and $\chi^{(2)}_{tnt} = \chi^{(2)}_{ttn}$ [123]. Since $\hat{\mathbf{n}}$ and $\hat{\mathbf{t}}$ differ for the different sides and edges of the investigated NP, it is important to define them accurately at each position $\mathbf{r}$, to get the correct $\chi^{(2)}_{\mathrm{surf}}(\mathbf{r})$.

After properly defining $\chi^{(2)}_{\mathrm{surf}}(\mathbf{r})$, we can calculate the nonlinear response for a situation, where the generated signal and incident pump fields are associated with polarization states i, j, and k, respectively. After performing the calculation for all possible permutations of field polarization states, we can define the effective, or in other words macroscopic, susceptibility $\chi^{(2)}_{\mathrm{eff}}$ for the investigated metasurface. More precisely, we can define which of the $\chi^{(2)}_{\mathrm{eff}}$ tensor components are vanishing and which become dominant.

As expected, NLST calculations indicate that a metasurface resembling a specific symmetry group has the same nonzero $\chi^{(2)}_{eff}$ tensor components as a

macroscopic interface belonging to the same symmetry group [124]. For example, an array of nanodisks does not have second-order responses at normal incidence (see Fig. 3.6), although there is a nonzero local nonlinear response at local-field hotspots near the nanodisk edges (see Fig. 3.1 b). The local responses at the opposite sides of the nanodisks have opposite signs, and thus, they cancel each other out for the total far-field response [123]. This cancellation can be avoided by breaking the normal-incidence conditions for either pump or signal fields. Overall, this means that an array of nanodisks have the same nonzero $\chi^{(2)}_{eff}$ tensor components as the macroscopic and isotropic interface ($C_{\infty v}$ class), which such an array geometrically resembles.

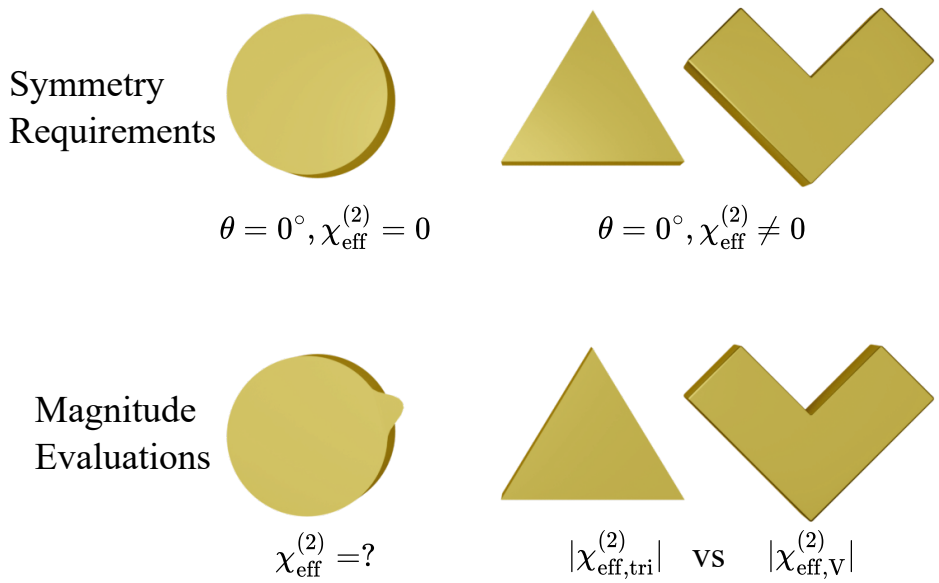

Figure 3.6 (Top row) Calculations based on NLST for plasmonic NPs result in the same symmetry requirements for second-order nonlinear responses as the macroscopic interfaces. For example, nanodisks resemble an isotropic interface and do not have a second-order response at normal incidence, while triangular and V-shaped NPs resembling C_{1v} symmetry do. (Bottom left) NLST can be also used to estimate the nonlinear responses arising from, e.g., structural deformations. (Bottom right) NLST can be also used to optimize the NP shape for the desired nonlinear process.

The same logic applies to anisotropic NPs, such as V-shaped NPs, triangular NPs, and split-ring resonators [125–127]. In this Thesis, we especially used V-shaped NPs arranged in periodic arrays and oriented similarly (see Figs. 3.3 and 3.4). With the NP symmetry axis set along the metasurface y-axis, such

metasurface resembles a macroscopic interface of the symmetry group C_{1v}, and therefore, has the same nonzero $\chi^{(2)}_{\text{eff}}$ components. Furthermore, both x- and y-polarized light induce local-field hotspots at the ends of the NP arms [79]. From the mode overlap point-of-view, the V-shape is therefore a good choice for the second-order processes with normally incident light, i.e., the processes associated with the effective susceptibility components $\chi^{(2)}_{yyy}$, $\chi^{(2)}_{yxx}$, and $\chi^{(2)}_{xxy} = \chi^{(2)}_{xyx}$.

As the discussion above indicates, the nonzero $\chi^{(2)}_{\text{eff}}$ components can be deduced from the geometry of the NPs and their organization into lattices [128]. However, the magnitude of the said tensor components cannot be estimated from the metasurface geometry alone, and NLST calculations become necessary. Furthermore, $\chi^{(2)}_{\text{eff}}$ can be evaluated with NLST not only for NPs with regular shapes but also for shapes with small fabrication defects and even for arbitrary shapes [129–131]. Therefore, NLST is a powerful tool for identifying sources of nonlinear response and ultimately optimizing the metasurface configuration for the desired nonlinear process.

4 DESIGN AND CHARACTERIZATION OF NONLINEAR METAMATERIALS

Studying metamaterials, or any other novel optical materials, consist of three main parts: design, fabrication, and characterization, preferably in this order. In this chapter, we give general descriptions of the computational and characterization methods used in the publications for this Thesis. Since the author did not perform any fabrication during the thesis project, we do not discuss fabrication methods here. Instead, we encourage the reader to see **Publications I** and **II** for the fabrication details.

4.1 Numerical Simulations for Nonlinear Metamaterials

Most of the optical properties of metasurfaces can be evaluated through numerical methods such as finite-difference time-domain (FDTD) method and finite element method (FEM) [132–135]. For the simulations of this Thesis, we used commercial simulation softwares Ansys FDTD Solutions and COMSOL Multiphysics, which utilize FDTD and FEM, respectively. Both softwares are similarly straightforward to use for simple simulations, but for more specific simulations, one software is more suitable than the other. For example, the scripting option in Ansys makes large parameter sweeps considerably easier to perform and analyze, when compared against performing them using COMSOL. On the other hand, FDTD simulations become very slow with non-zero incidence angles, while COMSOL handles such simulations in a much faster manner.

The typical simulation using either of the softwares starts with the building of the unit cell of the investigated metasurface. The unit cell consist of five parts (see Fig. 4.1): metamaterial building block (typically a nanoparticle), substrate and superstrate materials (typically glass and/or air), simulation

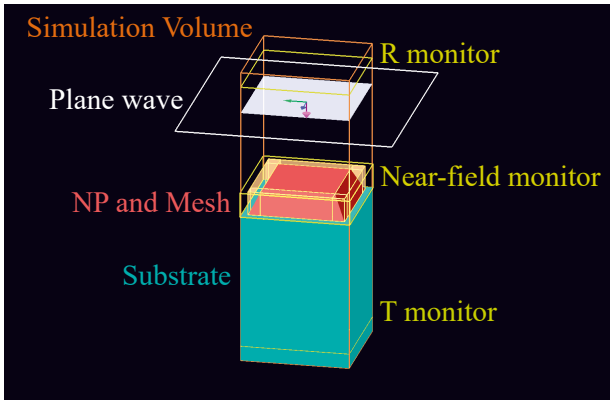

Figure 4.1 Typical simulation layout in the Ansys FDTD Solutions software for evaluating optical properties of a metasurface. The orange outlines show the simulation volume, for which, correct boundary conditions should be assigned, such as periodic boundary conditions for periodic metasurfaces. Inside the simulation volume, there is the simulated nanoparticle (NP) with proper meshing around it, a glass substrate, and an air superstrate. The simulation is performed for plane wave illumination (white). The results are stored in transmission (T), reflection (R), and near-field monitors.

boundaries with their specific boundary conditions (BCs), a plane-wave source, and monitors to evaulate metasurface's transmission, reflection, and local-field profiles. In COMSOL, the evaluation of local-field profiles does not require additional monitors, as the fields are evaluated and stored automatically for the entire simulation volume.

To run successful and optimal simulations, in terms of simulation time, file size, and accuracy, it is necessary to optimize the spectral resolution of the simulation and the meshing of the simulation volume, and also to select BCs correctly. To reach high enough spectral resolution, for example to accurately investigate high-Q resonances, the user of COMSOL needs to increase the number of evaluated frequency points, while the Ansys user should increase the used simulation time in the simulation settings. During the use of either of the softwares, an increase of the spectral resolution results in increased simulation time and file size. It is also important to properly mesh the simulation volume for properly balanced simulation time and accuracy of results. As a rule of thumb, the meshing should be just fine enough at interfaces and in the nanostructures, while keeping it as coarse as possible everywhere else. Finally, the correct selection of BCs is paramount. For periodic metasurfaces in the xy-plane, periodic

BCs should be used along the x- and y-directions. Using periodic BCs, the calculations make the assumption of infinite copies of metasurface unit cells along the periodic directions, which is an adequate approximation for large-enough metasurfaces. In the z-direction, which is typically the injection axis of the incident plane wave, perfectly matched layer (PML) BCs should be used. PMLs make sure that no unphysical back-reflections of simulated fields take place at the boundaries of the simulation volume, which could lead to unrealistic results.

After the proper build-up of the simulation design and successfully running the simulation, the simulated data can be extracted for further analysis in, e.g., Matlab. In this Thesis, this data consists of transmission and reflection spectra, resonance-induced phase shifts, and electric field vectors near the nanostructures. Next, we describe the analysis of this data in more detail and show how it can be used to evaluate the nonlinear responses of resonant metamaterials.

4.1.1 Computation of Nonlinear Responses

For **Publication III**, we estimated the nonlinear responses of the investigated metasurface using NLST. This requires simulation of the linear near-field responses at the interacting wavelengths and using them as input for the mode-overlap calculations. Here, we describe how Ansys FDTD Solutions (or COMSOL) and Matlab can be used to complete this task.

As said, the first step of our method is to simulate the linear local-field responses of the investigated metasurface. For this, the simulation unit cell should be constructed correctly following the guidelines of the previous Section. After completing the simulation, we need to export the needed results from the simulation software: transmission data, local electric field distributions near the investigated NPs, and data connecting the spatial coordinates to the NPs. When simulating with Ansys FDTD Solutions, the connectivity data set can be selected as the refractive index distribution near the NP. From this data set, the coordinates of the plasmonic NP can be identified, since the imaginary component of refractive index is much larger for metals than for dielectrics that we use as substrate materials. With COMSOL, it is convenient to export domain indices that directly indicate which coordinates correspond to the investigated NP.

Next, the exported simulation data is imported to Matlab for the NLST

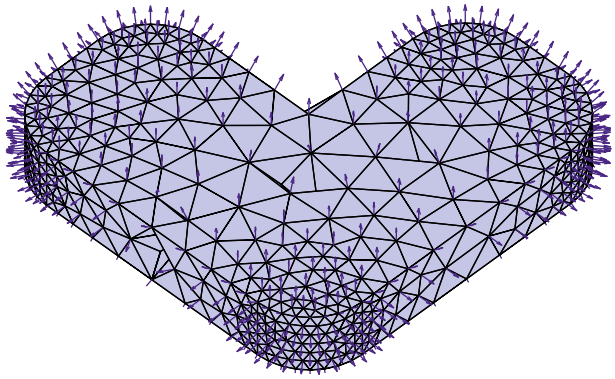

Figure 4.2 Illustration of a triangulated surface of a simulated nanoparticle. At each triangulation point, we can define surface normals (blue arrows) that can be used to form local second-order susceptibilities.

calculations. The first step is to identify to the NP surface coordinates, either from the refractive index or domain index data. Then, we triangulate the NP surface (using, e.g., Delaunay triangulation [136]) and form surface normal vectors $\hat{\mathbf{n}}$ at each triangulation point (see Fig. 4.2). Then, we use the simulated electric fields to estimate $\mathbf{E}_{\mathrm{loc}}(\omega, \mathbf{k}, \mathbf{r})$ at the triangulation points. As the last step before mode-overlap calculations, we use $\mathbf{n}_s$ to form the local susceptibility $\chi^{(2)}_{\mathrm{loc}}(\mathbf{r})$ tensors at each triangulation point using coordination transformations on known metal-dielectric interface susceptibilities $\chi^{(2)}_{\mathrm{surf}}$ (see Section 3.4).

After getting $\chi^{(2)}_{\mathrm{loc}}(\mathbf{r})$ and $\mathbf{E}_{\mathrm{loc}}(\omega, \mathbf{k}, \mathbf{r})$, we can input them into the mode overlap integral, which we have modified into a Riemann sum. For SHG, the far-field emission at the SH frequency is calculated as

$$E_{\mathrm{far,tot}}(2\omega, \mathbf{k}_2) \propto \sum_i \mathbf{E}^*_{\mathrm{loc}}(2\omega, \mathbf{k}_2, \mathbf{r}_i) \cdot \left(\chi^{(2)}_{\mathrm{loc}}(\mathbf{r}_i) : \mathbf{E}^2_{\mathrm{loc}}(\omega, \mathbf{k}_1, \mathbf{r}_i)\right) , \tag{4.1}$$

where $\mathbf{r}_i$ is the position vector of ith evaluation point. The signal irradiance is then calculated as

$$I(2\omega) \propto \left|E_{\mathrm{far,tot}}(2\omega)\right|^2 . \tag{4.2}$$

We note here that we do not calculate exact values for $I(2\omega)$, but rather the resonance enhancement factors which we get by comparing the on- and off-resonance results.

4.2 Transmission Measurements

In this Thesis, we characterize our metamaterials by measuring their transmission and SHG emission spectra. The transmission spectra reveal the spectral locations of resonances, such as LSPRs and SLRs, which boost the nonlinear interaction and induce phase-shifts to the interacting light beams. If the occurring resonances are where they were designed to be, we can then study if the nonlinear responses are as expected.

The transmission spectra in **Publications I** and **II** were measured using a setup illustrated in Fig 4.3. We used a halogen lamp (SLS201 300-2600 nm, Thorlabs) as a broadband and collimated light source. As our metasurfaces are typically anisotropic, we controlled the polarization of the incident light with a polarizing beamsplitter (PBS), which allowed us to measure transmission spectra for different linear polarization states. The sample itself was placed on a goniometer, which was connected to a combination of translation and rotation stages. This enabled accurate control of sample position, orientation, and especially, angle-depended measurements. After passing through the sample, the light beam is guided further with a lens pair, which both expand the beam and image the sample plane on an iris. The iris was set on the focal plane of our imaging camera, which we used to identify the correct sample. By adjusting the iris aperture size, we made sure that only the light passing through the wanted sample was guided further. After the iris, we placed a flip mirror, which guided light either towards the imaging camera or a spectrometer. Before the spectrometer, the light beam was focused on a multimode fiber connected to the spectrometer.

For **Publications I** and **II**, we used two spectrometers, AvaSpec-ULS-RS-TEC (Avantes) and NIR128L-1.7 (Control Development), to measure transmission spectra in VIS and NIR regions, respectively. For measuring LSPRs and relatively broadband SLRs ($Q \leq 100$), these spectrometers had adequate spectral resolutions. For SLRs with significantly higher Q-factors ($Q \sim 1000$), detectors with much higher spectral resolution ($\Delta\lambda_{\mathrm{res}} < 1\,\mathrm{nm}$), such as optical spectrum analyzers (OSAs), are needed. However, the iris in our setup decreases the amount of collected light to a level that cannot be detected by a typical OSA, when using a halogen lamp. Furthermore, light from the halo-

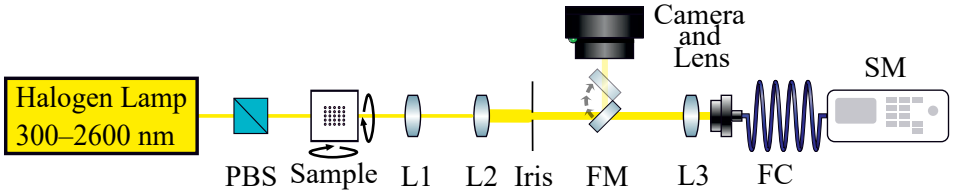

Figure 4.3 The setup for measuring transmission spectra in **Publications I** and **II** had a halogen lamp as a broadband light source, a camera for imaging the measured sample, and a spectrometer (SM) as a detector. For angle-dependent measurements, the sample was placed on a stage composed of rotation and translation stages, and of a goniometer. Additionally, the setup included a polarizing beam splitter (LP), lenses (L), a flip mirror (FM), and a fiber coupler (FC).

gen lamp is not coherent enough to excite extremely high-Q resonances [109]. Therefore, it would be wise to substitute the broadband halogen lamp by coherent light sources, such as supercontinuum lasers, when investigating SLRs with $Q \geq 1000$ [104].

4.3 Second-harmonic Generation Measurements

The SHG measurements in **Publications I** and **II** were conducted with the setup illustrated in Fig. 4.4. There, we used an optical parametric oscillator (OPO) pumped with a titanium sapphire (Ti:Sapph) femtosecond (fs) laser as a wavelength-tunable (1000–1300 nm) laser source. To maintain constant average power during a wavelength scan of the OPO, we used a combination of a motorized achromatic halfwave plate (HWP), PBSs, and a photodiode, which have been previously calibrated for all the used wavelengths. This approach allows an accurate power control up to 100 mW at each wavelength. We also wanted to ensure that all the incident laser power comes from the OPO. Thus, we placed a long pass filter (LPF) and a dichroic mirror (DM) to block all the remaining Ti:Sapph laser light and its possible harmonics.

In addition to the incident laser power and wavelength, it is also important to control its polarization and intensity. In our research, this is rather straightforward as we used linearly polarized light with normal Gaussian distribution. To control the polarization, we simply used another achromatic HWP. To ensure a clean Gaussian distribution and tight focus, we expanded the laser beam with two lenses set in a confocal configuration, with a pinhole placed in the

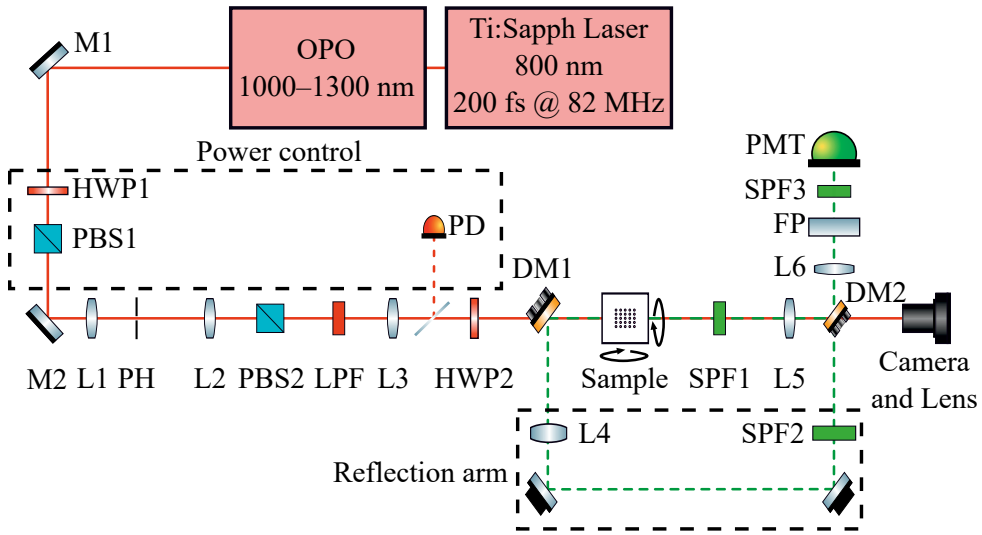

Figure 4.4 A schematic of the setup used for measuring SHG spectra for **Publications I** and **II**. As a tunable laser source we used an optical parametric oscillator (OPO), pumped with a titanium sapphire (Ti:sapph) femtosecond laser. We used a typical CMOS camera for imaging the sample, while the SHG signal was detected with a photomultiplier tube (PMT). The setup also includes mirrors (M), half-wave plates (HWPs), polarizing beam-splitters (PBSs), lenses (L), a pinhole (PH), dichroic mirrors (DMs), a long-pass filter (LPF), short-pass filters (SPFs), and a film polarizer (FP). To measure backpropagating SHG signals, DM2 can be flipped.

focal plane. Then, we focused the laser beam on the sample using an achromatic lens (lens L3 in Fig. 4.4). The focal length of this lens should be selected carefully depending on the nature of the sample. For samples exhibiting high-Q resonances, it is better to use a lens with a long focal length, e.g., 500 mm in **Publication II**. If the sample exhibits broader resonances, as the samples for **Publication I** did, tighter focus should be considered to achieve high pump intensities.

Similar to the transmission setup, the sample itself was placed on a stage with goniometric, rotational, and translational components, and it was imaged with a typical CMOS camera. With this approach, we could make sure that the sample was in the focus of L3, that it was aligned with the incident polarization, and that by rotating the sample it would not shift away from the laser beam.

In our measurements, we used a photomultiplier tube (PMT) as a detector of the SHG signal. Since PMTs are extremely sensitive light detectors, and easily damageable by stray light, we conducted the measurement in dark conditions.

Furthermore, we ensure that only SHG signal from the sample would reach the PMT with the use of short-pass filters (SPFs) and DMs. Here, the DM1 was set to block any Ti:Sapph laser from the sample and also to guide backward SHG emission to the reflection arm of the setup. DM2 was then used to select which one of the SHG signals, the forward or backward, was measured by the PMT. To characterize the polarization of the emitted SHG signal, we placed a film polarizer in front of the PMT.

4.3.1 Estimation of the Effective Nonlinear Susceptibility

In **Publications I** and **II**, we used PMT model PMA-C 192-M (PicoQuant) driven by PMS-400A (Becker & Hickel) photon counting card. We calibrated the components such that one PMT count per second corresponded to an average SHG power of 5.2×10^{-18} W [137]. The measured PMT count and SHG power ($\mathcal{P}(2\omega)$) allows us to identify different enhancement mechanisms, such as phase-matching enhancement in **Publication I** or resonance enhancement in **Publication II**. However, further characterization of the NLO properties of the investigated metamaterials, especially defining the effective second-order susceptibility $\chi^{(2)}_{\text{eff}}$ requires further processing.

The first step toward quantifying $\chi^{(2)}_{\text{eff}}$ is to define the peak irradiance of the used pump laser beam

$$I_{\text{peak}}(\omega) = \frac{\mathcal{P}_{\text{peak}}(\omega)}{A_b}\,, \tag{4.3}$$

where $\mathcal{P}_{\text{peak}}(\omega)$ and A_b are the peak power and cross-section area of the pump beam, respectively.

First, we consider A_b which for a typical Gaussian laser beam, is given by $A_b = \frac{\pi}{2}(\frac{d}{2})^2$, where d is the beam diameter (at $1/e^2$ of the maximum intensity). The pump diameter at our OPO output is 2 mm, which is expanded to 10 mm by the lenses L1 and L2 (see Fig. 4.4). Then, we focus the beam with the lens L3, with focal length f. Using the typical Gaussian beam optics, we can then estimate d at the focal plane of the lens as follows [138]:

$$d = \frac{4\lambda f}{\pi d_0} \tag{4.4}$$

where d_0 is the beam diameter at the focusing lens.

Next, we consider $\mathcal{P}_{\text{peak}}(\omega)$ of our fs laser, which is connected to the average power $\mathcal{P}_{avg}(\omega)$ by

$$\mathcal{P}_{\text{peak}}(\omega) \approx \frac{\mathcal{P}_{avg}}{1.763\tau_p\nu_{\text{rep}}}\,, \tag{4.5}$$

where τ_p and ν_{rep} are the pulse duration and repetition rate of the pulsed laser, respectively. For our OPO, $\tau_p = 200\,\text{fs}$ and $\nu_{\text{rep}} = 82\,\text{MHz}$. The factor 1.763 takes into account the sech-shaped temporal profile. Now, we can rewrite Eq. (4.3) in terms of $\mathcal{P}_{avg}(\omega)$ as

$$I_{\text{peak}}(\omega) = \frac{\mathcal{P}_{avg}(\omega)}{1.763\tau_p\nu_{\text{rep}}A_b}\,. \tag{4.6}$$

In **Publication II**, we estimated $\chi^{(2)}_{\text{eff}}$ with a method detailed in [139] and later used with metamaterials [126, 140].

$$\begin{aligned}\mathcal{P}_{\text{peak}}(2\omega) =& \frac{2}{c_0\epsilon_0 A_b}\frac{[t^{(1)}_{ms}]^4[t^{(2)}_{ms}]^2[t^{(2)}_{sa}]^2}{n_2^2c_2^2}\mathcal{P}^2_{\text{peak}}(\omega)\left(\frac{2\pi L_c}{\lambda}\right)^2 \\ &\times\left(\frac{1}{2}\chi^{(2)}_{\text{eff}}\right)^2\frac{\text{sinc}^2\psi + R_1 + R_2}{1 + R_3 + R_4},\end{aligned} \tag{4.7}$$

where $\psi = (2\pi L_c/\lambda)(n_1c_1 - n_2c_2)$, L_c is the length of the nonlinear material, λ is the pump wavelength, and n_1 and n_2 are the refractive indices at the fundamental and SH frequencies, respectively. The terms c_1 and c_2 are given by $c_m = \sqrt{1-(1/n_m)^2\sin^2\theta}$, where θ is the incident angle. In most of our measurements, we have $\theta = 0^\circ - 10^\circ$, and thus, we can approximate that $c_1 \approx c_2 \approx 1$. In the case of metamaterials and other nanophotonic components $L_c \ll \lambda$, and consequently, $\psi \approx 0$ and $\text{sinc}^2\psi \approx 1$. The terms $R1...R4$ are related to multiple reflections, that can be often neglected with metamaterials.

The terms $t^{(1)}_{ms}$ and $t^{(2)}_{ms}$ in Eq. (4.7) are the transmission coefficients of the nonlinear material at the fundamental and SH frequency, respectively. They are connected to the measured transmittance values by $T_\omega = \left|t^{(1)}\right|^2$ and $T_{2\omega} = \left|t^{(2)}\right|^2$. As we only consider the magnitude of the SH signal and neglect the signal propagation in the substrate, we can simply use the absolute values of $t^{(1)}$ and $t^{(2)}$ and rewrite the related parts in Eq. (4.7) as $[t^{(1)}_{ms}]^4 = T^2_\omega$ and $[t^{(2)}_{ms}]^2 = T_{2\omega}$. The third transmission coefficient $t^{(2)}_{sa}$ describes the substrate–air transmission.

Equation (4.7) is written in terms of peak powers and for the Gaussian unit system. In order to consider average powers, which can be directly measured, and to convert the formulation into the SI unit system, we need to modify the quotient $\mathcal{P}_{\text{peak}}(\omega)/A_b$ to include a factor of $\ln 2\sqrt{2\ln 2/\pi}/(2\nu_{\text{rep}}\tau_p)$. Finally, we can rewrite (4.7):

$$\mathcal{P}_{avg}(2\omega) = \frac{\ln 2}{4c_0\epsilon_0\nu_{\text{rep}}\tau_p}\sqrt{\frac{2\ln 2}{\pi}}\frac{T_\omega^2 T_{2\omega}[t_{sa}^{(2)}]^2}{n_2^2}\frac{\mathcal{P}_{avg}^2(\omega)}{A_b}\left(\frac{2\pi L_c}{\lambda}\right)^2\left(\chi_{\text{eff}}^{(2)}\right)^2, \quad (4.8)$$

from where we can solve for the $\chi_{\text{eff}}^{(2)}$.

5 RESULTS

In this Chapter, we summarize the results of the publications of this Thesis. We start with **Publication I**, where we used resonant phase-shifts to achieve phase matching in stacks of plasmonic metasurfaces. In **Publication II**, we utilized SLRs to achieve tunable multiply-resonant enhancement of SHG. Together, these two publications show how conventional enhancement methods, phase matching and multiply-resonant enhancement, can be brought to metamaterial devices. In **Publication III**, we propose a method to achieve broadband frequency conversion with narrowband SLRs, which surpasses the time–bandwidth limit of conventional narrowband resonators.

5.1 Phase-matching of Nonlinear Responses from Stacked Metasurfaces

In **Publication I**, we demonstrated phase matching for backward SHG from stacks of plasmonic metasurfaces, separated from each other by distance h (see Fig. 5.1). An incident pump beam with electric field amplitude of $E(\omega)$ induces SHG on a metasurface layer with effective susceptibility $\chi^{(2)}_{ms}$. Therefore, there are two beams interacting and propagating through the stacked metamaterial, pump and signal beams oscillating at the fundamental (ω) and doubled frequency (2ω), respectively. Both beams undergo phase changes due to propagation ($\varphi_{\omega_i} = k_{\omega_i} h$) and scattering at the metasurfaces (δ_{ω_i}). For backward SHG, we can now write the phase mismatch as

$$\Delta k = 2(\varphi_\omega + \delta_\omega) + \varphi_{2\omega} + \delta_{2\omega}\,. \tag{5.1}$$

The overall SHG response of the stacked metasurface is the superposition of each metasurface signal, modified by transmittances at the interacting frequen-

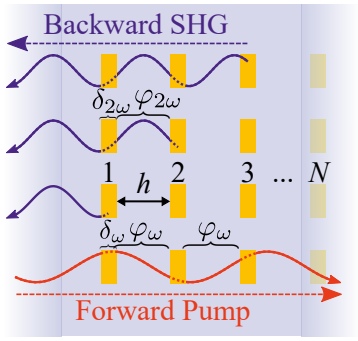

Figure 5.1 A schematic for backward SHG from N evenly spaced plasmonic metasurfaces, each separated by distance h from each other. Phase-matching of this process depends on phase shifts at the interacting frequencies ω and 2ω. Here, φ_i terms correspond to the phase accumulation during propagation. δ_i terms correspond to phase changes induced by the individual nanoparticle responses, here LSPRs [**Publication I**].

cies ($T(\omega_i)$) and Δk:

$$SHG \propto \left| \sum_{J=1}^{N} T^J(\omega) T^{J/2}(2\omega) e^{iJ\Delta k} \chi^{(2)}_{ms} E^2(\omega) \right|^2 . \tag{5.2}$$

From this equation, we can clearly see that SHG achieves its maximum and coherent build-up during propagation, when Δk is an integer of 2π.

For experimental demonstration of our approach, we fabricated five stacked metamaterials consisting of $N = 1, 2, ..., 5$ adjacent gold NP layers (see Fig. 5.2). Each NP array consisted of V-shaped NPs with arm length $L = 190\,\text{nm}$, arm width $w = 100\,\text{nm}$, and thickness $d = 20\,\text{nm}$, which were arranged in a rectangular array with periodicity of $p = 1000\,\text{nm}$. The first NP array was fabricated on a glass substrate ($n = 1.45$) and a spacer layer of spin-on glass ($n = 1.45$) with $h = 225\,\text{nm}$ was spin-coated between each layer.

With the NP parameters listed above, the investigated metasurface exhibits fundamental LSPRs centered at 974 nm and 1206 nm for y- and x-polarized light, respectively (see Fig 5.3 a). For both input polarizations, the sample exhibits higher-order LSPRs at shorter wavelengths, but still above the investigated signal wavelengths (500–650 nm). By fitting Lorentzian profiles into the measured transmission spectra (blue lines in Fig. 5.3 a), we can extract δ_ω and $\delta_{2\omega}$ terms (red lines in Fig. 5.3 a). As expected, the φ_ω is π at wavelengths shorter than the LSPR wavelengths, 0 at longer wavelengths, and goes through

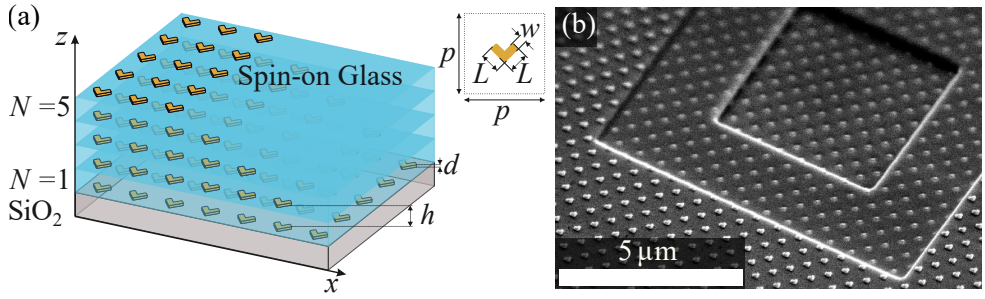

Figure 5.2 (a) A schematic of fabricated sample consisting of 5 stacked metasurfaces, separated by $h = 225\,\mathrm{nm}$. Each metasurface consisted of V-shaped gold NPs arranged in a square lattice with periodicity $p = 1000\,\mathrm{nm}$. Here, nanoparticle dimensions are $L = 190\,\mathrm{nm}$, $w = 100\,\mathrm{nm}$, and $d = 20\,\mathrm{nm}$. (b) An oblique-angle scanning electron micrograph of an etched sample consisting of three metasurface layers [**Publication I**].

an abrupt change near them. The Lorentzian fits also allow us to estimate $\chi^{(2)}_{ms}$. Due to symmetry rules for V-shaped NPs (see Section 3.4), we estimate the tensors $\chi^{(2)}_{yyy}$ and $\chi^{(2)}_{yxx}$.

We then inserted the measured and derived values into Eq. (5.2), to estimate the SHG response using a pump wavelength range of 1000–1300 nm. For the SHG process corresponding to $\chi^{(2)}_{yyy}$ the phase-matching condition was not fulfilled in this wavelength region, but for the process corresponding to $\chi^{(2)}_{yxx}$ it was fulfilled at 1135 nm. For this process, the maximum SHG response from a single layer was at LSPR wavelength of 1206 nm (see Fig 5.3 b). However, the maximum signal was achieved with 5 layers at the phase-matching wavelength of 1135 nm, where SHG signal builds up with the increasing number of layers.

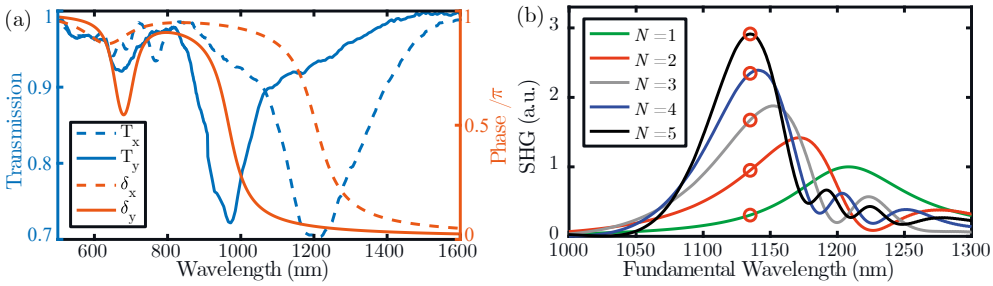

Figure 5.3 (a) Measured transmission (blue) and calculated phase shift (red) for a single NP array. The sample exhibits LSPRs at 974 nm and 1206 nm for y- (solid) and x-polarized (dashed) light, respectively. (b) The transmission and phase shifts can be used to semi-analytically estimate SHG response from stacks of metasurfaces. The calculated SHG signal builds up with increasing N at the phase-matching wavelength of 1135 nm [**Publication I**].

Next, we measured the SHG response from our samples using the setup shown in Fig. 4.4. To avoid sample damage, we limited our average input power to 10 mW. Now, the maximum signal with 5 layers is at 1141 nm, which is slightly shifted from the predicted phase-matching wavelength (see Fig. 5.4 a). We believe that this difference in estimated and measured phase-matching wavelengths is due to interparticle coupling between the adjacent NP layers.

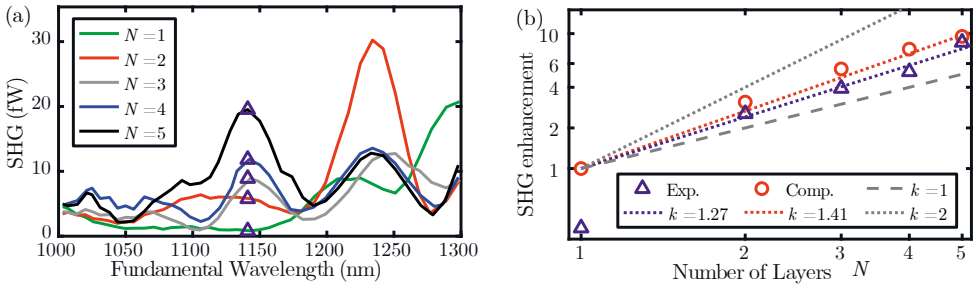

Figure 5.4 (a) Measured SHG emission spectra from the stacked metamaterials. The measured SHG singal grows with number of layers N at the phase-matching wavelength of 1141 nm. (b) At their respective phase-matching wavelengths, both the calculated (red spheres) and measured (blue triangles) signals scale superlinearly as a function of N, indicated by linear fits with slope $k > 1$ on the logarithmic scale [**Publication I**].

A closer analysis of the evolution of the SHG signals reveals that they scale super-linearly with increasing N (see Fig. 5.4 b). For the calculated response, $SHG_{\mathrm{comp}} \propto N^{1.41}$, and for the measured signal, $SHG_{\mathrm{exp}} \propto N^{1.27}$. Due to the transmission losses at the interacting wavelengths, the responses do not scale quadratically, which would be the case with phase matching in transparent materials (see Eq. (2.54)). Therefore, for utilizing our approach with much larger N, it would be advisable to design the phase matching to more transparent wavelengths.

To summarize, we experimentally demonstrated phase matching of backward SHG from stacks of plasmonic metasurfaces. We especially utilized the resonant phase shifts arising from LSPRs of the individual metasurfaces. Our approach shows promise to increase the efficiencies of nonlinear processes in plasmonic structures. Furthermore, other resonances could be also used to fulfill phase-matching conditions. Especially SLRs, which offer more accurate phase control through narrow linewidths and potential 2π phase jumps near the resonance, seem promising. Finally, the technique demonstrated here can be applied for other nonlinear processes. For example, the backward SHG could be even

further enhanced to achieve cascaded THG for efficient UV laser sources [73].

5.2 Multiply-resonant Enhancement of Nonlinear Responses using Surface Lattice Resonances

For **Publication II**, we designed and fabricated a multiply-resonant metasurface consisting of V-shaped aluminum NPs on a glass substrate ($n = 1.5$). The NP parameters were this time set to $L = 100\,\text{nm}$, $w = 70\,\text{nm}$, and $d = 40\,\text{nm}$ (see Fig. 5.5 a). To achieve homogeneous surroundings enabling SLRs, the NP array was covered with an index-matching oil. The choice of the NP material and size ensured that LSPRs excited using y- and x-polarized light would be below the investigated SHG signal wavelength range of 500–650 nm and pump wavelength range of 1000–1300 nm, respectively. This also allowed us to set lattice periodicities p_x and p_y such that we could have the x-polarized parallel SLR at the SHG pump wavelength range and the y-polarized SLR at the signal wavelength range. In other words, we designed the sample for multiply-resonant enhancement of the effective susceptibility component $\chi^{(2)}_{yxx}$. For the sample we discuss here, $p_x = 398\,\text{nm}$ and $p_y = 813\,\text{nm}$. At normal incidence, the metasurface thus exhibits parallel SLRs (see Eqs. (3.6) and (3.7)) at 1220 nm and 609 nm for x- and y-polarized light, respectively (see Fig. 5.5 b and c). In accordance to Eq. (3.8), the metasurface also exhibits the diagonal SLR for both polarizations at 546 nm.

As is seen from the transmission dispersion graphs in Figs. 5.6 a and b, x- and y-polarized SLRs shift from their normal-incidence values when the sample is tilted about y- and x-axis, respectively. From the transmission dispersion graphs, we can also identify the wavelength and incident angle combinations, for which the multiply-resonant condition $\lambda_x(\theta_y) = 2\lambda_y(\theta_x)$ is fulfilled. For normally incident pump ($\theta_y = 0°$), the y-polarized SLR is located near the desired wavelength of 610 nm at three θ_x angles. The first one is conveniently at normal incidence, where the parallel y-polarized SLR is located at 609 nm. Then, at $\theta_x = \pm 11°$, the diagonal SLR has shifted to 610 nm, and the multiply-resonant condition is again fulfilled.

To confirm the multiply-resonant enhancement on our sample, we measured its SHG response with the setup described in Fig. 4.4, using incident power

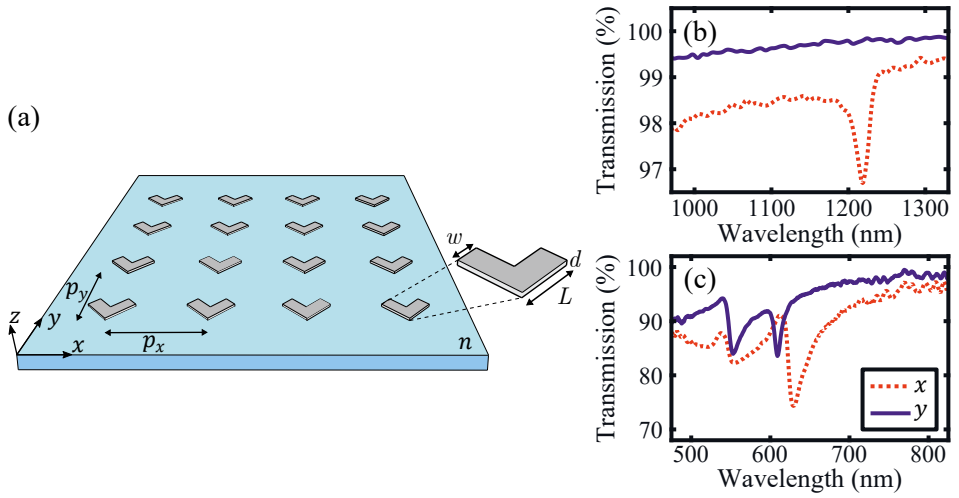

Figure 5.5 (a) A schematic of a multiply-resonant metasurface consisting of V-shaped aluminum NPs arranged in a rectangular array embedded in homogeneous glass surrounding (refractive index $n = 1.5$). Here, $L = 100\,\text{nm}$, $w = 70\,\text{nm}$, $d = 40\,\text{nm}$, $p_x = 398\,\text{nm}$, and $p_y = 813\,\text{nm}$. (b) and (c) measured transmission spectra for x- (red dashed lines) and y-polarized (blue solid lines) light at normal incidence. The metasurface exhibits parallel SLRs at 1220 nm and 609 nm for x- and y-polarized light, respectively. The sample also exhibits diagonal SLR at 546 nm for both input polarizations [**Publication II**].

level of 75 mW. In this experiment, the sample was placed on a combination of goniometric and rotational stages, allowing us to accurately control θ_y and θ_x. By setting $\theta_y = 0°$ and changing θ_x, we recorded the SHG dispersion graph corresponding to the $\chi^{(2)}_{yxx}$ process (see Fig. 5.6 c). In this graph, we can see how SLRs at both pump and signal wavelengths enhance the SHG response. Firstly, the x-polarized SLR boosts SHG at 1220 nm at each θ_x value. Secondly, the SHG response follows the dispersion of y-polarized SLRs. Thirdly and most importantly, the SHG response reaches its maximum at multiply-resonant conditions, i.e., with pump at 1220 nm and $\theta_x = [0°, \pm 11°]$.

At the multiply-resonant conditions, the signal is 10-fold enhanced when compared to the off-resonance level, reaching the power level of 5.8 fW. This corresponds to conversion efficiency of 7.7×10^{-14} and $\chi^{(2)}_{yxx} = 0.4\,\text{pm/V}$ (see Eq. (4.8)). This considerably low signal level is mostly explained by the relatively weak and low-Q SLRs (extinction $\leq 5\%$ and $Q \approx 60$). Indeed with stronger and higher-quality SLRs, SHG response could be over 1000-fold enhanced, as was recently demonstrated by Beer et al [141].

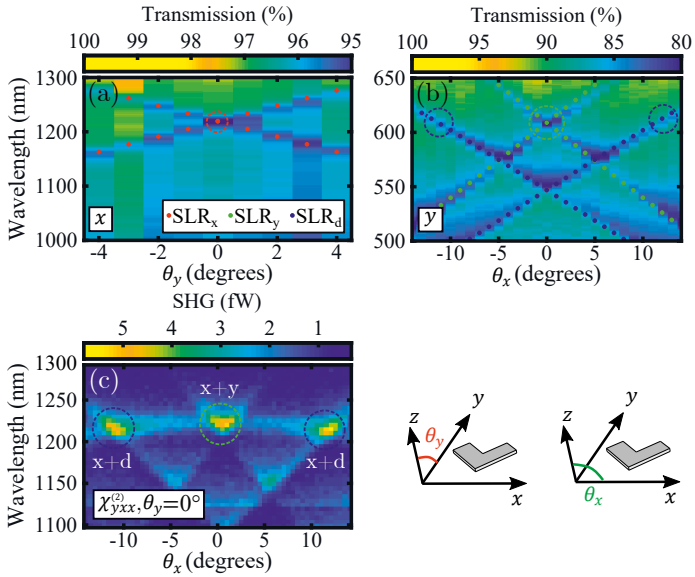

Figure 5.6 Dispersion graphs of transmission for (a) x- and (b) y-polarized light for the investigated sample. (c) Dispersion graph of SHG emission with x-polarized pump and y-polarized signal. (a)–(b) Parallel SLRs for x- (red dots) and y-polarized (green dots) light are shifted from their normal incidence values by tilting the sample along y-axis (θ_y) and x-axis (θ_x). The diagonal SLR also shifts with the tilt of the sample (blue dots). (c) SHG emission is boosted by the SLRs at both pump and signal wavelengths. The maximum signal occurs at multiply-resonant conditions (dashed circles). With incident angle set at $\theta_y = 0°$, this condition is fulfilled for pump wavelength of 1220 nm at three emission angles θ_x. At $\theta_x = 0°$ (green circle), multiply-resonant condition is fulfilled with parallel SLRs. At $\theta = \pm 11°$ (blue circles), it is fulfilled with diagonal SLR at the signal wavelength [**Publication II**].

Despite the low signal levels, our proof-of-principle demonstration illuminates the potential of SLRs and aluminum for nonlinear plasmonics. First of all, our samples could handle much higher input powers than devices relying on lossy LSPRs. Futhermore, the utilization of SLR dispersion also enables post-fabrication tuning of multiply-resonant conditions, which cannot be achieved with non-dispersive responses, such as LSPRs and Mie-type resonances. Overall, our results in **Publication II** can pave the path toward low-loss and tunable nonlinear plasmonic devices.

5.3 Broadband Frequency Conversion using high-Q Surface Lattice Resonances

As is described by the NLST, nonlinear optical responses can be enhanced dramatically with high-Q and narrowband resonances, such as SLRs, guided-mode resonances, or bound states in the continuum. On the other hand, nonlinear processes scale with higher powers of the pump intensities, making ultrashort pulses with high peak intensities most suitable. Unfortunately, ultrashort pulse duration means automatically broad spectral features, which limits the coupling efficiency of broadband pulses into narrowband resonators. This common disadvantage is known as the time–bandwidth limit [142]. In **Publication III**, we propose a metasurface-based method to overcome this limit, by utilizing a temporal focusing scheme and plasmonic SLRs (see Fig 5.7).

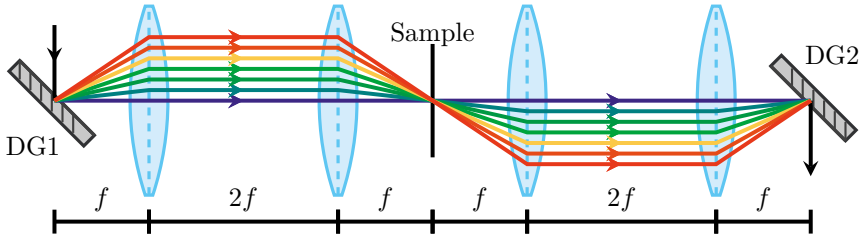

Figure 5.7 A schematic of the proposed setup for broadband frequency conversion. A diffraction grating (DG1) splits the incident pulse into spectral components that are then focused on the sample by a $4f$-correlator. Each spectral component arrives at different incidence angle, allowing each of them to couple efficiently to dispersive SLR modes. Light-matter interaction between each spectral component is then dramatically enhanced, including frequency conversion via sum-frequency generation. The generated signal components can be again combined into a broadband pulse by another $4f$-correlator and diffraction grating (DG2) [**Publication III**].

The first part of our proposed method is the setup shown in Fig. 5.7, which follows a temporal focusing scheme [143, 144]. It consists of two diffraction gratings (DGs), two lens pairs in $4f$-configurations, and a metasurface exhibiting dispersive SLRs. First, the incident broadband pump pulse hits the first DG, splitting into spectral components. Then, each spectral component is guided toward the sample, each at different incident angle θ. If the spatial dispersion of the spectral components matches the dispersion of the sample SLRs, each spectral component can be efficiently coupled into the metasurface. Conse-

quently, the local fields at each interacting wavelength are enhanced, boosting SFG between different spectral components (see Eq. (3.9)). This results in the generation of numerous spectral components at the SF wavelengths. These signal components can then be combined into a single broadband pulse by another lens pair and a DG.

The second part our approach is the SLR-exhibiting metasurface. For the numerical investigations of this work, we designed and simulated the linear and nonlinear responses of a metasurface illustrated in Fig 5.8 a. It consists of V-shaped aluminum NPs arranged in a rectangular lattice embedded in homogeneous glass surroundings ($n = 1.5$). Here, the NP and lattice parameters are set as $L = 120\,\text{nm}$, $w = 70\,\text{nm}$, $d = 40\,\text{nm}$, $p_x = 660\,\text{nm}$, and $p_y = 400\,\text{nm}$. At normal incidence, they give rise to LSPR near 570 nm and SLR at 1002 nm for y-polarized light. This SLR had the linewidhth $\Delta\lambda_{SLR} \approx 2\,\text{nm}$ corresponding to $Q = 500$.

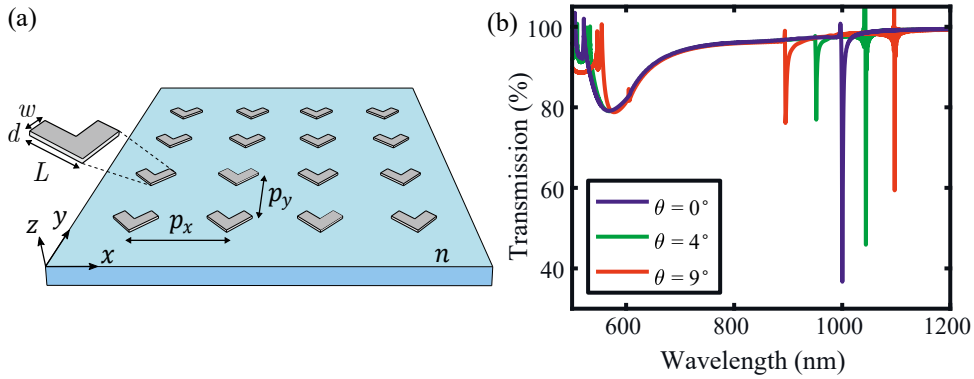

Figure 5.8 (a) The simulated metasurface consisted of V-shaped aluminum NPs arranged in a rectangular array in homogeneous glass surroundings ($n = 1.51$). Here, $L = 120\,\text{nm}$, $w = 70\,\text{nm}$, $d = 40\,\text{nm}$, $p_x = 660\,\text{nm}$, and $p_y = 400\,\text{nm}$. (b) The simulated transmission spectra for y-polarized light reveal a broader LSPR near 570 nm and a much narrower SLR at 1002 nm, at normal incidence (blue). By changing the incident angle θ (green and red), the normal-incidence SLR peak splits into two which shift to opposite directions. With $\theta = 9°$, the two SLRs form at 896 nm and 1100 nm [**Publication III**].

As we showed experimentally in **Publication II**, SLRs can be tuned by changing θ. As we see in Fig 5.8 b, nonzero θ splits the SLR peak into two and shifts them to opposite directions from the resonance wavelength of normally-incident light. In this work, we considered angles between 0° and 9°. At $\theta = 9°$, the two SLRs are located at 896 nm and 1100 nm. However, the SLRs at longer

wavelengths (>1000 nm) are associated with much higher Q-factors than the ones at shorter wavelengths (<1000 nm). Therefore, we only considered the SLRs at the longer wavelengths for our frequency conversion calculations.

Next, we calculated the SFG response of our sample design using NLST (see Section 4.1). In our calculations, we used broadband pump pulses centered at 1050 nm with linewidth $\Delta\lambda_L = 100\,\text{nm}$. First, we calculated the SFG response in situations where the entire pulse arrives at the sample at one incident angle. In such cases, SFG is only efficient for the degenerate process, i.e., SHG with pump beams at the SLR wavelength that depends on the incident angle (see Fig 5.9 a).

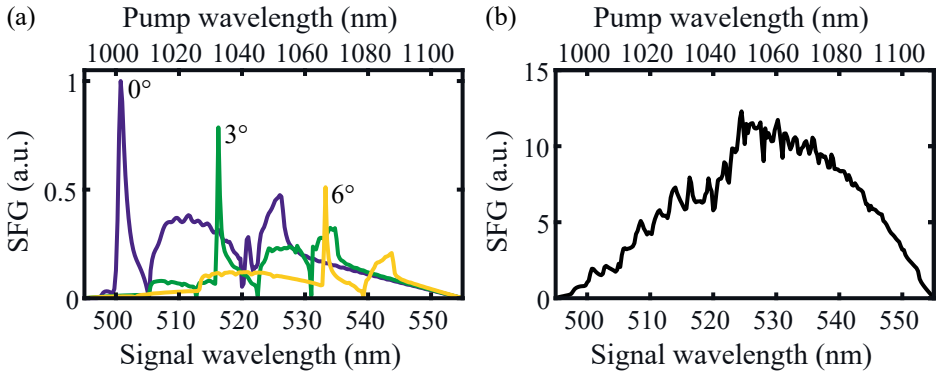

Figure 5.9 Frequency conversion of a broadband laser pulse with bandwidth of 100 nm via SFG in an SLR-exhibiting metasurface. (a) Without the proposed scheme (see Fig 5.7), the entire laser pulse arrives at the metasurface at a single angle of incidence. Consequently, only the degenerate SFG with both pump photons at the same SLR wavelength is enhanced. (b) When the proposed setup is used, the incident laser pulse is split into spectral components that are each coupled into a dispersive SLR, boosting the light-matter interaction between the spectral components. Consequently, SFG is enhanced over a broad spectral range with cumulative response boosting it even further. Overall, this results in broadband frequency conversion with signal bandwidth of 40 nm. All signals are normalized to the maximum SFG signal when all spectral components arrive at normal incidence (blue line) [**Publication III**].

Next, we calculated the SFG response for our proposed setup. We assumed that the pump beam was split into 10 spectral components with 5 nm bandwidths. We also assumed that each pulse arrives at the metasurface simultaneously and at θ that matches the SLR dispersion. Consequently, SLRs enhanced the local fields at each pump wavelength, boosting the SFG between all the possible combinations. The numerous interactions combined cumulatively into

significantly stronger signals, when compared to our calculations without the proposed setup. More importantly, they resulted in a broadband SFG signal with $\Delta\lambda_{SFG} = 40\,\text{nm}$ centered at 525 nm (see Fig 5.9 b).

To summarize, we proposed a method for broadband frequency conversion based on nonlinear optics, high-Q SLRs, and temporal focusing techniques. We numerically showed how our approach can far surpass the typical time–bandwidth limit associated with narrowband resonators. Therefore, our approach is not limited to nonlinear optical processes. Instead, it can be utilized for any optical processes involving ultrashort laser pulses.

6 CONCLUSIONS AND OUTLOOK

In this Dissertation, we investigated nonlinear optical properties of plasmonic metamaterials, consisting of gold or aluminum nanoparticles (NPs). We utilized their intrinsic responses, especially localized surface plasmon resonances (LSPRs) and surface lattice resonances (SLRs) to boost and control nonlinear responses. We especially aimed to progress the field of plasmonics with two approaches: bringing known enhancement methods to metamaterial components, and proposing novel functionalities beyond the reach of conventional nonlinear photonic components. Our findings are detailed in **Publications I**, **II**, and **III**.

In **Publication I**, phase matching of backward second-harmonic generation (SHG) in stacks of evenly spaces metasurfaces was demonstrated. The phase matching was achieved with the phase-engineering capabilities of plasmonic NPs. Especially, phase shifts induced by LSPRs of the investigated metamaterial were utilized. The results show promise for increasing the conversion efficiencies of plasmonic metamaterials through multilayer structures, or alternatively, through multipass configurations [145, 146].

Publication II was a proof-of-principle demonstration of multiply-resonant enhancement of SHG using solely SLRs. Beyond the first-ever demonstration, our results also showed the potential of aluminum for nonlinear nanophotonics, while simultaneously overcoming the low damage threshold usually associated with plasmonic structures. Most importantly, the presented results demonstrated a simple method for post-fabrication tuning of the multiply-resonant condition through the spatial dispersion of SLRs.

In **Publication III**, a metasurface-based method for frequency conversion of ultrashort laser pulses via SFG was proposed. Our approach relies on high-Q SLRs and their dispersion, and on a scheme based on temporal focusing. The presented numerical results show how the proposed approach can poten-

tially surpass the time–bandwidth limit typically associated with narrowband resonators. Therefore, the proposed approach could be utilized not only for nonlinear optics, but for any processes involving ultrashort laser pulses.

6.1 Outlook

In this Thesis, all of the presented work focused on the processes of SHG and SFG. However, the demonstrated and proposed techniques could be applied for numerous other multiwavelength nonlinear processes, such as spontaneous parametric down-conversion, difference-frequency generation, and cascaded third-harmonic generation [34, 147]. Successful demonstration of these processes could pave the way toward developing nanophotonic components for photon pair generation, and for the generation of laser light at THz and UV regimes.

The resonant phase control techniques that were used in **Publication I** to achieve phase matching could be readily applied for other photonic techniques as well. For example, one could design a metasurface where the resonant phase shift would vary along the metasurface. Such structures could be used for steering, lensing, or structuring the generated nonlinear signal [148–150]. Lensing and beam-steering functionalities would be beneficial for coupling nonlinear responses with waveguide structures and other microphotonic structures [151–153]. Nonlinear generation of structured light could be used in quantum communication and nonlinear holography [154, 155].

Ultimately, the high-Q resonance-based enhancement and resonant phase-control could be utilized in a single multifunctional metamaterial component. For example, one could envisage a design where high-Q SLRs at pump wavelenghts would boost the nonlinear signal, while a phase-controlling resonance at the signal wavelength would structure the generated signal. Such devices could be easily tunable through SLR dispersion or via controlling the refractive index profile surrounding the metasurface [156]. Such devices would help to address the main issues of nonlinear plasmonic devices, i.e., their inefficiency and lack of tunability, while surpassing the capabilities of classical components through multifunctionality.

REFERENCES

[1] Isaac Newton. *Opticks*. Dover Press, 1704.

[2] A. Einstein. "Über einen die Erzeugung und Verwandlung des Lichtes betreffenden heuristischen Gesichtspunkt". In: *Annalen der Physik* 322.6 (1905), pp. 132–148.

[3] Donna Strickland and Gerard Mourou. "Compression of amplified chirped optical pulses". In: *Optics Communications* 55.6 (1985), pp. 447–449.

[4] Philippe Antoine, Anne L'Huillier, and Maciej Lewenstein. "Attosecond Pulse Trains Using High–Order Harmonics". In: *Phys. Rev. Lett.* 77 (1996), pp. 1234–1237.

[5] Bill Corcoran, Mengxi Tan, Xingyuan Xu, Andreas Boes, Jiayang Wu, Thach G. Nguyen, Sai T. Chu, Brent E. Little, Roberto Morandotti, Arnan Mitchell, and David J. Moss. "Ultra-dense optical data transmission over standard fibre with a single chip source". In: *Nature Communications* 11 (2020).

[6] J.N. Bardsley. "International OLED technology roadmap". In: *IEEE Journal of Selected Topics in Quantum Electronics* 10.1 (2004), pp. 3–9.

[7] Jaehee Cho, Jun Hyuk Park, Jong Kyu Kim, and E. Fred Schubert. "White light-emitting diodes: History, progress, and future". In: *Laser & Photonics Reviews* 11.2 (2017), p. 1600147.

[8] Joseph A Castellano. *Liquid gold: the story of liquid crystal displays and the creation of an industry*. World Scientific, 2005.

[9] Jane Hodgkinson and Ralph P Tatam. "Optical gas sensing: a review". In: *Measurement Science and Technology* 24.1 (2012), p. 012004.

[10] Jim Larsson, Joakim Bood, Can T. Xu, Xiong Yang, Robert Lindberg, Fredrik Laurell, and Mikkel Brydegaard. "Atmospheric CO2 sensing using Scheimpflug-lidar based on a 1.57-μm fiber source". In: *Opt. Express* 27.12 (2019), pp. 17348–17358.

[11] Artur K. Ekert. "Quantum cryptography based on Bell's theorem". In: *Phys. Rev. Lett.* 67 (1991), pp. 661–663.

[12] Manuel Erhard, Robert Fickler, Mario Krenn, and Anton Zeilinger. "Twisted photons: New quantum perspectives in high dimensions". In: *Light: Science and Applications* 7 (2018).

[13] A. B. Zylstra et al. "Burning plasma achieved in inertial fusion". In: *Nature* 601 (2022), pp. 542–548.

[14] Elsa Garmire. "Nonlinear optics in daily life". In: *Opt. Express* 21.25 (2013), pp. 30532–30544.

[15] Y. R. Shen. *The Principles of Nonlinear Optics*. 1st. New York: Wiley, 1984. ISBN: 0471889989.

[16] Robert W. Boyd. *Nonlinear optics*. San Diego: Academic Press, 2020. ISBN: 9780128110034.

[17] Govind P. Agrawal. *Nonlinear Fiber Optics*. Elsevier, 2019. ISBN: 9780128170434.

[18] P. A. Franken, A. E. Hill, C. W. Peters, and G. Weinreich. "Generation of optical harmonics". In: *Physical Review Letters* 7.4 (1961), pp. 118–119.

[19] M. Bass, P. A. Franken, A. E. Hill, C. W. Peters, and G. Weinreich. "Optical Mixing". In: *Phys. Rev. Lett.* 8 (1962), pp. 18–18.

[20] Kenneth E. Niebuhr. "Generation of laser axial mode difference frequencies in a nonlinear dielectric". In: *Applied Physics Letters* 2 (1963), pp. 136–137.

[21] S. E. Harris, M. K. Oshman, and R. L. Byer. "Observation of Tunable Optical Parametric Fluorescence". In: *Phys. Rev. Lett.* 18 (1967), pp. 732–734.

[22] Paul G. Kwiat, Klaus Mattle, Harald Weinfurter, Anton Zeilinger, Alexander V. Sergienko, and Yanhua Shih. "New High-Intensity Source of Polarization-Entangled Photon Pairs". In: *Phys. Rev. Lett.* 75 (1995), pp. 4337–4341.

[23] Carlota Canalias, Valdas Pasiskevicius, (SCI) Skolan för teknikvetenskap, Tillämpad fysik, KTH, and Laserfysik. "Mirrorless optical parametric oscillator". In: *Nature Photonics* 1.8 (2007), pp. 459–462.

[24] Y R Shen. "Surface properties probed by second-harmonic and sum-frequency generation". In: *Nature* 337 (1989), pp. 519–525.

[25] Ying Wang, Jun Xiao, Sui Yang, Yuan Wang, and Xiang Zhang. "Second harmonic generation spectroscopy on two-dimensional materials, *Invited*". In: *Opt. Mater. Express* 9.3 (2019), pp. 1136–1149.

[26] J E Midwinter and J Warner. "The effects of phase matching method and of uniaxial crystal symmetry on the polar distribution of second-order non-linear optical polarization". In: *British Journal of Applied Physics* 16.8 (1965), p. 1135.

[27] M. M. Fejer, G. A. Magel, D. H. Jundt, and R. L. Byer. "Quasi-phase-matched second harmonic generation: tuning and tolerances". In: *IEEE Journal of Quantum Electronics* 28.11 (1992), pp. 2631–2654.

[28] J. A. Giordmaine and R. C. Miller. "Optical parametric oscillation in the visible spectrum". In: *Applied Physics Letters* 9.8 (1966), pp. 298–300.

[29] A. Ashkin, G. Boyd, and J. Dziedzic. "Resonant optical second harmonic generation and mixing". In: *IEEE Journal of Quantum Electronics* 2.6 (1966), pp. 109–124.

[30] Costas M. Soukoulis and Martin Wegener. "Past achievements and future challenges in the development of three-dimensional photonic metamaterials". In: *Nature Photonics* 5.9 (2011), pp. 523–530.

[31] Martti Kauranen and Anatoly V. Zayats. "Nonlinear plasmonics". In: *Nature Photonics* 6.11 (2012), pp. 737–748.

[32] Basudeb Sain, Cedrik Meier, and Thomas Zentgraf. "Nonlinear optics in all-dielectric nanoantennas and metasurfaces: A review". In: *Advanced Photonics* 1 (2019).

[33] Junjun Ma, Fei Xie, Weijin Chen, Jiaxin Chen, Wei Wu, Wei Liu, Yuntian Chen, Wei Cai, Mengxin Ren, and Jingjun Xu. "Nonlinear Lithium Niobate Metasurfaces for Second Harmonic Generation". In: *Laser and Photonics Reviews* 15 (2021).

[34] Tomás Santiago-Cruz, Anna Fedotova, Vitaliy Sultanov, Maximilian A. Weissflog, Dennis Arslan, Mohammadreza Younesi, Thomas Pertsch, Isabelle Staude, Frank Setzpfandt, and Maria Chekhova. "Photon Pairs from Resonant Metasurfaces". In: *Nano Letters* 21 (2021), pp. 4423–4429.

[35] Anna Fedotova, Luca Carletti, Attilio Zilli, Frank Setzpfandt, Isabelle Staude, Andrea Toma, Marco Finazzi, Costantino De Angelis, Thomas Pertsch, Dragomir N. Neshev, and Michele Celebrano. "Lithium Niobate Meta-Optics". In: *ACS Photonics* 9 (2022), pp. 3745–3763.

[36] V. G. Kravets, A. V. Kabashin, W. L. Barnes, and A. N. Grigorenko. "Plasmonic Surface Lattice Resonances: A Review of Properties and Applications". In: *Chem. Rev.* 118.12 (2018), pp. 5912–5951.

[37] Anton D. Utyushev, Vadim I. Zakomirnyi, and Ilia L. Rasskazov. "Collective lattice resonances: Plasmonics and beyond". In: *Reviews in Physics* 6 (2021), p. 100051.

[38] D. C. Marinica, A. G. Borisov, and S. V. Shabanov. "Bound States in the Continuum in Photonics". In: *Phys. Rev. Lett.* 100 (2008), p. 183902.

[39] Arash Ahmadivand and Burak Gerislioglu. "Photonic and Plasmonic Metasensors". In: *Laser and Photonics Reviews* 16 (2022).

[40] Lior Michaeli, Shay Keren-Zur, Ori Avayu, Haim Suchowski, and Tal Ellenbogen. "Nonlinear Surface Lattice Resonance in Plasmonic Nanoparticle Arrays". In: *Physical Review Letters* 118.24 (2017), p. 243904.

[41] Aravind P. Anthur, Haizhong Zhang, Ramon Paniagua-Dominguez, Dmitry A. Kalashnikov, Son Tung Ha, Tobias W.W. Maß, Arseniy I. Kuznetsov, and Leonid Krivitsky. "Continuous Wave Second Harmonic Generation Enabled by Quasi-Bound-States in the Continuum on Gallium Phosphide Metasurfaces". In: *Nano Letters* 20 (2020), pp. 8745–8751.

[42] Xiaotian Zhang, Linye He, Xin Gan, Xiaocong Huang, Yixuan Du, Zhenshan Zhai, Zhuang Li, Yuanlin Zheng, Xianfeng Chen, Yangjian Cai, and Xianyu Ao. "Quasi-Bound States in the Continuum Enhanced Second-Harmonic Generation in Thin-Film Lithium Niobate". In: *Laser & Photonics Reviews* 16.9 (2022), p. 2200031.

[43] C. C. Gerry and Peter Knight. *Introductory quantum optics*. Cambridge, UK; New York: Cambridge University Press, 2005. ISBN: 9780511648373.

[44] James Clerk Maxwell. *A treatise on electricity and magnetism*. Oxford: Clarendon Press, 1873.

[45] Eugene Hecht. *Optics*. 4th. San Francisco: Addison Wesley, 2002. ISBN: 0321188780.

[46] Guang S. He. *Nonlinear Optics and Photonics*. Oxford University Press, 2015. ISBN: 9780198702764.

[47] D. Milovzorov and T. Suzuki. "Size-dependent second-harmonic generation by nanocrystals prepared by plasma-enhanced chemical-vapor deposition". In: *Applied Physics Letters* 75 (1999), pp. 4103–4105.

[48] Chao-Kuei Lee, Fu-Jen Kao, Shing Chung Wang, and Ci-Ling Pan. "Simultaneous Observation of Second-Harmonic Emission and Three-Photon Excited Photoluminescence from Hybrid Vapor Phase Epitaxy-Grown GaN Film". In: *Japanese Journal of Applied Physics* 40.12R (2001), p. 6805.

[49] D.C Dai, S.J Xu, S.L Shi, M.H Xie, and C.M Che. "Observation of both second-harmonic and multiphoton-absorption-induced luminescence in ZnO". eng. In: *IEEE photonics technology letters* 18.14 (2006), pp. 1533–1535.

[50] R. Czaplicki, A. Kiviniemi, M. J. Huttunen, X. R. Zang, T. Stolt, I. Vartiainen, J. Butet, M. Kuittinen, OJF Martin, and M. Kauranen. "Less Is More: Enhancement of Second-Harmonic Generation from Metasurfaces by Reduced Nanoparticle Density". In: *Nano Letters* 18.12 (2018), pp. 7709–7714.

[51] Solomon M. Saltiel, Andrey A. Sukhorukov, and Yuri S. Kivshar. "Chapter 1 - Multistep parametric processes in nonlinear optics". In: ed. by E. Wolf. Vol. 47. Progress in Optics. Elsevier, 2005, pp. 1–73.

[52] M. Marangoni, M. Lobino, and R. Ramponi. "Simultaneously phase-matched second- and third-harmonic generation from 1.55 μm radiation in annealed proton-exchanged periodically poled lithium niobate waveguides". In: *Opt. Lett.* 31.18 (2006), pp. 2707–2709.

[53] H. A. Lorentz. *The theory of electrons and its applications to the phenomena of light and radiant heat*. eng. 2. ed. New York: Dover, 1952.

[54] Robert C. Miller. "Optical second harmonic generation in piezoelectric crystals". In: *Applied Physics Letters* 5.1 (1964), pp. 17–19.

[55] Robert Czaplicki, Mariusz Zdanowicz, Kalle Koskinen, Hannu Husu, Janne Laukkanen, Markku Kuittinen, and Martti Kauranen. "Linear and nonlinear properties of high-quality l-shaped gold nanoparticles". In: *Nonlinear Optics Quantum Optics* 45.1-2 (2012), pp. 71–83.

[56] P. Guyot-Sionnest, W. Chen, and Y. R. Shen. "General considerations on optical second-harmonic generation from surfaces and interfaces". In: *Phys. Rev. B* 33 (1986), pp. 8254–8263.

[57] J.H. Hunt, P. Guyot-Sionnest, and Y.R. Shen. "Observation of C-H stretch vibrations of monolayers of molecules optical sum-frequency generation". In: *Chemical Physics Letters* 133.3 (1987), pp. 189–192.

[58] P. Guyot-Sionnest, J. H. Hunt, and Y. R. Shen. "Sum-frequency vibrational spectroscopy of a Langmuir film: Study of molecular orientation of a two-dimensional system". In: *Phys. Rev. Lett.* 59 (1987), pp. 1597–1600.

[59] Evgenia Kim, Feng Wang, Wei Wu, Zhaoning Yu, and Y. Ron Shen. "Nonlinear optical spectroscopy of photonic metamaterials". In: *Phys. Rev. B* 78 (2008), p. 113102.

[60] S. Roke, M. Bonn, and A. V. Petukhov. "Nonlinear optical scattering: The concept of effective susceptibility". In: *Physical review.B, Condensed matter and materials physics* 70.11 (2004).

[61] P. D. Maker, R. W. Terhune, M. Nisenoff, and C. M. Savage. "Effects of dispersion and focusing on the production of optical harmonics". In: *Physical Review Letters* 8.1 (1962), pp. 21–22.

[62] F ZERNIKE and J E Midwinter. *Applied nonlinear optics*. eng. 1973.

[63] M.V. Hobden and J. Warner. "The temperature dependence of the refractive indices of pure lithium niobate". In: *Physics Letters* 22.3 (1966), pp. 243–244.

[64] E. J. Lim, M. M. Fejer, and R. L. Byer. “Second-harmonic generation of green light in periodically poled planar lithium niobate waveguide”. In: *Electron. Lett.* 25.3 (1989), pp. 174–175.

[65] G. A. Magel, M. M. Fejer, and R. L. Byer. “Quasi-phase-matched second-harmonic generation of blue light in periodically poled LiNbO3”. In: *Applied Physics Letters* 56.2 (1990), pp. 108–110.

[66] M H Chou, I Brener, M M Fejer, E E Chaban, and S B Christman. “1.5-um-Band Wavelength Conversion Based on Cascaded Second-Order Nonlinearity in LiNbO Waveguides”. In: *IEEE Photonics Technol. Lett.* 11.6 (1999), pp. 653–655.

[67] Haim Suchowski, Dan Oron, Ady Arie, and Yaron Silberberg. “Geometrical representation of sum frequency generation and adiabatic frequency conversion”. In: *Phys. Rev. A - At. Mol. Opt. Phys.* 78.6 (2008), pp. 1–5.

[68] H. Suchowski, B. D. Bruner, A. Ganany-Padowicz, I. Juwiler, A. Arie, and Y. Silberberg. “Adiabatic frequency conversion of ultrafast pulses”. In: *Appl. Phys. B Lasers Opt.* 105.4 (2011), pp. 697–702.

[69] Jin U. Kang, Yujie J. Ding, William K. Burns, and Joseph S. Melinger. “Backward second-harmonic generation in periodically poled bulk LiNbO3”. In: *Opt. Lett.* 22.12 (1997), pp. 862–864.

[70] Xinhua Gu, Roman Y. Korotkov, Yujie J. Ding, Jin U. Kang, and Jacob B. Khurgin. “Backward second-harmonic generation in periodically poled lithium niobate”. In: *J. Opt. Soc. Am. B* 15.5 (1998), pp. 1561–1566.

[71] Xinhua Gu, Maxim Makarov, Yujie J. Ding, Jacob B. Khurgin, and William P. Risk. “Backward second-harmonic and third-harmonic generation in a periodically poled potassium titanyl phosphate waveguide”. In: *Opt. Lett.* 24.3 (1999), pp. 127–129.

[72] Patrick Mutter, Kjell Martin Mølster, Andrius Zukauskas, Valdas Pasiskevicius, and Carlota Canalias. “Efficient first-order quasi-phase-matched backward second-harmonic generation”. In: *Optics Letters* 48 (2023), p. 1534.

[73] Robert Lindberg, Xiao Liu, Andrius Zukauskas, Siddharth Ramachandran, and Valdas Pasiskevicius. “Simultaneous nonlinear wavelength and

mode conversion for high-brightness blue sources". In: *J. Opt. Soc. Am. B* 38.11 (2021), pp. 3491–3498.

[74] Cai Wenshan and Vladimir Shalaev. *Optical metamaterials fundamentals and applications*. eng. New York: Springer, 2010. ISBN: 1-282-83451-7.

[75] D. R. Smith, J. B. Pendry, and M. C. K. Wiltshire. "Metamaterials and Negative Refractive Index". In: *Science* 305.5685 (2004), pp. 788–792.

[76] Willie J. Padilla, Dimitri N. Basov, and David R. Smith. "Negative refractive index metamaterials". In: *Materials today* 9.7-8 (2006), pp. 28–35.

[77] Jason Valentine, Shuang Zhang, Thomas Zentgraf, Erick Ulin-Avila, Dentcho A. Genov, Guy Bartal, and Xiang Zhang. "Three-dimensional optical metamaterial with a negative refractive index". In: *Nature* 455 (2008), pp. 376–379.

[78] Minhua Li, Jian Song, and Fei Wu. "Ultra-compact chiral metamaterial with negative refractive index based on miniaturized structure". In: *Journal of Magnetism and Magnetic Materials* 426 (2017), pp. 150–154.

[79] Hannu Husu, Jouni Mäkitalo, Janne Laukkanen, Markku Kuittinen, and Martti Kauranen. "Particle plasmon resonances in L-shaped gold nanoparticles". In: *Optics Express* 18.16 (2010).

[80] Nanfang Yu, Patrice Genevet, Mikhail A. Kats, Francesco Aieta, Jean-Philippe Tetienne, Federico Capasso, and Zeno Gaburro. "Light Propagation with Phase Discontinuities: Generalized Laws of Reflection and Refraction". In: *Science* 334.6054 (2011), pp. 333–337.

[81] Patrice Genevet, Federico Capasso, Francesco Aieta, Mohammadreza Khorasaninejad, and Robert Devlin. "Recent advances in planar optics: From plasmonic to dielectric metasurfaces". In: *Optica* 4.1 (2017), pp. 139–152.

[82] Bing Shen, Peng Wang, Randy Polson, and Rajesh Menon. "Ultra-high-efficiency metamaterial polarizer". In: *Optica* 1.5 (2014), pp. 356–360.

[83] Sengul Gonulal, Muharrem Karaaslan, Emin Unal, Kemal Delihacioglu, Furkan Dincer, Erkan Tetik, and Cumali Sabah. "90° Polarization rotator and antireflector using meanderline chiral metamaterials: Analytical and numerical approach". In: *Optik* 126.24 (2015), pp. 5587–5592.

[84] Lingling Huang, Shuang Zhang, and Thomas Zentgraf. "Metasurface holography: From fundamentals to applications". In: *Nanophotonics* 7.6 (2018), pp. 1169–1190.

[85] Kseniia Baryshnikova, Dmitry Gets, Tatiana Liashenko, Anatoly Pushkarev, Ivan Mukhin, Yuri Kivshar, and Sergey Makarov. "Broadband Antireflection with Halide Perovskite Metasurfaces". In: *Laser and Photonics Reviews* 14 (2020).

[86] Stéphane Larouche, Yu Ju Tsai, Talmage Tyler, Nan M. Jokerst, and David R. Smith. "Infrared metamaterial phase holograms". In: *Nature Materials* 11 (5 2012), pp. 450–454. ISSN: 14764660.

[87] Geyang Qu, Wenhong Yang, Qinghai Song, Yilin Liu, Cheng Wei Qiu, Jiecai Han, Din Ping Tsai, and Shumin Xiao. "Reprogrammable metahologram for optical encryption". In: *Nature Communications* 11 (2020).

[88] Xuyue Guo, Peng Li, Jinzhan Zhong, Dandan Wen, Bingyan Wei, Sheng Liu, Shuxia Qi, and Jianlin Zhao. "Stokes meta-hologram toward optical cryptography". In: *Nature Communications* 13 (2022).

[89] H. P. Myers. *Introductory to Solid State Physics*. Second. Taylor and Francis, 1997.

[90] Stefan A. Maier. *Plasmonics: Fundamentals and Applications*. 1st. New York, NY: Springer Us, 2007. ISBN: 0387331506.

[91] Emilie Ringe, Mark R. Langille, Kwonnam Sohn, Jian Zhang, Jiaxing Huang, Chad A. Mirkin, Richard P. Van Duyne, and Laurence D. Marks. "Plasmon length: A universal parameter to describe size effects in gold nanoparticles". In: *Journal of Physical Chemistry Letters* 3 (2012), pp. 1479–1483.

[92] Xingjie Ni, Alexander V. Kildishev, and Vladimir M. Shalaev. "Metasurface holograms for visible light". In: *Nature Communications* 4 (Nov. 2013).

[93] Euclides Almeida, Ora Bitton, and Yehiam Prior. "Nonlinear metamaterials for holography". In: *Nature Communications* 7 (2016).

[94] Shulin Sun, Kuang-Yu Yang, Chih-Ming Wang, Ta-Ko Juan, Wei Ting Chen, Chun Yen Liao, Qiong He, Shiyi Xiao, Wen-Ting Kung, Guang-Yu Guo, Lei Zhou, and Din Ping Tsai. "High-Efficiency Broadband Anomalous Reflection by Gradient Meta-Surfaces". In: *Nano Letters* 12.12 (2012), pp. 6223–6229.

[95] Alastair D. Humphrey and William L. Barnes. "Plasmonic surface lattice resonances on arrays of different lattice symmetry". In: *Physical Review B - Condensed Matter and Materials Physics* 90 (2014).

[96] Lord Rayleigh. "III. Note on the remarkable case of diffraction spectra described by Prof. Wood". In: *The London, Edinburgh, and Dublin Philosophical Magazine and Journal of Science* 14.79 (1907), pp. 60–65.

[97] Weilu Gao, Jie Shu, Ciyuan Qiu, and Qianfan Xu. "Excitation of Plasmonic Waves in Graphene by Guided-Mode Resonances". In: *ACS Nano* 6.9 (2012), pp. 7806–7813.

[98] Eric S.A. Goerlitzer, Reza Mohammadi, Sergey Nechayev, Kirsten Volk, Marcel Rey, Peter Banzer, Matthias Karg, and Nicolas Vogel. "Chiral Surface Lattice Resonances". In: *Advanced Materials* 32 (2020).

[99] Dmitry Khlopin, Frédéric Laux, William P. Wardley, Jérôme Martin, Gregory A. Wurtz, Jérôme Plain, Nicolas Bonod, Anatoly V. Zayats, Wayne Dickson, and Davy Gérard. "Lattice modes and plasmonic linewidth engineering in gold and aluminum nanoparticle arrays". In: *Journal of the Optical Society of America B* 34 (2017), p. 691.

[100] R. Guo, T. K. Hakala, and P. Törmä. "Geometry dependence of surface lattice resonances in plasmonic nanoparticle arrays". In: *Physical Review B* 95 (2017).

[101] Theng Loo Lim, Yaswant Vaddi, M. Saad Bin-Alam, Lin Cheng, Rasoul Alaee, Jeremy Upham, Mikko J. Huttunen, Ksenia Dolgaleva, Orad Reshef, and Robert W. Boyd. "Fourier-Engineered Plasmonic Lattice Resonances". In: *ACS Nano* 16 (2022), pp. 5696–5703.

[102] Kirsten Volk, Joseph P.S. Fitzgerald, Pia Ruckdeschel, Markus Retsch, Tobias A.F. König, and Matthias Karg. "Reversible Tuning of Visible Wavelength Surface Lattice Resonances in Self-Assembled Hybrid Monolayers". In: *Advanced Optical Materials* 5 (2017).

[103] Vaibhav Gupta, Patrick T. Probst, Fabian R. Goßler, Anja Maria Steiner, Jonas Schubert, Yannic Brasse, Tobias A.F. König, and Andreas Fery. "Mechanotunable Surface Lattice Resonances in the Visible Optical Range by Soft Lithography Templates and Directed Self-Assembly". In: *ACS Applied Materials and Interfaces* 11 (2019), pp. 28189–28196.

[104] Jussi Kelavuori, Viatcheslav Vanyukov, Timo Stolt, Petri Karvinen, Heikki Rekola, Tommi K. Hakala, and Mikko J. Huttunen. "Thermal Control of Plasmonic Surface Lattice Resonances". In: *Nano Letters* 22 (10 2022), pp. 3879–3883.

[105] Peter Offermans, Martijn C. Schaafsma, Said R. K. Rodriguez, Yichen Zhang, Mercedes Crego-Calama, Sywert H. Brongersma, and Jaime Gómez Rivas. "Universal Scaling of the Figure of Merit of Plasmonic Sensors". In: *ACS Nano* 5.6 (2011), pp. 5151–5157.

[106] Michal Eitan, Zeev Iluz, Yuval Yifat, Amir Boag, Yael Hanein, and Jacob Scheuer. "Degeneracy Breaking of Wood's Anomaly for Enhanced Refractive Index Sensing". In: *ACS Photonics* 2.5 (2015), pp. 615–621.

[107] Jingtian Hu, Danqing Wang, Debanjan Bhowmik, Tingting Liu, Shikai Deng, Michael P. Knudson, Xianyu Ao, and Teri W. Odom. "Lattice-Resonance Metalenses for Fully Reconfigurable Imaging". In: *ACS Nano* 13 (2019), pp. 4613–4620.

[108] Guangyuan Li, Xiang Du, Lei Xiong, and Xiuhua Yang. "Plasmonic Metasurfaces with Quality Factors Up to 790 in the Visible Regime". In: *Advanced Optical Materials* (2023).

[109] M. Saad Bin-Alam, Orad Reshef, Yaryna Mamchur, M. Zahirul Alam, Graham Carlow, Jeremy Upham, Brian T. Sullivan, Jean-Michel Ménard, Mikko J. Huttunen, Robert W. Boyd, and Ksenia Dolgaleva. "Ultra-high-Q resonances in plasmonic metasurfaces". In: *Nature Communications* 12 (2021), p. 974.

[110] Sergei V. Zhukovsky, Viktoriia E. Babicheva, Alexander V. Uskov, Igor E. Protsenko, and Andrei V. Lavrinenko. "Enhanced electron photoemission by collective lattice resonances in plasmonic nanoparticle-array photodetectors and solar cells". In: *Plasmonics* 9 (2014), pp. 283–289.

[111] T. K. Hakala, H. T. Rekola, A. I. Väkeväinen, J. P. Martikainen, M. Nečada, A. J. Moilanen, and P. Törmä. "Lasing in dark and bright modes of a finite-sized plasmonic lattice". In: *Nature Communications* 8 (2017).

[112] V.A. Markel. "Coupled-dipole Approach to Scattering of Light from a One-dimensional Periodic Dipole Structure". In: *Journal of Modern Optics* 40.11 (1993), pp. 2281–2291.

[113] Shengli Zou, Nicolas Janel, and George C. Schatz. "Silver nanoparticle array structures that produce remarkably narrow plasmon lineshapes". In: *Journal of Chemical Physics* 120.23 (2004), pp. 10871–10875.

[114] Mikko J. Huttunen, Ksenia Dolgaleva, Päivi Törmä, and Robert W. Boyd. "Ultra-strong polarization dependence of surface lattice resonances with out-of-plane plasmon oscillations". In: *Optics Express* 24.25 (2016), pp. 28279–28289.

[115] Tobias W. W. Maß and Thomas Taubner. "Incident Angle-Tuning of Infrared Antenna Array Resonances for Molecular Sensing". In: *ACS Photonics* 2.10 (2015), pp. 1498–1504.

[116] Mikko J. Huttunen, Orad Reshef, Timo Stolt, Ksenia Dolgaleva, Robert W. Boyd, and Martti Kauranen. "Efficient nonlinear metasurfaces by using multiresonant high-Q plasmonic arrays". In: *Journal of the Optical Society of America B* 36.7 (2019), E30.

[117] Kevin O'Brien, Haim Suchowski, Junsuk Rho, Alessandro Salandrino, Boubacar Kante, Xiaobo Yin, and Xiang Zhang. "Predicting nonlinear properties of metamaterials from the linear response". In: *Nature Materials* 14.4 (2015), pp. 379–383.

[118] David C. Hooper, Christian Kuppe, Danqing Wang, Weijia Wang, Jun Guan, Teri W. Odom, and Ventsislav K. Valev. "Second Harmonic Spectroscopy of Surface Lattice Resonances". In: *Nano Letters* 19.1 (2019), pp. 165–172.

[119] Tingyin Ning, Henna Pietarinen, Outi Hyvärinen, Ravi Kumar, Tommi Kaplas, Martti Kauranen, and Goëry Genty. "Efficient second-harmonic generation in silicon nitride resonant waveguide gratings". In: *Optics Letters* 37.20 (2012), pp. 4269–4271.

[120] Michele Celebrano, Xiaofei Wu, Milena Baselli, Swen Großmann, Paolo Biagioni, Andrea Locatelli, Costantino De Angelis, Giulio Cerullo, Roberto Osellame, Bert Hecht, Lamberto Duò, Franco Ciccacci, and Marco Finazzi. "Mode matching in multiresonant plasmonic nanoantennas for enhanced second harmonic generation". In: *Nature Nanotechnology* 10.5 (2014), pp. 412–417.

[121] Momchil Minkov, Dario Gerace, and Shanhui Fan. "Doubly resonant $\chi^{(2)}$ nonlinear photonic crystal cavity based on a bound state in the continuum". In: *Optica* 6 (2019), p. 1039.

[122] Jun Wang, Marco Clementi, Momchil Minkov, Andrea Barone, Jean-François Carlin, Nicolas Grandjean, Dario Gerace, Shanhui Fan, Matteo Galli, and Romuald Houdré. "Doubly resonant second-harmonic generation of a vortex beam from a bound state in the continuum". In: *Optica* 7 (2020), p. 1126.

[123] Jerry I. Dadap, Jie Shan, and Tony F. Heinz. "Theory of optical second-harmonic generation from a sphere of centrosymmetric material: small-particle limit". In: *J. Opt. Soc. Am. B* 21.7 (2004), pp. 1328–1347.

[124] N C Panoiu, W E I Sha, D Y Lei, and G-C Li. "Nonlinear optics in plasmonic nanostructures". In: *Journal of Optics* 20.8 (June 2018), p. 083001.

[125] Brian K. Canfield, Sami Kujala, Konstantins Jefimovs, Jari Turunen, and Martti Kauranen. "Linear and nonlinear optical responses influenced by broken symmetry in an array of gold nanoparticles". In: *Optics Express* 12.22 (2004), pp. 5418–5423.

[126] M. Saad Bin-Alam, Joshua Baxter, Kashif M. Awan, Antti Kiviniemi, Yaryna Mamchur, Antonio Calà Lesina, Kosmas L. Tsakmakidis, Mikko J. Huttunen, Lora Ramunno, and Ksenia Dolgaleva. "Hyperpolarizability of Plasmonic Meta-Atoms in Metasurfaces". In: *Nano Letters* 21 (2021), pp. 51–59.

[127] Cristian Cirac'i, Ekaterina Poutrina, Michael Scalora, and David R. Smith. "Origin of second-harmonic generation enhancement in optical split-ring resonators". In: *Phys. Rev. B* 85 (20 May 2012), p. 201403.

[128] Hannu Husu, Roope Siikanen, Jouni Mäkitalo, Joonas Lehtolahti, Janne Laukkanen, Markku Kuittinen, and Martti Kauranen. "Metamaterials with Tailored Nonlinear Optical Response". In: *Nano Letters* 12.2 (2012), pp. 673–677.

[129] Godofredo Bautista, Mikko J. Huttunen, Jouni Mäkitalo, Juha M. Kontio, Janne Simonen, and Martti Kauranen. "Second-Harmonic Generation Imaging of Metal Nano-Objects with Cylindrical Vector Beams". In: *Nano Letters* 12.6 (2012), pp. 3207–3212.

[130] Jérémy Butet, Krishnan Thyagarajan, and Olivier J. F. Martin. "Ultrasensitive Optical Shape Characterization of Gold Nanoantennas Using Second Harmonic Generation". In: *Nano Letters* 13.4 (2013), pp. 1787–1792.

[131] Jérémy Butet, Benjamin Gallinet, Krishnan Thyagarajan, and Olivier J. F. Martin. "Second-harmonic generation from periodic arrays of arbitrary shape plasmonic nanostructures: a surface integral approach". In: *J. Opt. Soc. Am. B* 30.11 (2013), pp. 2970–2979.

[132] Dennis M. Sullivan. *Electromagnetic Simulation Using the FDTD Method*. Vol. 5. John Wiley & Sons, 2000. ISBN: 9781118459393.

[133] Daryl L. Logan. *A First Course in the Finite Element Method: Enhanced Edition*. Vol. 6. Cengage Learning, 2022. ISBN: 9780357676424.

[134] Hao Yang. *FDTD modeling of metamaterials : theory and applications*. eng. Boston [i.e. Norwood], Massachusetts: Artech House, 2008. ISBN: 1-59693-161-2.

[135] Yu Wenhua. *Advanced computational electromagnetic methods and applications*. eng. Artech House antennas and electromagnetics analysis library Advanced computational electromagnetic methods and applications. Boston ; Artech House, 2015. ISBN: 1-5231-1693-5.

[136] Siu-Wing. Cheng, Tamal K. (Tamal Krishna) Dey, and Jonathan. Shewchuk. *Delaunay mesh generation*. eng. Boca Raton: CRC Press, 2013. ISBN: 0-429-18609-6.

[137] Antti Kiviniemi. *Spectral Measurements of Second-Harmonic Generated Light*. M.Sc Thesis. Tampere University of Technology, 2018.

[138] Orazio Svelto. *Principles of lasers*. 5. New York, NY: Springer, 2010. ISBN: 9781441913012.

[139] Warren N. Herman and L. Michael Hayden. "Maker fringes revisited: second-harmonic generation from birefringent or absorbing materials". In: *J. Opt. Soc. Am. B* 12.3 (1995), p. 416.

[140] L. Alloatti, C. Kieninger, A. Froelich, M. Lauermann, T. Frenzel, K. Köhnle, W. Freude, J. Leuthold, M. Wegener, and C. Koos. "Second-order nonlinear optical metamaterials: ABC-type nanolaminates". In: *Applied Physics Letters* 107 (2015).

[141] Sebastian Beer, Jeetendra Gour, Alessandro Alberucci, Christin David, Stefan Nolte, and Uwe D. Zeitner. "Second harmonic generation under doubly resonant lattice plasmon excitation". In: *Opt. Express* 30.22 (2022), pp. 40884–40896.

[142] Shanhui Fan, Wonjoo Suh, and J. D. Joannopoulos. "Temporal coupled-mode theory for the Fano resonance in optical resonators". In: *J. Opt. Soc. Am. A* 20.3 (2003), pp. 569–572.

[143] Dan Oron, Eran Tal, and Yaron Silberberg. "Scanningless depth-resolved microscopy". In: *Opt. Express* 13.5 (2005), pp. 1468–1476.

[144] Shawn Divitt, Wenqi Zhu, Cheng Zhang, Henri J. Lezec, and Amit Agrawal. "Ultrafast optical pulse shaping using dielectric metasurfaces". In: *Science* 364.6443 (2019), pp. 890–894.

[145] René Geromel, Philip Georgi, Maximilian Protte, Shiwei Lei, Tim Bartley, Lingling Huang, and Thomas Zentgraf. "Compact Metasurface-Based Optical Pulse-Shaping Device". In: *Nano Letters* 23.8 (2023), pp. 3196–3201.

[146] Madona Mekhael, Timo Stolt, Anna Vesala, Heikki Rekola, Tommi K. Hakala, Robert Fickler, and Mikko J. Huttunen. "Phase-Matched Second-Harmonic Generation from Metasurfaces Inside Multipass Cells". In: *ACS Photonics* 11.2 (2024), pp. 682–687.

[147] Mikko J. Huttunen, Payman Rasekh, Robert W. Boyd, and Ksenia Dolgaleva. "Using surface lattice resonances to engineer nonlinear optical

processes in metal nanoparticle arrays". In: *Physical Review A* 97.5 (May 2018).

[148] Nadav Segal, Shay Keren-Zur, Netta Hendler, and Tal Ellenbogen. "Controlling light with metamaterial-based nonlinear photonic crystals". In: *Nature Photonics* 9 (Feb. 2015), pp. 180–184.

[149] Shay Keren-Zur, Ori Avayu, Lior Michaeli, and Tal Ellenbogen. "Nonlinear Beam Shaping with Plasmonic Metasurfaces". In: *ACS Photonics* 3.1 (2016), pp. 117–123. ISSN: 23304022.

[150] Bingxia Wang, Kai Wang, Xuanmiao Hong, Yan Sheng, Shuhang Qian, and Peixiang Lu. "Resonant Nonlinear Synthetic Metasurface with Combined Phase and Amplitude Modulations". In: *Laser and Photonics Reviews* 15 (2021).

[151] Luyao Xu, Christopher A. Curwen, Philip W.C. Hon, Qi Sheng Chen, Tatsuo Itoh, and Benjamin S. Williams. "Metasurface external cavity laser". In: *Applied Physics Letters* 107 (Nov. 2015).

[152] Yi Yang Xie, Pei Nan Ni, Qiu Hua Wang, Qiang Kan, Gauthier Briere, Pei Pei Chen, Zhuang Zhuang Zhao, Alexandre Delga, Hao Ran Ren, Hong Da Chen, Chen Xu, and Patrice Genevet. "Metasurface-integrated vertical cavity surface-emitting lasers for programmable directional lasing emissions". In: *Nature Nanotechnology* 15 (2020), pp. 125–130.

[153] Tsafrir Abir, Mai Tal, and Tal Ellenbogen. "Second-Harmonic Enhancement from a Nonlinear Plasmonic Metasurface Coupled to an Optical Waveguide". In: *Nano Letters* 22 (Apr. 2022), pp. 2712–2717.

[154] Alexander S. Solntsev, Girish S. Agarwal, and Yuri Yuri Kivshar. "Metasurfaces for quantum photonics". In: *Nature Photonics* 15 (2021), pp. 327–336.

[155] Daniel Frese, Qunshuo Wei, Yongtian Wang, Mirko Cinchetti, Lingling Huang, and Thomas Zentgraf. "Nonlinear Bicolor Holography Using Plasmonic Metasurfaces". In: *ACS Photonics* 8 (2021), pp. 1013–1019.

[156] Mukesh Sharma, Lior Michaeli, Danielle Ben Haim, and Tal Ellenbogen. "Liquid Crystal Switchable Surface Lattice Resonances in Plasmonic Metasurfaces". In: *ACS Photonics* 9 (2022), pp. 2702–2712.

PUBLICATIONS

PUBLICATION
I

Backward Phase-Matched Second-Harmonic Generation from Stacked Metasurfaces

Timo Stolt, Jeonghyun Kim, Sébastien Héron, Anna Vesala, Younghwan Yang, Jungho Mun, Minkyung Kim, Mikko J. Huttunen, Robert Czaplicki, Martti Kauranen, Junsuk Rho, and Patrice Genevet

Physical Review Letters 126 (2021), p. 033901
DOI: 10.1103/PhysRevLett.126.033901

Backward Phase-Matched Second-Harmonic Generation from Stacked Metasurfaces

Timo Stolt,[1,*] Jeonghyun Kim,[2,*] Sébastien Héron,[3] Anna Vesala,[1] Younghwan Yang,[2] Jungho Mun,[5] Minkyung Kim,[2] Mikko. J. Huttunen,[1] Robert Czaplicki,[4] Martti Kauranen,[1] Junsuk Rho,[2,5,6,‡] and Patrice Genevet[3,†]

[1]*Photonics Laboratory, Physics Unit, Tampere University, FI-33014 Tampere, Finland*
[2]*Department of Mechanical Engineering, Pohang University of Science and Technology (POSTECH), Pohang 37673, Republic of Korea*
[3]*Université Côte d'Azur, CNRS, CRHEA, rue Bernard Gregory, Sophia Antipolis, 06560 Valbonne, France*
[4]*Institute of Physics, Faculty of Physics, Astronomy, and Informatics, Nicolaus Copernicus University, Grudziądzka 5/7, 87-100 Toruń, Poland*
[5]*Department of Chemical Engineering, Pohang University of Science and Technology (POSTECH), Pohang 37673, Republic of Korea*
[6]*National Institute of Nanomaterials Technology (NINT), Pohang 37673, Republic of Korea*

(Received 16 June 2020; accepted 16 December 2020; published 22 January 2021)

We demonstrate phase-matched second-harmonic generation (SHG) from three-dimensional metamaterials consisting of stacked metasurfaces. To achieve phase matching, we utilize a novel mechanism based on phase engineering of the metasurfaces at the interacting wavelengths, facilitating phase-matched SHG in the unconventional backward direction. Stacking up to five metasurfaces,we obtain a phase-matched SHG signal, which scales superlinearly with the number of layers. Our results motivate further investigations to achieve higher conversion efficiencies also with more complex wave fronts.

DOI: 10.1103/PhysRevLett.126.033901

Optical metamaterials and metasurfaces are artificial structures consisting of subwavelength building blocks, known as meta-atoms, and are associated with optical properties not found in nature [1]. These properties include magnetism at optical frequencies, strong optical activity, negative index of refraction, and epsilon-near-zero behavior [2–4]. In addition, recent work on phase-engineered metasurfaces has demonstrated the interesting possibilities to realize flat optical components, such as lenses, holographic components, and polarizers [5–11].

In addition to the linear optical properties of metamaterials, their nonlinear optical responses are also becoming important. Several technologically relevant photonic applications rely on the nonlinear responses of materials, including second-harmonic generation (SHG), photon-pair generation, all-optical switching, frequency combs, and supercontinuum generation [12–15]. The challenging part in these nonlinear applications is the fact that nonlinear optical processes in materials are intrinsically weak. Because of this fact, nonlinear processes in conventional materials, such as crystals, rely on the concept of phase matching. In phase-matched materials and without losses, the generated nonlinear signal scales quadratically on the propagation length, resulting in practical conversion efficiencies with sufficiently long materials [see Fig. 1(a)] [16,17].

For homogeneous materials and forward SHG signals, phase matching can be achieved if the refractive indices at the fundamental and second-harmonic frequencies are equal. However, this requirement is a significant limitation because of refractive-index dispersion, which can be overcome by the concept of quasi-phase-matching, i.e., by structuring the material in such a way that the sign of the nonlinear susceptibility is periodically reversed [18]. In principle, quasi-phase-matching is a very general concept that allows any nonlinear signal to be optimized. Unfortunately, quasi-phase-matching and other traditional phase-matching schemes seem unfeasible for miniaturization of optical devices. Additionally, these techniques are restricted in terms of, e.g., polarization and the spatial

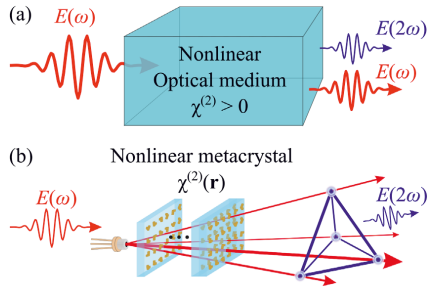

FIG. 1. (a) For traditional nonlinear materials, achieving phase matching and strong nonlinear responses is very restricted in terms of, e.g., the selected material and the polarization of the interacting fields. (b) Nonlinear optical processes can be phase matched with metamaterials that induce arbitrary phase changes in the interacting fields.

profiles of the interacting waves. These limitations motivate the ongoing development of efficient and less restricted nanoscale devices.

Utilization of metal nanoantennas has recently emerged as a promising route toward more efficient nonlinear metamaterials [19,20]. Metal nanoantennas support collective oscillations of conduction electrons, known as localized surface plasmons. Under resonant conditions, these oscillations give rise to localized surface plasmon resonances (LSPRs), which can considerably enhance the local field near the particles [21]. Because nonlinear processes scale with high powers of the local field, the plasmon-assisted field enhancement can result in a dramatic increase in the otherwise weak nonlinear response. Consequently, numerous investigations have been carried out during the past decade in order to understand the nonlinear response of plasmonic nanoantennas [22–26]. So far, work on nonlinear metamaterials has focused on single planar metasurfaces limiting the achieved efficiencies. A viable route to improve the efficiencies, which was explored numerically before [27], would be to stack several metasurfaces on top of each other, giving rise to phase-matching issues. In addition, such nonlinear metamaterials could provide novel capabilities to conventional phase-matching techniques relying on the intrinsic material dispersion. Particularly, the use of metamaterials could allow one to design phase-matched devices exhibiting arbitrary transverse phase profiles, therefore providing interesting possibilities to fabricate nonlinear metalenses and holography [see Fig. 1(b)] [28,29].

We demonstrate how such nonlinear phase-matched metamaterials can be fabricated by stacking metasurfaces into three-dimensional (3D) structures and show how the approach can considerably improve the performance of existing nonlinear metasurfaces. Our approach utilizes both local-field enhancement and phase engineering of LSPRs. The latter provides more freedom to phase match nonlinear processes than what is possible using conventional nonlinear materials [see Fig. 1(b)]. We demonstrate both capabilities by fabricating metamaterial devices consisting of up to five layers of metasurfaces that are phase matched to emit SHG in the backward direction. We demonstrate *superlinear* dependence of the emitted SHG signals on the number of stacked metasurfaces, which is only possible via phase matching.

For conventional materials and SHG, the phase changes are associated with the propagation of the fundamental and second-harmonic fields through the material. Phase matching in such materials is connected to wave vector mismatch Δk, which vanishes for perfectly phase-matched processes. With Δk, we can define the phase-matching condition, e.g., for backpropagating SHG as $\Delta k = 2k_\omega + k_{2\omega} = 0$, where $k_\omega = n_\omega \omega/c$ and $k_{2\omega} = n_{2\omega} 2\omega/c$ are the wave vector amplitudes at the fundamental (ω) and SHG (2ω) frequencies, respectively [16]. With conventional nonlinear materials, this condition cannot be fulfilled, but it can be compensated by fabricating periodic quasi-phase-matched crystals [16,30,31]. It is also possible to utilize zero-index materials to realize structures that have relaxed phase-matching requirements [32].

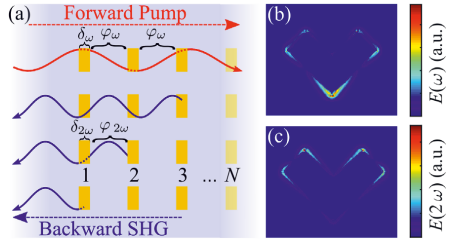

FIG. 2. (a) Backward phase-matched SHG emission from metamaterials consisting of N stacked layers. The phase-matching condition is fulfilled by controlling the phase accumulation for both incident light (red arrows) and SHG light (blue arrows). The terms φ_ω and $\varphi_{2\omega}$ correspond to phase accumulation due to propagation. The LSPRs of metal nanoantennas enhance the local fields at (b) fundamental frequency E_ω and (c) second-harmonic (SH) frequency $E_{2\omega}$ and also induce the phase changes associated with LSPRs δ_ω and $\delta_{2\omega}$, respectively.

By using resonant metamaterials, we can extend this phase-matching condition by taking into account the phase changes δ_ω and $\delta_{2\omega}$ that occur in a metamaterial due to coherent scattering of light from the constituent nanoantennas at the fundamental and SHG frequencies, respectively. Because these terms are dictated by the optical response of the nanoantennas, namely, by their LSPRs [7], the extended phase-matching condition becomes solvable by metamaterial design. In order to demonstrate this capability, we designed and fabricated metamaterial devices where the backward SHG emission is phase matched [see Fig. 2(a)].

The designed metamaterial devices consisted of a number N of identical metasurfaces that were separated by identical spacer layers of thickness h. For such devices, the total amplitude of the emitted SH field is described by (see the Supplemental Material [33] for details)

$$\mathrm{SHG} \propto \left| \sum_{J=1}^{N} T(\omega)^J T(2\omega)^{J/2} e^{iJ\Delta k} \chi^{(2)}_{\mathrm{ms}} E(\omega)^2 \right|^2, \quad (1)$$

where $\chi^{(2)}_{\mathrm{ms}}$ is the relevant component of the SHG susceptibility tensor of a single metasurface, and $T(\omega)$ and $T(2\omega)$ are the transmittances of a single metasurface at the fundamental and SH frequencies, respectively. For phase-matched SH emission, the wave vector mismatch Δk must therefore be an integer of 2π,

$$\Delta k = 2(\varphi_\omega + \delta_\omega) + \varphi_{2\omega} + \delta_{2\omega} = 2\pi m, \quad (2)$$

where m is an integer and terms $\varphi_{2\omega} = k_{2\omega} h$ and $\varphi_\omega = k_\omega h$ arise from the propagation of the fields. Estimating the

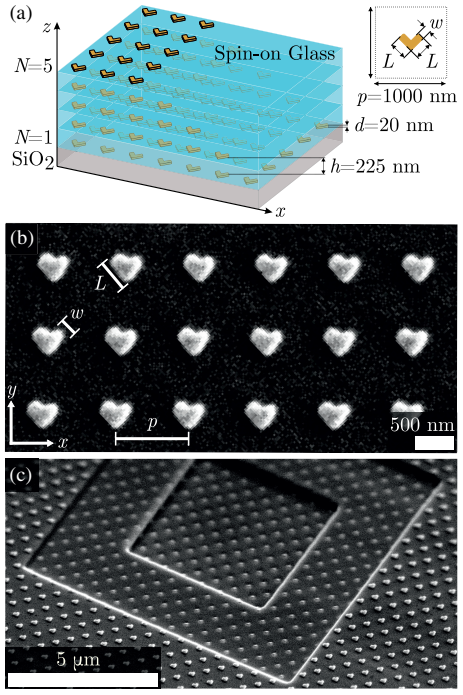

FIG. 3. (a) Investigated devices were composed of up to N metasurfaces stacked on top of each other, separated by $h = 225$-nm-thick spacer layers. Each of the metasurfaces consisted of a square array of 20-nm-thick V-shaped gold nanoantennas. (b) Representative scanning electron micrograph of one fabricated device ($L190$-3). (c) Oblique scanning electron micrograph obtained after successive etching with a focused ion beam, illustrating the stacked nature of the investigated metamaterial devices.

phase terms δ_ω and $\delta_{2\omega}$, which correspond to nanoparticles scattering phase retardation at ω and 2ω for the particles of interest, Eq. (2) allows us to solve for the spacer thickness h. The transmittance, phase, and susceptibility terms of Eqs. (1) and (2) were estimated from the measured transmission spectra of our devices (see the Supplemental Material [33] for details).

Our metamaterials consisted of a varying number N metasurfaces composed of V-shaped gold nanoantennas with arm lengths of $L = 190$ nm ($L190$-N), arm widths of $w = 100$ nm, and thicknesses of $d = 20$ nm. These nanostructures were arranged into square lattices with a lattice constant of $p = 1000$ nm [Fig. 3(a)]. This lattice configuration was chosen because it has been earlier found to emit SHG strongly [34]. However, we note that the configuration is not yet optimized in terms of overall conversion efficiency, because the strongest SHG emission from such arrays may not occur in the normal direction [35]. Note also that, due to the configuration, other nonlinear diffractive channels exist, but they do not fulfill the phase-matching condition. Interesting new possibilities to realize multibeam phase-matching processes can be envisioned in the context of multiplexed nonlinear metasurface stacks.

The above parameters were calculated to give rise to LSPRs centered near 1060 nm. According to Eq. (2), for $m = 0$ the phase-matching condition was fulfilled close to the LSPR wavelength by choosing the layer thickness of $h = 225$ nm. Specifically, the phase-matching condition for devices $L190$-N was fulfilled for linear input polarization orthogonal to the symmetry axis of the V particles (x axis) [Fig. 3(b)]. Because of the symmetry properties of the samples, the generated SHG emission is polarized along the symmetry axis (y axis).

The devices were fabricated using standard electron beam lithography on a cleaned SiO_2 substrate through a sequence of steps repeated N times (see the Supplemental Material [33] for further details) [36]. Representative scanning electron micrographs of one realized metamaterial device ($L190$-3) are shown in Figs. 3(b) and 3(c).

The SHG responses of the devices were characterized using a setup described in detail elsewhere [34]. Briefly, a femtosecond laser oscillator (Chameleon Vision II, Ti: sapphire, 80 MHz) combined with an optical parametric oscillator (Chameleon Compact, 1000–1300 nm) was used as the pump, while the backward-emitted SHG signals were measured using a power-calibrated photomultiplier tube. See Supplemental Material [33] for a more detailed description of the setup. Here, we limited our input mean power to 10 mW in order to avoid possible sample damage. The SHG responses of the fabricated metamaterial devices consisting of varying number of metasurfaces ($N = 1, 2, \ldots, 5$) were measured as a function of the pump wavelength (see Fig. 4).

The predicted SH emission spectra from the devices [Fig. 4(a)] show a clear increase of the average SHG power near the phase-matching wavelength of 1135 nm when the number of metasurfaces N grows. This behavior is also observed in the measured backward-emitted SHG signals [Fig. 4(b)]. The strongest SHG signal for the device composed of five metasurfaces ($L190$-5) corresponded to SHG power of 20 fW and occurred at the wavelength of 1141 nm, which is slightly shifted from the predicted phase-matching wavelength due to experimental imperfections. A closer analysis of the results reveals that the SHG response near 1141 nm no longer depends linearly on the number of metasurfaces N [Fig. 4(b)]. Instead, the SHG signals follow superlinear dependence on N ($\mathrm{SHG} \propto N^{1.27}$), confirming that the devices were successfully phase matched [Fig. 4(c)]. Furthermore, the devices were successfully phase matched in the challenging backward direction [37]. Because the SHG emission from the device $L190$-1 was markedly weaker than the SHG emissions

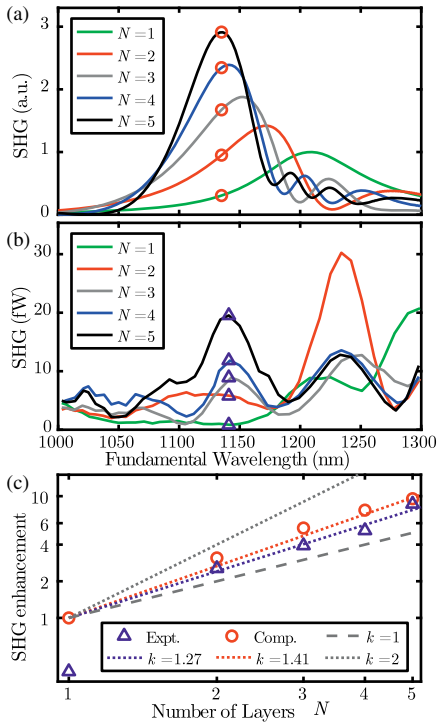

FIG. 4. (a) Predicted and (b) measured SHG emission spectra from the devices. SHG emission grows with increasing number of layers N at the phase-matching wavelength of 1135 nm (1141 nm) for predicted (measured) results. (c) Both the predicted (red spheres) and experimental (blue triangles) SHG emissions scale superlinearly as a function of N, resulting in linear fits with slopes $k > 1$ on the logarithmic scale.

from the rest of devices, that data point was excluded from the curve fitting. This difference between the $L190$-1 and other devices may be a result of interlayer coupling that is not present in the single layer device.

We note that the fabricated devices exhibited losses that were estimated by measuring the transmittance of a single metasurface to be close to 90% (97%) near the pump (SHG) wavelengths (see the measured transmittance spectra in the Supplemental Material [33]). By taking into account the associated reductions in the intensities for subsequent metasurfaces [see Eq. (1)], one expects around eightfold SHG enhancement, which is very close to the enhancement we measure [Fig. 4(c)].

Next we discuss approaches that could be combined with the demonstrated methodology in order to further improve the performance of nonlinear metamaterials. First, an obvious method would be to increase the number of metasurface stacks N. However, at some point of increasing N to values much higher than 5, the surface flatness of the fabricated metasurfaces may start to be affected. As discussed previously [38–40], the spin-on-glass planarization introduces surface roughness of the order of only a few nanometers for five adjacent layers. According to Ref. [41], some effort would be required to address this problem for thicker artificial nonlinear crystals (~20–50 layers and beyond). Second, the nanoparticle material, shapes, and dimensions used in this Letter have not yet been optimized in terms of overall conversion efficiencies. Recent advances in all-dielectric nonlinear metasurfaces also suggest that record-high conversion efficiencies could be achieved by phase matching such structures using this methodology [42]. Third, looking at Eq. (1) and Fig. 4(c), we see that, in order to considerably improve the efficiency of future phase-matched metamaterial devices by further increasing N, the metasurfaces should be made highly transparent at the operation wavelengths. Finally, we note that the conversion efficiency is not the only figure of merit. In many applications, a more important parameter is the optical power of the generated light. Here, nonlinear metasurfaces are a promising technology, because their fabrication can be scaled up to array sizes that are compatible with the use of high-power lasers, for example, by using nanoimprint lithography [43].

In addition to enhancing the overall conversion efficiencies of nonlinear metamaterials, this demonstration of phase-engineered nonlinear metamaterials has several other fundamental implications. For example, one can envisage how nonlinear metamaterials could be utilized for adiabatic frequency conversion, enabling broadband frequency conversion in nanomaterials [44,45]. Furthermore, this methodology could allow design of more efficient nonlinear terahertz-emitting metamaterials [46–48]. Finally, the presented phase-engineering principles apply also for arbitrary wave fronts. Successful phase matching of nonlinear processes using complex spatial modes would have applications in holography and quantum computing [24,28].

To conclude, we have demonstrated how the performance of nonlinear metamaterials can be substantially increased by stacking metasurfaces into three-dimensional metamaterials. Phase-matching considerations that are often difficult to fulfill using conventional materials can be easily solved by controlling the dimensions of the nanoantennas and the separation between the metasurfaces. We demonstrated this by phase matching second-harmonic generation emission from fabricated metamaterials in the challenging backward direction. We fabricated nonlinear metamaterial devices consisting of up to five stacked metasurfaces and demonstrated an order-of-magnitude increase in the backward-emitted second-harmonic intensities from the devices. Our results open a new paradigm of phase-engineered three-dimensional nonlinear metamaterials that could be used, for example, to realize more efficient nonlinear metamaterials.

We acknowledge the support of the Academy of Finland (Grant No. 308596), the Flagship of Photonics Research and Innovation (PREIN) funded by the Academy of Finland (Grant No. 320165), the European Research Council (ERC) under the European Union's Horizon 2020 Research and Innovation Programme (Grant Agreements No. 639109 and No. 724881), the National Research Foundation (NRF) Grants (No. NRF-2019R1A2C3003129, No. CAMM-2019M3A6B3030637, No. NRF-2019R1A5A8080290, and No. NRF-2020K1A3A1A21024374) funded by the Ministry of Science and ICT of the Korean Government. Younghwan Yang acknowledges a fellowship from Hyundai Motor Chung Mong-Koo Foundation, and Minkyung Kim acknowledges the NRF Global Ph.D. fellowship (NRF-2017H1A2A1043204) funded by the Ministry of Education of the Korean government.

*These authors contributed equally to this work.
†Corresponding author.
patrice.genevet@crhea.cnrs.fr
‡Corresponding author.
jsrho@postech.ac.kr

[1] C. M. Soukoulis and M. Wegener, Nat. Photonics **5**, 523 (2011).
[2] M. W. Klein, C. Enkrich, M. Wegener, and S. Linden, Science **313**, 502 (2006).
[3] A. Alù, M. G. Silveirinha, A. Salandrino, and N. Engheta, Phys. Rev. B **75**, 155410 (2007).
[4] S. Zhang, Y.-S. Park, J. Li, X. Lu, W. Zhang, and X. Zhang, Phys. Rev. Lett. **102**, 023901 (2009).
[5] N. Yu and F. Capasso, Nat. Mater. **13**, 139 (2014).
[6] X. Yin, T. Steinle, L. Huang, T. Taubner, M. Wuttig, T. Zentgraf, and H. Giessen, Light **6**, e17016 (2017).
[7] P. Genevet, F. Capasso, F. Aieta, M. Khorasaninejad, and R. Devlin, Optica **4**, 139 (2017).
[8] L. Huang, S. Zhang, and T. Zentgraf, Nanophotonics **7**, 1169 (2018).
[9] E. Arbabi, S. M. Kamali, A. Arbabi, and A. Faraon, ACS Photonics **5**, 3132 (2018).
[10] H. Ren, G. Briere, X. Fang, P. Ni, R. Sawant, S. Héron, S. Chenot, S. Vézian, B. Damilano, V. Brändli, S. A. Maier, and P. Genevet, Nat. Commun. **10**, 2986 (2019).
[11] N. A. Rubin, G. D'Aversa, P. Chevalier, Z. Shi, W. T. Chen, and F. Capasso, Science **365**, eaax1839 (2019).
[12] P. G. Kwiat, K. Mattle, H. Weinfurter, A. Zeilinger, A. V. Sergienko, and Y. Shih, Phys. Rev. Lett. **75**, 4337 (1995).
[13] T. Brabec and F. Krausz, Rev. Mod. Phys. **72**, 545 (2000).
[14] T. J. Kippenberg, R. Holzwarth, and S. A. Diddams, Science **332**, 555 (2011).
[15] M. R. Shcherbakov, P. P. Vabishchevich, A. S. Shorokhov, K. E. Chong, D. Y. Choi, I. Staude, A. E. Miroshnichenko, D. N. Neshev, A. A. Fedyanin, and Y. S. Kivshar, Nano Lett. **15**, 6985 (2015).
[16] R. W. Boyd, *Nonlinear Optics* (Academic Press, San Diego, 2020).
[17] C. Wang, Z. Li, M. H. Kim, X. Xiong, X. F. Ren, G. C. Guo, N. Yu, and M. Lončar, Nat. Commun. **8**, 2098 (2017).
[18] E. J. Lim, M. M. Fejer, and R. L. Byer, Electron. Lett. **25**, 174 (1989).
[19] M. Kauranen and A. V. Zayats, Nat. Photonics **6**, 737 (2012).
[20] J. Lee, M. Tymchenko, C. Argyropoulos, P. Y. Chen, F. Lu, F. Demmerle, G. Boehm, M. C. Amann, A. Alù, and M. A. Belkin, Nature (London) **511**, 65 (2014).
[21] S. A. Maier, *Plasmonics: Fundamentals and Applications* (Springer Science & Business Media, New York, 2007).
[22] M. Lapine, I. V. Shadrivov, and Y. S. Kivshar, Rev. Mod. Phys. **86**, 1093 (2014).
[23] J. Butet, P. F. Brevet, and O. J. Martin, ACS Nano **9**, 10545 (2015).
[24] G. Li, S. Zhang, and T. Zentgraf, Nat. Rev. Mater. **2**, 17010 (2017).
[25] E. Rahimi and R. Gordon, Adv. Opt. Mater. **6**, 1800274 (2018).
[26] M. J. Huttunen, R. Czaplicki, and M. Kauranen, J. Nonlinear Opt. Phys. Mater. **28**, 1950001 (2019).
[27] N. Segal, S. Keren-Zur, N. Hendler, and T. Ellenbogen, Nat. Photonics **9**, 180 (2015).
[28] G. Li, S. Chen, N. Pholchai, B. Reineke, P. W. H. Wong, E. Y. B. Pun, K. W. Cheah, T. Zentgraf, and S. Zhang, Nat. Mater. **14**, 607 (2015).
[29] C. Schlickriede, N. Waterman, B. Reineke, P. Georgi, G. Li, S. Zhang, and T. Zentgraf, Adv. Mater. **30**, 1703843 (2018).
[30] M. Pelton, P. Marsden, D. Ljunggren, M. Tengner, A. Karlsson, A. Fragemann, C. Canalias, and F. Laurell, Opt. Express **12**, 3573 (2004).
[31] X. P. Hu, P. Xu, and S. N. Zhu, Photonics Res. **1**, 171 (2013).
[32] H. Suchowski, K. O'Brien, Z. J. Wong, A. Salandrino, X. Yin, and X. Zhang, Science **342**, 1223 (2013).
[33] See Supplemental Material at http://link.aps.org/supplemental/10.1103/PhysRevLett.126.033901 for descriptions of the semi-analytical phase-matching model, the sample fabrication process, the transmission experiments, and the experimental setup.
[34] R. Czaplicki, A. Kiviniemi, M. J. Huttunen, X. Zang, T. Stolt, I. Vartiainen, J. Butet, M. Kuittinen, O. J. F. Martin, and M. Kauranen, Nano Lett. **18**, 7709 (2018).
[35] R. Czaplicki, A. Kiviniemi, J. Laukkanen, J. Lehtolahti, M. Kuittinen, and M. Kauranen, Opt. Lett. **41**, 2684 (2016).
[36] G. Yoon, I. Kim, S. So, J. Mun, M. Kim, and J. Rho, Sci. Rep. **7**, 6668 (2017).
[37] L. Liu, L. Wu, J. Zhang, Z. Li, B. Zhang, and Y. Luo, Adv. Sci. **5**, 1800661 (2018).
[38] A. Arbabi, E. Arbabi, S. M. Kamali, Y. Horie, S. Han, and A. Faraon, Nat. Commun. **7**, 13682 (2016).
[39] L. Yan, W. Zhu, M. F. Karim, H. Cai, A. Y. Gu, Z. Shen, P. H. J. Chong, D. L. Kwong, C. W. Qiu, and A. Q. Liu, Adv. Mater. **30**, 1802721 (2018).
[40] C. Jin, M. Afsharnia, R. Berlich, S. Fasold, C. Zou, D. Arslan, I. Staude, T. Pertsch, and F. Setzpfandt, Adv. Photonics **1**, 1 (2019).
[41] Y. Zhao, M. A. Belkin, and A. Alù, Nat. Commun. **3**, 870 (2012).
[42] B. Sain, C. Meier, and T. Zentgraf, Adv. Photonics **1**, 1 (2019).
[43] J. M. Kontio, H. Husu, J. Simonen, M. J. Huttunen, J. Tommila, M. Pessa, and M. Kauranen, Opt. Lett. **34**, 1979 (2009).

[44] H. Suchowski, D. Oron, A. Arie, and Y. Silberberg, Phys. Rev. A **78**, 063821 (2008).
[45] H. Suchowski, V. Prabhudesai, D. Oron, A. Arie, and Y. Silberberg, Opt. Express **17**, 12731 (2009).
[46] D. K. Polyushkin, E. Hendry, E. K. Stone, and W. L. Barnes, Nano Lett. **11**, 4718 (2011).
[47] L. Luo, I. Chatzakis, J. Wang, F. B. Niesler, M. Wegener, T. Koschny, and C. M. Soukoulis, Nat. Commun. **5**, 3055 (2014).
[48] S. Keren-Zur, M. Tal, S. Fleischer, D. M. Mittleman, and T. Ellenbogen, Nat. Commun. **10**, 1778 (2019).

PUBLICATION II

Multiply-resonant second-harmonic generation using surface lattice resonances in aluminum metasurfaces

Timo Stolt, Anna Vesala, Heikki Rekola, Petri Karvinen, Tommi K. Hakala, and Mikko J. Huttunen

Optics Express 30.3 (2022), pp. 3620–3631
DOI: 10.1364/OE.449198

Research Article | Vol. 30, No. 3 / 31 Jan 2022 / Optics Express 3620

Optics EXPRESS

Multiply-resonant second-harmonic generation using surface lattice resonances in aluminum metasurfaces

TIMO STOLT,[1] ANNA VESALA,[1] HEIKKI REKOLA,[2] PETRI KARVINEN,[2] TOMMI K. HAKALA,[2] AND MIKKO J. HUTTUNEN[1,*]

[1]*Tampere University, Photonics Laboratory, Physics Unit, Tampere FI-33014, Finland*
[2]*Faculty of Science and Forestry, Department of Physics and Mathematics, University of Eastern Finland, FI-80101 Joensuu, Finland*
[*]*mikko.huttunen@tuni.fi*

Abstract: Nonlinear metamaterials show potential for realizing flat nonlinear optical devices but are generally lacking in terms of achievable conversion efficiencies. Recent work has focused on enhancing nonlinear processes by utilizing high quality factor resonances, such as collective responses known as surface lattice resonances (SLRs) taking place in periodic metal nanoparticle arrays. Here, we investigate how the dispersive nature of SLRs affects the nonlinear responses of SLR-supporting metasurfaces. Particularly, we measure second-harmonic generation from aluminum nanoparticle arrays and demonstrate that by tilting the sample along two orthogonal directions, the sample can be made multiply-resonant for several pump and second-harmonic signal wavelength combinations. Characterized metasurfaces are estimated to exhibit a second-order susceptibility value of 0.40 pm/V, demonstrating aluminum as a potential material for nonlinear metasurfaces.

1. Introduction

Recent developments in miniaturized photonic devices have created a demand for nanoscale nonlinear optical components, which could be potentially addressed by a novel material class known as metamaterials [1]. They are artificial structures consisting of subwavelength building blocks, often referred to as meta-atoms. By carefully selecting the meta-atom properties, the bulk metamaterial can exhibit properties not found in natural materials, such as nanoscale phase-engineering capabilities [2,3]. Through these unique properties, metamaterials show potential for realizing novel flat photonic components, such as metalenses and meta-holograms [4,5].

In addition to their linear optical properties, also the nonlinear optical properties of metamaterials have been investigated [6–9]. For example, plasmonic metamaterials consisting of metal nanoparticles show potential for enabling efficient nonlinear processes in chip-scale devices [10,11]. The optical properties of metal nanoparticles are dominated by the collective oscillations of conduction electrons, known as localized surface plasmons [12]. They exhibit resonant behavior, known as localized surface plasmon resonances (LSPRs), which results in increased local fields near the nanoparticle surface. This local-field enhancement boosts light-matter interaction, including nonlinear processes that scale with high powers of the driving field. Therefore, utilizing LSPRs leads to dramatic enhancements of the nonlinear responses of metal nanoparticles [13–19]. Unfortunately, LSPRs are associated with considerable losses, significantly limiting their potential for nonlinear optics. However, by arranging metal nanoparticles into periodic lattices, collective responses referred to as surface lattice resonances (SLRs) emerge. They are associated with much narrower resonance linewidths and higher quality factors (Q-factors) than LSPRs [20–23]. This indicates that SLRs are also associated with remarkably stronger local-field

#449198 https://doi.org/10.1364/OE.449198
Journal © 2022 Received 1 Dec 2021; revised 11 Jan 2022; accepted 13 Jan 2022; published 19 Jan 2022

Optics EXPRESS

enhancements and smaller losses. Consequently, SLRs can be utilized to enhance the nonlinear responses of metasurfaces [24–26].

Most studies on nonlinear plasmonics have focused on singly-resonant metamaterials exhibiting a resonance either at the pump or signal wavelengths of the studied nonlinear processes [24,25,27]. However, nonlinear processes scale with the local fields at all interacting wavelengths [12,28]. Thus, for example a process of second-harmonic generation (SHG) can be enhanced by utilizing multiply-resonant materials, where the resonance enhancement occurs both at the signal and pump wavelengths [29–34]. Furthermore, recent numerical work suggests that multiply-resonant operation based on SLRs could dramatically increase nonlinear responses of plasmonic metasurfaces [35].

Here, we experimentally demonstrate multiply-resonant enhancement of SHG in SLR-exhibiting metasurfaces consisting of V-shaped aluminum (Al) nanoparticles. We achieve multiply-resonant operation by tilting the investigated metasurfaces and by utilizing the dispersion of SLRs. The multiply-resonant conditions are fulfilled at several different wavelengths, demonstrating the tunability of SLR-enhanced responses. The measured SH signals correspond to nonlinear susceptibility tensor values of 0.40 pm/V, which is of the same order-of-magnitude as the typical values for traditional nonlinear materials [28].

2. Theory

2.1. Surface lattice resonances

The optical properties of metals are governed by the collective oscillations of conduction electrons known as plasmons [12]. At resonant conditions, the strength of light–matter interaction increases, resulting in dramatic changes of, e.g., reflectivity and absorbance of the bulk metal. In the case of metal nanoparticles, plasmons are restricted to the particle surface [36]. Therefore, in resonant conditions, incident light is coupled to the local plasmon modes resulting in increased local fields near the nanoparticle surface. This phenomenon is known as LSPR, and it is widely used in many applications of plasmonic metamaterials [37–39]. LSPRs are associated with relatively broad linewidths and therefore low Q-factors ($Q \sim 10$), which indicate extremely short resonance lifetimes but, on the other hand, considerable losses and relatively low local-field enhancements. The low field enhancement can be compensated by using optically dense plasmonic structures and intense pulsed laser sources. Unfortunately, the subsequent strong absorption decrease damage thresholds of the plasmonic structures, significantly limiting the usable input power and thus the strength of the nonlinear responses of plasmonic metamaterials.

A viable approach to decrease losses and increase the interaction strength in plasmonic metamaterials is to utilize SLRs. They are propagating surface modes resulting from radiative coupling of localized surface plasmons in a periodic grating of nanoparticles. They are associated with remarkably high Q-factors ($Q \sim 1000$) [23], indicating significantly higher local-field enhancements than the ones associated with LSPRs. Because SLRs result from diffractive properties of the metasurface, their spectral locations are related to the Rayleigh anomalies (RAs) according to [40,41]

$$\lambda_{l,m}(\theta,\phi) = -A_{l,m}(\theta,\phi) + \sqrt{A_{l,m}^2(\theta,\phi) - B_{l,m}(\theta)}, \tag{1}$$

where l and m are the diffraction orders along the Cartesian coordinates of the grating, θ is the incidence angle in the incidence plane, and ϕ is the azimuthal angle that defines the orientation of the incidence plane with respect to the Cartesian coordinates. For a rectangular metasurface with lattice constants p_x and p_y along the surface Cartesian coordinates (see Fig. 1), the variables $A_{l,m}(\theta,\phi)$ and $B_{l,m}(\theta)$ are given by

$$A_{l,m}(\theta,\phi) = \frac{\sin\theta}{(l/p_x)^2 + (m/p_y)^2}\left(\frac{l\sin\phi}{p_x} + \frac{m\cos\phi}{p_y}\right), \tag{2}$$

Optics EXPRESS

$$B_{l,m}(\theta) = \frac{\sin^2\theta - n^2}{(l/p_x)^2 + (m/p_y)^2}, \tag{3}$$

where n is the refractive index of the surrounding material.

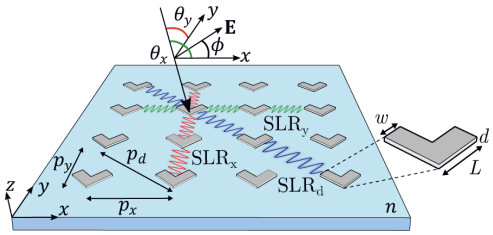

Fig. 1. Surface lattice resonance (SLR) modes propagate along the metasurface. Their spectral location depends on numerous factors: incidence angle (θ), azimuthal angle (ϕ), refractive index (n), and lattice constants p_x, p_y, and p_d. For y-polarized light ($\phi = 90°$), parallel SLRs (green waves) depend on θ_x and p_x, and for x-polarized light ($\phi = 0°$), the emerging SLRs depend on and θ_y and p_y (red waves). The diagonal SLRs (blue waves) occur for both polarizations. In this work, we consider metasurfaces consisting of V-shaped nanoparticles with arm length L, arm width w, and thickness d. These parameters dictate localized surface plasmon resonances of individual nanoparticles, which also impact the SLR formation.

In this work, we focus on in-plane SLRs that occur when the polarization of the incident light and the induced dipoles in the nanoparticles are parallel to the metasurface, i.e., when the incident light is TE polarized [42]. These SLR modes propagate along the metasurface in the directions that are not parallel with incident polarization. The most obvious option for nanoparticles to couple is along the direction that is perpendicular to the incident polarization, resulting in surface modes we name as parallel SLR.

Here, we are interested in first-order parallel SLRs for light polarized along either the x- or y-axis of the rectangular metasurface. For x-polarized light ($\phi = 0°$), the SLR wavelength depends on p_y and the incidence angle θ_y on the yz-plane (see Fig. 1) as given by

$$\lambda_x(\theta_y) = \lambda_{0,\pm1}(\theta_y) = p_y\left(n \mp \sin\theta_y\right). \tag{4}$$

For y-polarized light ($\phi = 90°$), a similar condition is found to be

$$\lambda_y(\theta_x) = \lambda_{\pm1,0}(\theta_x) = p_x\left(n \mp \sin\theta_x\right), \tag{5}$$

where θ_x is the incidence angle along the xz-plane with respect to the metasurface normal.

Plasmon modes in a rectangular lattice can couple also along the diagonal of the lattice unit cell, resulting in diagonal SLRs (blue waves in Fig. 1). At normal incidence ($\theta_x = \theta_y = 0°$), the diagonal SLRs occur at the same wavelength for both incident polarizations, which for first-order SLRs is given by

$$\lambda_d = n\frac{p_x p_y}{p_d}, \tag{6}$$

where $p_d = \sqrt{p_x^2 + p_y^2}$ is the diagonal of the metasurface unit cell.

Overall, the spectral location of the SLR depends on the polarization of the interacting wave, the lattice constants p_x and p_y, the refractive index of the surrounding material n, and the incidence angles θ_x and θ_y, providing us multiple parameters to control the occurrence of SLRs.

Optics EXPRESS

2.2. Second-harmonic generation in multiply-resonant structures

The SH responses of metamaterials depend on the local fields $E_{\mathrm{loc}}(\omega)$ and $E_{\mathrm{loc}}(2\omega)$, oscillating at the fundamental and SH frequency, respectively [12,28]. Therefore, we can write for far-field SH emission $E_{\mathrm{nl}}(2\omega)$ that

$$E_{\mathrm{nl}}(2\omega) \propto \chi^{(2)} E_{\mathrm{loc}}(2\omega) E^2_{\mathrm{loc}}(\omega), \tag{7}$$

where $\chi^{(2)}$ is the effective nonlinear susceptibility of the metasurface.

The local electric fields in Eq. (7) can be enhanced by utilizing metasurface responses, such as LSPRs and SLRs, at the interacting wavelengths. Most works have considered singly-resonant metasurfaces that exhibit resonances at either the signal or more commonly at the fundamental wavelength [24,43]. However, the nonlinear responses can be further enhanced by utilizing multiply-resonant metasurfaces that exhibit resonances at both interacting wavelengths. For example, Celebrano et al. designed metasurfaces consisting of gold nanoparticles exhibiting LSPRs to enhance SHG [30]. In this work, we extend the approach to metasurfaces based on SLRs with clear benefits. As mentioned before, SLRs are very dependent on the polarization state and propagation direction of the interacting laser fields. Therefore, we design our metasurfaces for type-I SHG, where both fundamental fields have the same polarization state k, while the emitted signal field is associated with a different polarization state j. For this process, we can rewrite Eq. (7) as follows:

$$E_{nl}(\mathbf{k}_2, 2\omega) \propto \chi^{(2)}_{jkk} E_{\mathrm{loc},j}(\mathbf{k}_2, 2\omega) E^2_{\mathrm{loc},k}(\mathbf{k}_1, \omega), \tag{8}$$

where $\mathbf{k}_1$ and $\mathbf{k}_2$ are the wavevectors of fundamental and SH beams, respectively, and $\chi^{(2)}_{jkk}$ is the corresponding effective nonlinear susceptibility tensor component.

3. Methods

3.1. Sample fabrication

For this work, we fabricated Al nanoparticle arrays with a total area of 300×300 μm. The structures were fabricated on a pre-cleaned microscope slide (Schott Nexterion, D263T glass). A 200 nm layer of PMMA-resist (MicroChem, 950k) was spin-coated on top and baked on a hot plate at 180°C for 180 s. A 10 nm layer of Al was evaporated on the resist to act as a conductive layer for electron beam lithography.

The patterning was done using a Raith EBPG 5000+ 100 kV electron beam lithography system. After patterning the Al layer was removed using a 1% sodium hydroxide solution. The resist was then developed using a 1:3 mixture of methyl isobutyl ketone and isopropanol (IPA) for 15 s, followed by a 30 s immersion in IPA. The sample was dried with nitrogen and placed in an electron beam evaporator for depositing 30 nm of Al. Finally, a liftoff process was performed by soaking the sample in acetone overnight and gently washing the surface with more acetone using a syringe. This removes the resist and excess metal on top of it, leaving only the nanoparticles on the glass substrate. The sample was then rinsed with IPA and dried with nitrogen.

Before the measurements, we covered the metasurface with index-matching oil and an anti-reflection (AR) coated coverslip with the AR wavelength band at 1000–1300 nm. This way, the nanoparticles were assured to have a homogeneous surrounding, and we avoided any Fabry–Pérot resonances resulting from multiple reflections from different interfaces present in the fabricated devices.

3.2. Experiments

In this work, we characterized both linear and nonlinear optical properties of our metasurfaces using two different experimental setups. Here, only short descriptions are given while further details are described in Supplement 1.

Optics EXPRESS

In order to characterize the linear optical properties of our samples, especially the properties of the occurring SLRs, we measured transmission spectra of our samples (see Figs. 2, 3(a)–(b), and 4(a)–(b)) Here, we used a broadband halogen lamp, a linear polarizer, and spectrometers to locate SLRs. We placed the sample on a goniometer on a rotational stage, which was connected to a 3-axis translational stage. This enabled continuous control over sample position and orientation, especially with respect to angles θ_y and θ_x. By measuring the transmission spectra at different angles, we extracted the dispersion relation graphs shown in Figs. 3(a)–(b) and 4(a)–(b).

In our nonlinear experiments, we used an optical parametric oscillator (1000–1300 nm) pumped with a titanium sapphire femtosecond laser (800 nm, repetition rate 82 MHz, pulse duration 200 fs) as a tunable laser source. We set our laser power to 75 mW using a combination of a linear polarizer, an achromatic half-wave plate and a reference diode. The laser beam was then weakly focused on the sample using an achromatic lens (f = 500 mm), resulting in estimated beam diameter ($1/e^2$ of maximum intensity) of 75 μm and peak intensity of 115 MW/cm^2 at the sample plane. Similar to the transmission experiments, we placed the sample on a stage that allows fine-tuning of sample position and accurate control of θ_y and θ_x. In this setup, the rotation stage was motorized allowing continuous incidence angle scans. The generated SH signal was collected with a photo-multiplier tube. By repeating angle scans for different pump wavelengths, we acquired the (λ, θ)-graphs for the SHG emission from studied metasurfaces, shown in Figs. 3(c) and 4(c).

4. Design and results

Our metasurfaces consisted of V-shaped Al nanoparticles with arm length L = 100 nm, arm width w = 70 nm, and thickness d = 30 nm (see Fig. 1). The nanoparticles were fabricated on a glass substrate (refractive index n = 1.51) [See the Sample Fabrication section for details]. The nanoparticles were arranged in rectangular lattices with lattice constants p_y and p_x along and orthogonal to the nanoparticle symmetry axis (y-axis), respectively (see Fig. 1). In such configuration, the metasurface has the following non-zero second-order susceptibility tensor components $\chi^{(2)}_{yyy}$, $\chi^{(2)}_{yxx}$, and $\chi^{(2)}_{xxy} = \chi^{(2)}_{xyx}$ [44]. Additionally, under illumination of x- or y-polarized

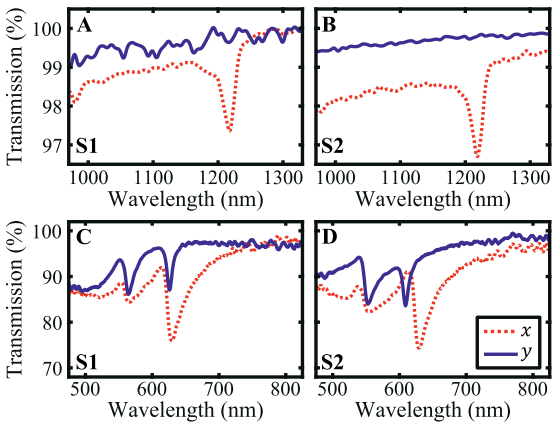

Fig. 2. Measured tranmsission spectra for the studied periodic aluminum metasurfaces (see Fig. 1). (a)–(b) The two studied samples, S1 and S2, had p_y = 813 nm, resulting in first-order SLRs at 1220 nm for x-polarized light (dotted red lines). (c)–(d) S1 (S2) has p_x = 410 nm (398 nm), resulting in first-order SLR at 626 nm (609 nm) for y-polarized light (blue solid lines). Furthermore, S1 (S2) exhibit diagonal SLRs at 560 nm (546 nm).

Optics EXPRESS

light, local field hotspots form in the tips of the V-shaped nanoparticles [45]. We note that similar array configurations have been shown to result in SLRs at different spectral regions [46].

Here, we studied two metasurfaces composed of identical nanoparticles but varying in their array periodicities. For sample S1, the periodicities were $p_x = 410$ nm and $p_y = 813$, and for sample S2, $p_x = 398$ nm and $p_y = 813$ nm. Since both samples are composed of identical nanoparticles, they both exhibit LSPRs centered at 475 nm and 550 nm for y- and x-polarized light, respectively (see Supplement 1 for more information). The samples also have the same $p_y = 813$ nm, and therefore, at normal incidence, they exhibit the first-order SLR for x-polarized light at $\lambda_x(0°) = 1220$ nm (see Fig. 2(a)). The two samples differ in p_x, and therefore, also in location of parallel SLRs for y-polarized light ($\lambda_y(\theta_x)$) and diagonal SLRs for both polarizations (λ_d). At normal incidence, these SLRs occur at $\lambda_y(0°) = 626$ nm (609 nm) and $\lambda_d = 560$ nm (546 nm) for the sample S1 (S2).

Our metasurfaces were designed for the multiply-resonant enhancement of SHG corresponding to $\chi^{(2)}_{yxx}$, i.e., to the process with x-polarized pump and y-polarized SH signal. The multiply-resonant operation is therefore enabled for SHG processes where the pump is coupled to the x-polarized SLR and the signal to the y-polarized SLR, either parallel or diagonal. Thus, we can write the condition for multiply-resonant operation with resonance wavelengths $\lambda_x(\theta_y)$ and $\lambda_y(\theta_x)$ to be

$$\lambda_x(\theta_y) = 2\lambda_y(\theta_x), \tag{9}$$

where θ_y and θ_x emphasize the fact that we modify the SLR wavelengths by rotating the sample accordingly. This way, the experiment corresponds to a situation where the sample is illuminated at an angle θ_y and the SH signal is collected at an angle θ_x.

For sample S1, the multiply-resonant condition of Eq. (9) is not fulfilled at normal incidence, but can be achieved by utilizing the dispersion of the occurring SLRs (see Figs. 3(a) and 3(b)). Here, we selected $\theta_y = 3°$ for which S1 exhibit x-polarized SLRs at 1176 nm and 1250 nm (red circle in Fig. 3(a)). Then, we utilize the dispersion of y-polarized SLRs to fulfill the multiply-resonant condition at three different conditions (dashed circles in Fig. 3(b)). For the pump wavelength of 1176 nm, the multiply-resonant condition is fulfilled at $\theta_x = \pm 5°$, where parallel SLRs (green dots) and diagonal SLRs (blue dots) overlap at 590 nm. For the pump wavelength of 1250 nm, the multiply-resonant condition is fulfilled conveniently at $\theta_x = 0°$, where the fundamental y-polarized SLR occurs at 626 nm. These locations of multiply-resonant operation are marked in Figs. 3(a) and 3(b) with dashed circles.

To demonstrate multiply-resonant operation using the angle–wavelength combinations mentioned above, we set $\theta_y = 3°$ and measured the SHG (θ_x, λ) -spectrum corresponding to $\chi^{(2)}_{yxx}$, i.e., to the SHG process with x-polarized pump and y-polarized signal (see Fig. 3(c)). The SH emission pattern follows the dispersion of y-polarized SLRs, and the signal reaches its maximum when multiple SLRs occur at interacting wavelengths (green and blue circles). At these locations, the SH emission is 8-fold, when compared against the off-resonance signal. The maximum emission power is 5.7 fW, which corresponds to a conversion efficiency of 7.6×10^{-14}. By using the method presented by Herman et al. [47,48], we estimate a value $\chi^{(2)}_{yxx} = 0.36$ pm/V for the sample S1 (see Supplement 1 for calculation details).

However, the maximum SH signal is achieved, when diagonal and parallel SLRs overlap at 590 nm. This overlap results in stronger resonance than the separate SLRs. Additionally, the two SLRs near the pump wavelengths 1176 nm and 1250 nm are considerably weak, when compared against, e.g., the normal-incidence SLR at 1220 nm. Thus, we cannot confidently confirm that the strong signals observed with the pump wavelength of 1176 nm results from multiply-resonant operation or simply from overlapping SLRs at the signal wavelength. To undoubtedly demonstrate multiply-resonant enhancement, we measured the SH response from the sample S2.

For the sample S2, the multiply-resonant condition in Eq. (9) is fulfilled at normal incidence ($\theta_y = 0°$ and $\theta_x = 0°$) for the pump wavelength of 1220 nm (red circle in Fig. 4(a) and green circle

Optics EXPRESS

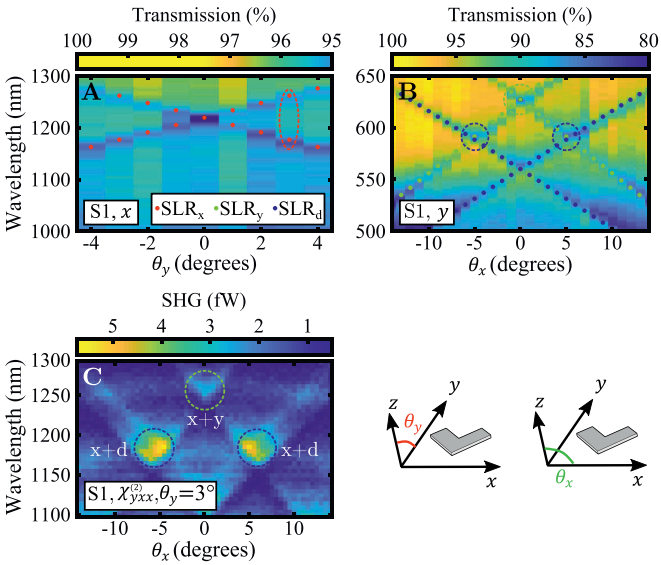

Fig. 3. The dispersion graphs of transmission for (a) x- and (b) y-polarized incident light. (c) The dispersion graph of SHG emission for the sample S1, with x-polarized pump and y-polarized SHG signal. (a)–(b) At normal incidence ($\theta_y = \theta_x = 0°$), sample S1 exhibits first-order parallel SLRs at 1220 nm and 626 nm for x-polarized (red dots) and y-polarized (green dots) light, respectively. Additionally, diagonal SLRs (blue dots) occur at 560 nm for normal incidence illumination. By tilting the sample, the SLRs shift from their normal-incidence values. (c) SLRs occurring near the pump and signal wavelengths impact the SHG associated with $\chi^{(2)}_{yxx}$. By setting $\theta_y = 3°$ (dashed circle in a) and tilting sample with respect to x-axis (θ_x), the SH emission is enhanced with three different wavelength–angle combinations (dashed circles in b). At $\theta_x = 0°$, the parallel SLRs for x- and y-polarized light enhance SHG at 1250 nm (green circle). At $\theta_x = \pm 5°$, parallel and diagonal SLRs for y-polarized light overlap at 590 nm, and parallel SLR for x-polarization occurs at 1176 nm. Combined, these SLRs enhance SHG near 1180 nm (blue circles).

in (b)). By rotating the sample along the x-axis, i.e., by changing θ_x, the diagonal SLRs (red dots) shift from $\lambda_d = 546$ nm. At $\theta_x = \pm 11°$ $\lambda_d = 610$ nm and the multiply-resonant condition is again fulfilled (blue circles in Fig. 4(b)).

To confirm the multiply-resonant operation, we measured the SHG (θ_x, λ)-spectrum by setting $\theta_y = 0°$ and scanning over a wavelength range of 1000–1300 nm and an angle range (θ_x) from $-15°$ to $15°$ (see Fig. 4(c)). From the SH emission pattern it is clear, that the x-polarized SLR enhances the nonlinear response, as there is significant signal at all values of θ_x at the pump wavelength of 1220 nm. Other parts of the SH emission pattern again follows the dispersion of y-polarized SLRs and reaches its maximum at multiply-resonant conditions, i.e., at 1220 nm when $\theta_x = [0°, \pm 11°]$ (marked with green and blue circles). Now, the multiply-resonant enhancement results in 10-fold enhancement and the maximum emission power of 5.8 fW. The measured signal therefore corresponds to conversion efficiency 7.7×10^{-14} and $\chi^{(2)}_{yxx} = 0.40$ pm/V.

For sample S2, the impact of multiply-resonant operation is more evident. The SH emission with the pump wavelength of 1220 nm is visibly enhanced at all angles θ_x, demonstrating the impact of the SLR at the pump wavelength. More importantly, the signal reaches the maximum

Optics EXPRESS

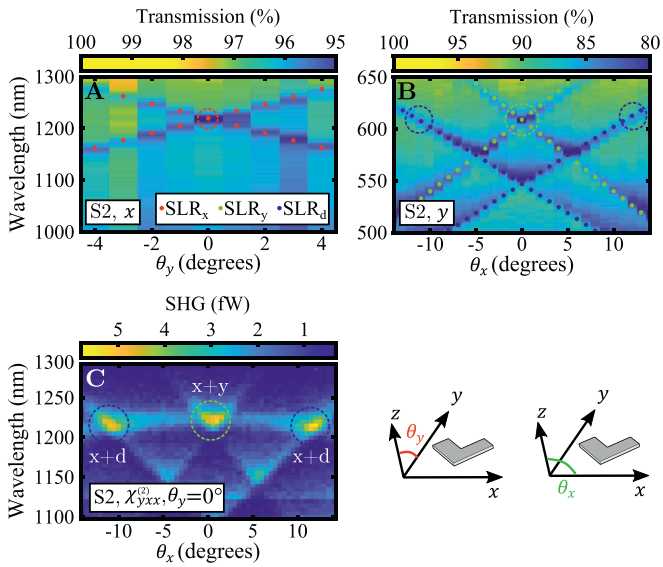

Fig. 4. The dispersion graphs of transmission for (a) x- and (b) y-polarized incident light for the sample S2. (c) The dispersion graph of SHG emission for the sample S2, with x-polarized pump and y-polarized SHG signal. (a)–(b) At normal incidence, sample S2 exhibits first-order parallel SLRs at 1220 nm and 609 nm for x-polarized (red dots) and y-polarized (green dots) light, respectively. The sample exhibits also diagonal SLRs (blue dots) at 546 nm. Tilting sample along y-axis (θ_y) and x-axis (θ_x) will shift x- and y-polarized SLRs from their normal incidence values. By setting $\theta_y = 0°$, the multiply-resonant condition for SHG associated with $\chi^{(2)}_{yxx}$ ($\lambda_x = 2\lambda_y$) is fulfilled when $\theta_x = [0°, \pm 11°]$ (dashed circles). (c) SLRs enhance the second-harmonic emission and the maximum value is achieved at the multiply-resonant condition. With the incident angle set to $\theta_y = 0°$, this occurs at the pump wavelength 1220 nm with three different emission angles θ_x. First, at $\theta_x = 0°$ (green circle), the multiply-resonant condition is fulfilled with parallel SLRs. At $\theta_x = \pm 11$ (blue circles), S2 exhibit diagonal SLRs at 610 nm, therefore fulfilling the multiply-resonant condition.

level only, when the multiply-resonant condition is fulfilled with parallel and diagonal SLRs occurring at 610 nm, marked in Fig. 4(c) with green and blue circles, respectively.

5. Discussion

Our results demonstrate two things. First, only few studies have characterized the nonlinear properties of Al nanostructures [49,50]. This is due to the fact that Al spontaneously forms oxides (Al_2O_3), which impacts the plasmonic properties of the Al nanoparticles [51]. Therefore, many researchers prefer more stable plasmonic nanostructures, such as gold and silver nanoparticles [52]. However, our work utilizes the diffractive properties of plasmonic metasurfaces, which are less sensitive to the changes in LSPRs induced by the oxidation of Al nanoparticles. Furthermore, the use of gold or silver nanoparticles would have shifted LSPRs to longer wavelengths, i.e., to the SHG wavelength range of our studies. Thus, we would not have achieved multiply-resonant operation by utilzing only SLRs if gold or silver nanoparticles were used.

Optics EXPRESS

Second, our results demonstrate the multiply-resonant enhancement of SHG by utilizing only SLRs. Other works have either utilized only LSPRs or singly-resonant structures that exhibit SLRs near either the pump or signal wavelengths [41]. Unfortunately, our results demonstrate only 10-fold on-and-off-resonance enhancement and SH signal levels of 5 fW, which are significantly lower than the corresponding values acquired with singly-resonant SLR-based structures [24,25]. A major reason for this difference is the fact that our samples exhibited relatively weak and low-Q SLRs (extinction $\leq 5\%$ and $Q \approx 60$) at the pump wavelength. Thus, the SLR-induced field enhancements were also relatively weak. These points originated mostly from the fact that the nanoparticles themselves were relatively small when compared against the lattice constant p_y, which weakened the inter-particle coupling. However, our OPO restricted the investigation to pump wavelengths of 1000–1300 nm and signal wavelengths of 500–650 nm. Having larger nanoparticles would have shifted the LSPRs to the desired signal wavelength range, preventing us from using only SLRs to realize multiply-resonant operation. Furthermore, highly transparent structures could prove to be useful in future investigations. For example, multiple such structures could be stacked on top of each other to achieve phase-matched SHG boosting the overall nonlinear signal [53].

Another factor that might explain the weakness of the measured SHG signals is the possible poor spatial overlap between local fields induced by different SLR modes. We note that such mode-overlap calculations have been already performed for very similar periodic metasurfaces elsewhere [54], where the use of oblique angles of incidence did not dramatically affect the estimated SHG signals. Therefore, we do not think this reason is the most probable one to explain the weakness of the SHG signal. Unfortunately, due to our restricted computational capabilities, we did not have the resources to repeat such calculations for the general 2D situation we have in this work experimentally investigated. We also note, that due to the non-local nature of SLRs, the conventional susceptibility formalism may not anymore be adequate if a broad range of angles of incidence would be used. In such case, it would seem preferable to estimate the nonlinear responses by performing mode-overlap calculations [54]. Alternatively, it might be possible to estimate angle-dependent nonlinear responses by using an approach based on the nonlinear discrete-dipole approximation [55]. Although the latter approach approximates individual nanoparticles as point-like scatterers, and does not therefore permit mode-overlap calculations, the approach is computational less intensive than approaches based on full-wave simulations.

Despite the relatively low signal levels, our results demonstrate how SHG can be modified by utilizing the dispersion of SLRs. As is shown in Figs. 3 and 4, SLRs near both pump and signal wavelengths enhance the SH response, which reaches its maximum at the multiply-resonant conditions. By tilting the sample accordingly, we can change the multiply-resonant wavelength, i.e., tune the wavelength of the maximum SH response. Such post-fabrication tunability could prove useful for realizing other nonlinear processes in resonant metasurfaces, such as sum-frequency generation, difference-frequency generation, and third-harmonic generation [35]. Demonstrating these processes could pave the path towards flat and tunable laser sources with the operation band ranging from the ultraviolet to the terahertz (THz) region of the electromagnetic spectrum.

6. Conclusion

In summary, we demonstrate multiply-resonant enhancement of second-harmonic generation from Al metasurfaces. The achieved signal levels correspond to the nonlinear susceptibility tensor component value of 0.40 pm/V, which is the same order-of-magnitude as the susceptibility values of conventional nonlinear optical materials, demonstrating the potential of Al metasurfaces for nonlinear optics. Here, we achieve the multiply-resonant enhancement by utilizing collective responses of periodic metal nanoparticle arrays known as surface lattice resonances. Due to

Optics EXPRESS

the dispersion of surface lattice resonances, we can control the multiply-resonant enhancement by tilting the sample. As a result, we achieve multiply-resonant enhancement with several different combinations of signal wavelength, incidence angle, and signal emission angle, therefore demonstrating tunable second-harmonic generation. Our methods show promise for realizing other nonlinear processes in plasmonic metasurfaces. Such structures could pave the path towards flat and tunable nonlinear devices.

Funding. Academy of Finland (308596, 320165, 320166, 322002); Jenny ja Antti Wihurin Rahasto (Doctoral study grant).

Acknowledgements. Authors acknowledge Jarno Reuna for providing anti-reflection coatings.

Disclosures. Authors declare no conflicts of interest.

Data availability. Data underlying the results presented in this paper are not publicly available at this time but may be obtained from the authors upon reasonable request.

Supplemental document. See Supplement 1 for supporting content.

References

1. C. M. Soukoulis and M. Wegener, "Past achievements and future challenges in the development of three-dimensional photonic metamaterials," Nat. Photonics **5**(9), 523–530 (2011).
2. P. Genevet, F. Capasso, F. Aieta, M. Khorasaninejad, and R. Devlin, "Recent advances in planar optics: from plasmonic to dielectric metasurfaces," Optica **4**(1), 139 (2017).
3. S. Chen, Z. Li, Y. Zhang, H. Cheng, and J. Tian, "Phase Manipulation of Electromagnetic Waves with Metasurfaces and Its Applications in Nanophotonics," Adv. Opt. Mater. **6**(13), 1800104 (2018).
4. F. Aieta, M. A. Kats, P. Genevet, and F. Capasso, "Achromatic metasurfaces by dispersive phase compensation," Science **347**(6228), 1342–1345 (2015).
5. M. Khorasaninejad, A. Ambrosio, P. Kanhaiya, and F. Capasso, "Broadband and chiral binary dielectric meta-holograms," Sci. Adv. **2**(5), 1 (2016).
6. A. D. Boardman, V. V. Grimalsky, Y. S. Kivshar, S. V. Koshevaya, M. Lapine, N. M. Litchinitser, V. N. Malnev, M. Noginov, Y. G. Rapoport, and V. M. Shalaev, "Active and tunable metamaterials," Laser Photonics Rev. **5**(2), 287–307 (2011).
7. S. Keren-Zur, L. Michaeli, H. Suchowski, and T. Ellenbogen, "Shaping light with nonlinear metasurfaces," Adv. Opt. Photonics **10**(1), 309 (2018).
8. A. Krasnok, M. Tymchenko, and A. Alù, "Nonlinear metasurfaces: a paradigm shift in nonlinear optics," Mater. Today **21**(1), 8–21 (2018).
9. B. Sain, C. Meier, and T. Zentgraf, "Nonlinear optics in all-dielectric nanoantennas and metasurfaces: a review," Adv. Photonics **1**(2), 024002 (2019).
10. M. Kauranen and A. V. Zayats, "Nonlinear plasmonics," Nat. Photonics **6**(11), 737–748 (2012).
11. J. Lee, M. Tymchenko, C. Argyropoulos, P. Y. Chen, F. Lu, F. Demmerle, G. Boehm, M. C. Amann, A. Alù, and M. A. Belkin, "Giant nonlinear response from plasmonic metasurfaces coupled to intersubband transitions," Nature **511**(7507), 65–69 (2014).
12. S. A. Maier, *Plasmonics: fundamentals and applications* (Springer Science & Business Media, 2007).
13. M. W. Klein, C. Enkrich, M. Wegener, and S. Linden, "Second-harmonic generation from magnetic metamaterials," Science **313**(5786), 502–504 (2006).
14. M. Lapine, I. V. Shadrivov, and Y. S. Kivshar, "Colloquium: Nonlinear metamaterials," Rev. Mod. Phys. **86**(3), 1093–1123 (2014).
15. J. Butet, P. F. Brevet, and O. J. Martin, "Optical Second Harmonic Generation in Plasmonic Nanostructures: From Fundamental Principles to Advanced Applications," ACS Nano **9**(11), 10545–10562 (2015).
16. M. S. Nezami and R. Gordon, "Localized and propagating surface plasmon resonances in aperture-based third harmonic generation," Opt. Express **23**(25), 32006 (2015).
17. G. Li, S. Zhang, and T. Zentgraf, "Nonlinear photonic metasurfaces," Nat. Rev. Mater. **2**(5), 17010 (2017).
18. E. Rahimi and R. Gordon, "Nonlinear Plasmonic Metasurfaces," Adv. Opt. Mater. **6**(18), 1800274 (2018).
19. M. J. Huttunen, R. Czaplicki, and M. Kauranen, "Nonlinear plasmonic metasurfaces," J. Nonlinear Opt. Phys. Mater. **28**(01), 1950001 (2019).
20. W. Wang, M. Ramezani, A. I. Väkeväinen, P. Törmä, J. G. Rivas, and T. W. Odom, "The rich photonic world of plasmonic nanoparticle arrays," Mater. Today **21**(3), 303–314 (2018).
21. V. G. Kravets, A. V. Kabashin, W. L. Barnes, and A. N. Grigorenko, "Plasmonic Surface Lattice Resonances: A Review of Properties and Applications," Chem. Rev. **118**(12), 5912–5951 (2018).
22. A. D. Utyushev, V. I. Zakomirnyi, and I. L. Rasskazov, "Collective lattice resonances: Plasmonics and beyond," Rev. Phys. **6**, 100051 (2021).

Optics EXPRESS

23. M. S. Bin-Alam, O. Reshef, Y. Mamchur, M. Z. Alam, G. Carlow, J. Upham, B. T. Sullivan, J.-M. Ménard, M. J. Huttunen, R. W. Boyd, and K. Dolgaleva, "Ultra-high-q resonances in plasmonic metasurfaces," Nat. Commun. **12**(1), 974 (2021).
24. L. Michaeli, S. Keren-Zur, O. Avayu, H. Suchowski, and T. Ellenbogen, "Nonlinear surface lattice resonance in plasmonic nanoparticle arrays," Phys. Rev. Lett. **118**(24), 243904 (2017).
25. D. C. Hooper, C. Kuppe, D. Wang, W. Wang, J. Guan, T. W. Odom, and V. K. Valev, "Second harmonic spectroscopy of surface lattice resonances," Nano Lett. **19**(1), 165–172 (2019).
26. A. Han, C. Dineen, V. E. Babicheva, and J. V. Moloney, "Second harmonic generation in metasurfaces with multipole resonant coupling," Nanophotonics **9**(11), 3545–3556 (2020).
27. B. Shen, L. Liu, Y. Li, S. Ren, J. Yan, R. Hu, and J. Qu, "Nonlinear spectral-imaging study of second- and third-harmonic enhancements by surface-lattice resonances," Adv. Opt. Mater. **8**(8), 1901981 (2020).
28. R. W. Boyd, *Nonlinear optics* (Academic Press, San Diego, 2020), 4th ed.
29. K. Thyagarajan, S. Rivier, A. Lovera, and O. J. Martin, "Enhanced second-harmonic generation from double resonant plasmonic antennae," Opt. Express **20**(12), 12860–12865 (2012).
30. M. Celebrano, X. Wu, M. Baselli, S. Großmann, P. Biagioni, A. Locatelli, C. De Angelis, G. Cerullo, R. Osellame, B. Hecht, L. Duò, F. Ciccacci, and M. Finazzi, "Mode matching in multiresonant plasmonic nanoantennas for enhanced second harmonic generation," Nat. Nanotechnol. **10**(5), 412–417 (2015).
31. S. D. Gennaro, M. Rahmani, V. Giannini, H. Aouani, T. P. Sidiropoulos, M. Navarro-Cía, S. A. Maier, and R. F. Oulton, "The Interplay of Symmetry and Scattering Phase in Second Harmonic Generation from Gold Nanoantennas," Nano Lett. **16**(8), 5278–5285 (2016).
32. K. Y. Yang, J. Butet, C. Yan, G. D. Bernasconi, and O. J. Martin, "Enhancement mechanisms of the second harmonic generation from double resonant aluminum nanostructures," ACS Photonics **4**(6), 1522–1530 (2017).
33. M. Minkov, D. Gerace, and S. Fan, "Doubly resonant $\chi^{(2)}$ nonlinear photonic crystal cavity based on a bound state in the continuum," Optica **6**(8), 1039 (2019).
34. L. Soun, B. Fix, H. E. Ouazzani, S. Héron, N. Bardou, C. Dupuis, S. Derelle, J. Jaeck, R. Haïdar, and P. Bouchon, "Experimental demonstration of second-harmonic generation in high χ^2 metasurfaces," Opt. Lett. **46**(6), 1466 (2021).
35. M. J. Huttunen, O. Reshef, T. Stolt, K. Dolgaleva, R. W. Boyd, and M. Kauranen, "Efficient nonlinear metasurfaces by using multiresonant high-Q plasmonic arrays," J. Opt. Soc. Am. B **36**(7), E30–E35 (2019).
36. K. Yao and Y. Liu, "Plasmonic metamaterials," Nanotechnol. Rev. **3**(2), 177–210 (2014).
37. E. Petryayeva and U. J. Krull, "Localized surface plasmon resonance: Nanostructures, bioassays and biosensing-a review," Anal. Chim. Acta **706**(1), 8–24 (2011).
38. X. Gu, T. Qiu, W. Zhang, and P. K. Chu, "Light-emitting diodes enhanced by localized surface plasmon resonance," Nanoscale Res. Lett. **6**(1), 199 (2011).
39. P. F. Gao, Y. F. Li, and C. Z. Huang, "Localized surface plasmon resonance scattering imaging and spectroscopy for real-time reaction monitoring," Appl. Spectrosc. Rev. **54**(3), 237–249 (2019).
40. T. W. Maß and T. Taubner, "Incident angle-tuning of infrared antenna array resonances for molecular sensing," ACS Photonics **2**(10), 1498–1504 (2015).
41. R. Czaplicki, A. Kiviniemi, J. Laukkanen, J. Lehtolahti, M. Kuittinen, and M. Kauranen, "Surface lattice resonances in second-harmonic generation from metasurfaces," Opt. Lett. **41**(12), 2684–2687 (2016).
42. K. Volk, J. P. Fitzgerald, and M. Karg, "In-plane surface lattice and higher order resonances in self-assembled plasmonic monolayers: From substrate-supported to free-standing thin films," ACS Appl. Mater. Interfaces **11**(17), 16096–16106 (2019).
43. R. Czaplicki, A. Kiviniemi, M. J. Huttunen, X. Zang, T. Stolt, I. Vartiainen, J. Butet, M. Kuittinen, O. J. F. Martin, and M. Kauranen, "Less is more – enhancement of second-harmonic generation from metasurfaces by reduced nanoparticle density," Nano Lett. **18**(12), 7709–7714 (2018).
44. R. Czaplicki, J. Mäkitalo, R. Siikanen, H. Husu, J. Lehtolahti, M. Kuittinen, and M. Kauranen, "Second-harmonic generation from metal nanoparticles: Resonance enhancement versus particle geometry," Nano Lett. **15**(1), 530–534 (2015).
45. H. Husu, R. Siikanen, J. Mäkitalo, J. Lehtolahti, J. Laukkanen, M. Kuittinen, and M. Kauranen, "Metamaterials with tailored nonlinear optical response," Nano Lett. **12**(2), 673–677 (2012).
46. M. S. Bin-Alam, O. Reshef, R. N. Ahmad, J. Upham, M. J. Huttunen, K. Dolgaleva, and R. W. Boyd, "Cross-polarized surface lattice resonances in a rectangular lattice plasmonic metasurface," arXiv preprint 2111.02472 (2021).
47. W. N. Herman and L. M. Hayden, "Maker fringes revisited: second-harmonic generation from birefringent or absorbing materials," J. Opt. Soc. Am. B **12**(3), 416–427 (1995).
48. L. Alloatti, C. Kieninger, A. Froelich, M. Lauermann, T. Frenzel, K. Köhnle, W. Freude, J. Leuthold, M. Wegener, and C. Koos, "Second-order nonlinear optical metamaterials: Abc-type nanolaminates," Appl. Phys. Lett. **107**(12), 121903 (2015).
49. B. Metzger, L. Gui, J. Fuchs, D. Floess, M. Hentschel, and H. Giessen, "Strong Enhancement of Second Harmonic Emission by Plasmonic Resonances at the Second Harmonic Wavelength," Nano Lett. **15**(6), 3917–3922 (2015).
50. B. Metzger, M. Hentschel, and H. Giessen, "Probing the Near-Field of Second-Harmonic Light around Plasmonic Nanoantennas," Nano Lett. **17**(3), 1931–1937 (2017).
51. C. Langhammer, M. Schwind, B. Kasemo, and I. Zoric, "Localized surface plasmon resonances in aluminum nanodisks," Nano Lett. **8**(5), 1461–1471 (2008).

Optics EXPRESS

52. E. Benichou, G. Bachelier, C. Jonin, P. F. Brevet, and C. B. Lyon, "Multipolar Contributions of the Second Harmonic Generation from Silver and Gold Nanoparticles," J. Phys. Chem. C **111**(26), 9044–9048 (2007).
53. T. Stolt, J. Kim, S. Héron, A. Vesala, Y. Yang, J. Mun, M. Kim, M. J. Huttunen, R. Czaplicki, M. Kauranen, J. Rho, and P. Genevet, "Backward phase-matched second-harmonic generation from stacked metasurfaces," Phys. Rev. Lett. **126**(3), 033901 (2021).
54. T. Stolt and M. J. Huttunen, "Broadband frequency conversion of ultrashort pulses using high-q metasurface cavities," arXiv preprint 2110.13486 (2021).
55. M. J. Huttunen, P. Rasekh, R. W. Boyd, and K. Dolgaleva, "Using surface lattice resonances to engineer nonlinear optical processes in metal nanoparticle arrays," Phys. Rev. A **97**(5), 053817 (2018).

PUBLICATION III

Broadband frequency conversion of ultrashort pulses using high-Q metasurface resonators

Timo Stolt and Mikko J. Huttunen

New Journal of Physics 24.2 (2022), p. 025004
DOI: 10.1088/1367-2630/ac4a14

PAPER • **OPEN ACCESS**

Broadband frequency conversion of ultrashort pulses using high-*Q* metasurface resonators

To cite this article: Timo Stolt and Mikko J Huttunen 2022 *New J. Phys.* **24** 025004

New Journal of Physics
The open access journal at the forefront of physics

Deutsche Physikalische Gesellschaft DPG
IOP Institute of Physics

Published in partnership with: Deutsche Physikalische Gesellschaft and the Institute of Physics

OPEN ACCESS

RECEIVED
27 October 2021

REVISED
20 December 2021

ACCEPTED FOR PUBLICATION
11 January 2022

PUBLISHED
9 February 2022

PAPER

Broadband frequency conversion of ultrashort pulses using high-*Q* metasurface resonators

Timo Stolt and Mikko J Huttunen*

Photonics Laboratory, Physics Unit, Tampere University, FI-33014 Tampere, Finland
* Author to whom any correspondence should be addressed.

E-mail: mikko.huttunen@tuni.fi

Keywords: nonlinear optics, metasurfaces, surface lattice resonance, plasmonics, frequency conversion

Abstract

Frequency conversion of light can be dramatically enhanced using high quality factor (*Q*-factor) resonator. Unfortunately, the achievable conversion efficiencies and conversion bandwidths are fundamentally limited by the time–bandwidth limit of the resonator, restricting their use in frequency conversion of ultrashort pulses. Here, we propose and numerically demonstrate sum-frequency generation based frequency conversion using a metasurface-based resonator configuration that could overcome this limitation. The proposed experimental configuration takes use of the spatially dispersive responses of periodic metasurfaces supporting collective surface lattice resonances (SLRs), and can be utilized for broadband frequency conversion of ultrashort pulses. We investigate a plasmonic metasurface, supporting a high-*Q* SLR ($Q = 500$, linewidth of 2 nm) centered near 1000 nm, and demonstrate ∼1000-fold enhancements of nonlinear signals. Furthermore, we demonstrate broadband frequency conversion with a pump conversion bandwidth reaching 75 nm, a value that greatly surpasses the linewidth of the studied resonator. Our work opens new avenues to utilize high-*Q* metasurfaces for broadband nonlinear frequency conversion.

Since the construction of the first laser in 1960, lasers have been the most common instruments to generate intense, coherent, monochromatic, and directional light [1]. When applying specific techniques, such as *Q*-switching and mode-locking, lasers can be used to generate ultrashort pulses with extremely high peak intensities and pulse durations down to a few femtoseconds. A major drawback of ultrashort pulse lasers is the lack of tunability. Visible and infrared spectral regions are commonly accessed by utilizing nonlinear frequency conversion resulting from nonlinear processes, such as second-harmonic generation (SHG), sum-frequency generation (SFG), or difference-frequency generation (DFG) [2]. Unfortunately, nonlinear processes are, by their nature, extremely inefficient. Conventional nonlinear optical devices overcome this drawback by utilizing phase-matching techniques and optical resonators [2]. Even though these techniques solve the efficiency problem, their operation bandwidths are often quite narrow, restricting their use in frequency conversion of ultrashort pulses with broad spectral features. This trade-off between conversion efficiency and bandwidth can be solved using adiabatic frequency conversion [3, 4]. However, such techniques rely on long propagation lengths and complicated phase-matching schemes in the nonlinear medium, motivating to seek for alternative approaches.

Recent progress in the fabrication of nanostructures has enabled the development of a novel material class called metamaterials [5]. They are artificial structures consisting of nanoscale building blocks such as nanoparticles (NPs) and gratings. Interestingly, the optical properties of metamaterials can be engineered by tuning the properties of the building blocks, such as their size and shape, during the fabrication process. As a result, metamaterials can exhibit exotic properties, such as negative index of refraction, epsilon-near-zero behavior at optical frequencies, and nanoscale phase-engineering capabilities [6–9].

Plasmonic metasurfaces consisting of metallic NPs have recently shown the potential for enhancing nonlinear processes in nanoscale structures [10]. Metal NPs exhibit collective oscillations of the conduction

electrons giving rise to localized surface plasmon resonances (LSPRs) [11], which result in an increased local field near the NP, subsequently enhancing the nonlinear response [12–18]. However, LSPRs are associated with low quality factors (Q-factors, $Q < 10$) due to the high ohmic losses associated with plasmon resonances. Fortunately, periodically arranged NPs exhibit surface lattice resonances (SLRs) [19, 20], that are associated with narrow spectral features and thus of much higher Q-factors ($Q \approx 2300$) than LSPRs [21]. Therefore, SLRs can result in dramatic local-field enhancements and consequent enhancement of nonlinear responses [22–24].

Despite the potential of utilizing SLR-based metasurface resonators for frequency conversion, their behavior is restricted by the time–bandwidth limit associated with optical resonators [25]. Further enhancement of the local fields present near the NPs by designing SLRs with Q-factors will simultaneously limit their use to frequency conversion of spectrally broad laser sources [21]. Therefore, use of high-Q metasurfaces is seemingly restricted to spectrally narrow laser sources and subsequent nonlinear applications.

In this work, we propose an experimental configuration to achieve broadband frequency conversion with a single plasmonic metasurface supporting a high-Q SLR resonator ($Q \approx 500$, center wavelength 1002 nm, linewidth of 2 nm). The proposed setup utilizes a temporal-focusing scheme that first separates an incident broadband laser beam into separate spectral components that interact nonlinearly with the metasurface. The spatial dispersion of SLRs allows us to couple these different spectral components of the incident beam, arriving at the metasurface at different incidence angles, optimally with the SLR of the metasurface. After the nonlinear interaction, the generated signal frequency components are then combined to form the broadband output beam. Effectively, the use of the proposed scheme results in a broadband enhancement of SHG and SFG processes. We numerically show resonance-enhanced SFG exhibiting a pump conversion bandwidth of $\Delta\lambda \approx 75$ nm (1020–1095 nm), a value greatly exceeding the 2 nm linewidth of the SLR.

1. Theory

The nonlinear response of a metasurface can be evaluated using nonlinear scattering theory [26, 27]. Using this approach, the SFG response of a metasurface depends on the mode overlap between local fields at the fundamental frequencies $\mathbf{E}(\omega_1, \mathbf{r})$ and $\mathbf{E}(\omega_2, \mathbf{r})$, and at the SFG frequency $\mathbf{E}(\omega_3, \mathbf{r})$ [28–30]. Consequently, the detected far-field SFG emission $\mathbf{E}_{\text{det}}$ ($\omega_3 = \omega_1 + \omega_2$) can be estimated using the Lorentz reciprocity theorem as [26]

$$\mathbf{E}_{\text{det}}(\omega_3 = \omega_1 + \omega_2) \propto \iiint_V \chi^{(2)}(\omega_3; \omega_1, \omega_2, \mathbf{r}) : \mathbf{E}(\omega_1, \mathbf{r})\mathbf{E}(\omega_2, \mathbf{r})\mathbf{E}^*(\omega_3, \mathbf{r})\, \mathrm{d}V, \tag{1}$$

where integration is performed over metasurface unit cell volume V, and $\chi^{(2)}(\omega_3;\ \omega_1, \omega_2, \mathbf{r})$ is the nonlinear susceptibility tensor. For SHG, where $\omega_1 = \omega_2 = \omega$ and $\omega_3 = 2\omega$, equation (1) is written as

$$\mathbf{E}_{\text{det}}(2\omega) \propto \iiint_V \chi^{(2)}(2\omega; \omega, \omega, \mathbf{r}) : \mathbf{E}^2(\omega, \mathbf{r})\mathbf{E}^*(2\omega, \mathbf{r})\, \mathrm{d}V. \tag{2}$$

The local fields $\mathbf{E}(\omega_i, \mathbf{r})$ consist of the incident laser field $\mathbf{E}_{\text{inc}}(\mathbf{k}_i, \omega_i)$, where $\mathbf{k}_i$ is the laser field wave vector, and of the field scattered by the nanoparticles in the metasurface $\mathbf{E}_{\text{scat}}(\omega_i)$. In other words, $\mathbf{E}(\omega_i) = \mathbf{E}_{\text{inc}}(\mathbf{k}_i, \omega_i) + \mathbf{E}_{\text{scat}}(\omega_i)$. Consequently, the local fields can be increased either by increasing the incident laser field amplitude, or by utilizing resonances, such as LSPRs or SLRs, that boost the scattered fields $\mathbf{E}_{\text{scat}}(\omega_i)$ [31].

In this work, we focus on SLRs that occur in periodic arrays of metallic NPs for two different reasons. First, SLRs can be associated with very high Q-factors and consequently also with considerable local-field enhancements. Second, the collective nature of SLRs makes them spatially dispersive, which can be utilized to realize broadband frequency conversion.

Collective SLRs result from radiative coupling between periodically arranged NPs. This coupling is strong near the Rayleigh anomaly wavelength, which for the first-order diffraction mode is given by [32]:

$$\lambda_{\pm 1} = P\,(n \mp \sin\,\theta)\,, \tag{3}$$

where P is the array periodicity, n is the refractive index of the surrounding material, and θ is the incidence angle in air, i.e. above the superstate material. Looking at equation (3), we see that the SLRs associated with diffraction orders ± 1 occur at the same wavelength when $\theta = 0^\circ$. When $\theta \neq 0^\circ$, these two SLRs shift away from this wavelength, and from each other. This angle-dependence of SLRs provide simple means to tune the central wavelength of the resonance. We note that use of LSPRs does not provide similar tunability.

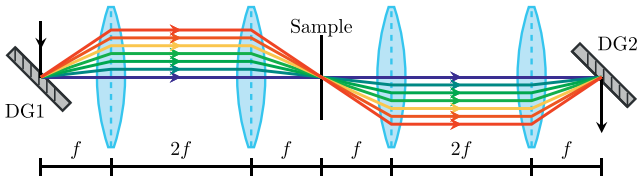

Figure 1. Proposed setup for broadband frequency conversion using high-Q metasurfaces. The incident pulse is separated into its spectral components using the first diffraction grating (DG1). A 4f-correlator is then used to guide the spectral components into the metasurface, where the incidence angles θ of the spectral components depend on the frequency ω. At the metasurface, the pump frequencies are up-converted with the process of sum-frequency generation. After the frequency conversion, the spectral components of the nonlinear signal are combined using a second 4f-correlator and a subsequent diffraction grating (DG2).

Despite the potential of utilizing high-Q SLRs for enhancing light–matter interaction taking place in the metasurface, similar to all optical resonators their behavior is restricted by the time–bandwidth limit. An increase in the Q-factor of the resonator is necessarily associated with a reduction of the operation bandwidth. This limit seems to particularly restrict many nonlinear applications utilizing ultrashort laser pulses with pulse durations τ_p of 10–100 fs and linewidths $\Delta\lambda_L$ of 10–100 nm. Typical high-Q SLRs have linewidths $\Delta\lambda_{SLR} \sim 1$ nm, suggesting their use with fs lasers to be inefficient. For example, when using a laser with $\tau_p \approx 200$ fs and $\Delta\lambda_L \approx 10$ nm, only ~10% of the laser power can be coupled into an SLR mode with a linewidth $\Delta\lambda_{SLR} = 1$ nm. To overcome this problem, we propose an experimental scheme that utilizes diffractive optical elements and the angle-dependent responses of SLRs (see figure 1).

The scheme for broadband frequency conversion using the setup shown in figure 1 consists of five steps and resembles closely a temporal focusing scheme [33, 34]. First, the incident laser pulse is split into its spectral components by a diffraction grating. The laser beam spot at the diffraction grating is then imaged using two lenses, acting as a 4f-correlator, onto the sample plane. Thus, the different spectral components of the input beam arrive to the sample at different angles of incidence θ. With a properly selected diffraction grating and a set of lenses, the incidence angle of a given frequency component can be made to match with the resonance wavelength of the tilted SLR (see equation (3)). Therefore, it becomes possible to couple an incident broadband source more efficiently into a high-Q metasurface and subsequently boost the broadband SFG response. Finally, using another pair of lenses acting as a 4f-correlator, the SFG signal component beams are imaged onto a second diffraction grating. With a proper selection of these components, the spectral components of the SFG signal are combined with the second diffraction grating completing the broadband conversion process.

2. Results and discussion

In this work, we used finite-difference time-domain (FDTD) method to simulate the optical response of a metasurface consisting of V-shaped aluminum NPs. In order to ensure homogeneous surroundings required for SLRs, the NPs were embedded inside homogeneous glass surroundings with refractive index $n = 1.51$. The NPs had arm length $L = 120$ nm, arm width $w = 70$ nm, and thickness $d = 30$ nm, resulting in LSPRs near 570 nm for y-polarized light (see figure 2). In order to have our metasurface exhibit y-polarized SLRs near 1000 nm, we set $p_x = 660$ nm. The other lattice constant was set to a slightly smaller value of $p_y = 400$ nm to increase the NP density without significant impact to the y-polarized SLRs. With these parameters and under illumination at normal incidence, the investigated metasurface exhibited an SLR at 1002 nm for y-polarized light. Here, linewidth of the SLRs was $\Delta\lambda_{SLR} \approx 2$ nm corresponding to $Q = 500$.

Next, we simulated the transmittance of the sample with the incidence angle θ varying from 0° to 9°. Again, we considered y-polarized light. By changing θ, SLR peak was split into two peaks, which moved further from 1002 nm as θ increased (see figure 2 (b)). At $\theta = 9°$, SLRs occurred at 896 nm and 1100 nm. For the NP geometry considered in this work, the Q-factors and the local-field enhancement factors associated with the shorter-wavelength SLRs were found to be significantly lower than for those of the longer-wavelength SLRs. Therefore, in what follows, we chose to focus only on the longer-wavelength SLRs occurring between 1000–1100 nm.

In order to verify that the local fields are accordingly enhanced in the presence of high-Q SLRs, we also present the simulated local field distributions (see figure 3). When using y-polarized incident light oscillating at the SLR peak wavelength, the light–matter interaction results in local-field hot spots near the corners of the NPs that point along the y-direction. Although the overall structure of the local-field

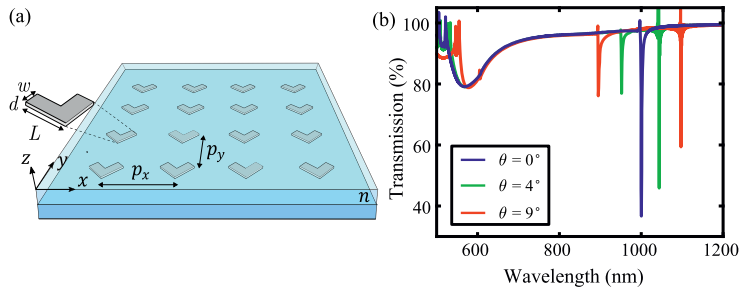

Figure 2. (a) The simulated metasurface consisting of V-shaped aluminum NPs arranged on rectangular lattice in homogeneous glass surroundings ($n = 1.51$). Here, the NP and lattice parameters are $L = 120$ nm, $w = 70$ nm, $d = 30$ nm, $p_x = 660$ nm, and $p_y = 400$ nm. (b) With these parameters and y-polarized incident light, the metasurface exhibits a broad LSPR near 570 nm and a much narrower SLR at 1002 nm. The simulated transmission spectra shows how the peak wavelengths of the splitted SLR near 1000 nm shift from the normal incidence resonance wavelength (blue line), when the incidence angle changes. With $\theta = 9°$ (red line) two SLRs form at 896 nm and 1100 nm. In this work, we chose to utilize only the SLRs occurring at longer wavelengths (>1000 nm), because their Q-factors are larger than those of the shorter-wavelength SLRs (<1000 nm).

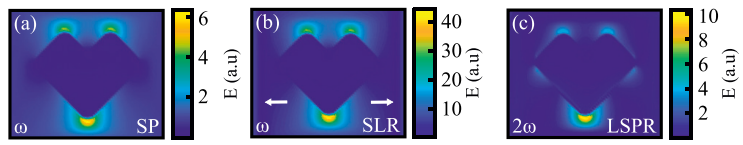

Figure 3. (a) Interaction with y-polarized light induces local-field hot spots on the edges of single particles (SP). (b) When nanoparticles are arranged in an array and the incident light is set to the SLR wavelength of 1002 nm, the local-field enhancement becomes dramatically larger than in the SP case. The collective nature of SLRs causes the field to drop symmetrically along the direction inter-particle coupling (white arrows). (c) At the second-harmonic wavelength of 501 nm, the local fields are enhanced due to the presence of a LSPR centered at 570 nm. In total, the mode overlap between $E(\omega, \mathbf{r})$ and $E(2\omega, \mathbf{r})$ result in enhanced SHG and SFG responses.

distribution associated with a single NP (figure 3(a)) is not markedly affected when the NPs are arranged periodically giving rise to the high-Q SLR (figure 3(b)), the field amplitudes are. Their intensity dramatically increases, when we arrange particles into an array and couple light into the SLR mode (figure 3(b)). Clear local-field hot spots also form, when the wavelength of the incident light is close to the LSPR wavelength (figure 3(c)).

Next, we used the simulated field profiles (figure 3) to calculate mode-overlap integrals associated with the nonlinear scattering theory (see equations (1) and (2)). Here, we assumed that the nonlinear response of the plasmonic NPs is dominated by their surface response. Specifically, we only considered the susceptibility component perpendicular to the surface of the NP ($\chi^{(2)}_{\perp\perp\perp}$), and the respective field components [35]. Furthermore, the incident pump and the generated nonlinear signal fields were assumed to be polarized along the y-direction. First, we estimated how efficiently narrowband laser pulses ($\Delta\lambda_L \approx 1$ nm, FWHM) at different wavelengths between 1000–1100 nm can be converted to SHG wavelengths between 500–550 nm (see figure 4). Laser pulses at different wavelengths were guided on the metasurface at different incidence angles (0°–9°), resulting in enhanced SHG due to occurring SLRs. As expected by looking at equation (3), different incident wavelengths can be made resonant with the metasurface simply by changing the angle of incidence. When compared against the off-resonance situation (5 nm away from the SLR wavelength), the calculated SHG intensities were enhanced by factors in the range of 500 (8° angle of incidence) to 1800 (3° angle of incidence). The differences between SHG signals at different incident angles result from small differences in the pump and second-harmonic field distributions that affect the overall SHG signal levels due to changes in the mode-overlap calculations. Particularly, the estimated SHG signals were found to be very sensitive to the changes in the second-harmonic field.

Next, we consider the frequency conversion of a broadband laser pulse centered at a wavelength of 1050 nm having a bandwidth of $\Delta\lambda_L = 100$ nm (FWHM). First, we consider the situation where the entire pulse arrives at the metasurface at one incidence angle (see figure 5(a)). For simplicity, we assume that each spectral component of the broad laser pulse arrived at the metasurface simultaneously. Thus, the spectral

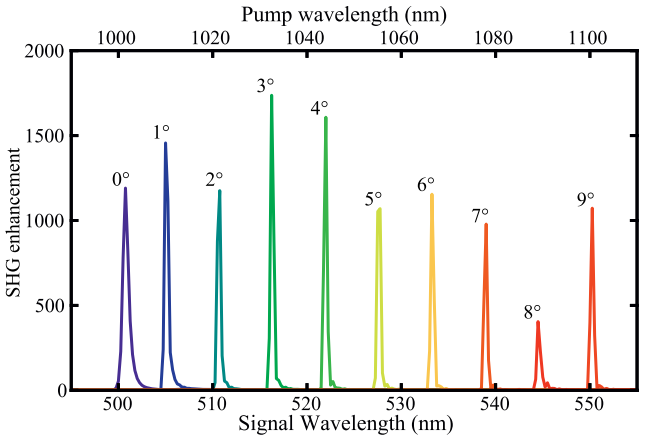

Figure 4. Tunable frequency conversion of narrowband laser pulses ($\Delta\lambda_L \approx 1$ nm) via angle-dependent SHG. The SHG signals are normalized to the non-resonant case (5 nm off the SLR wavelength).

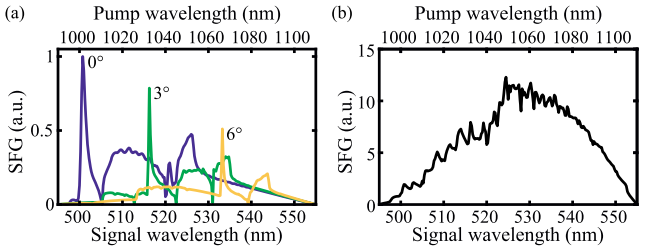

Figure 5. Frequency conversion of a broadband laser source ($\Delta\lambda_L = 100$ nm) via SFG in an SLR-supporting metasurface ($\Delta\lambda_{SLR} \approx 2$ nm corresponding to $Q = 500$). (a) SFG responses of studied metasurface without the proposed scheme (see figure 1). The laser pulse is incident on the metasurface at a single angle of incidence. Thus, the laser pulse arriving either at 0° (blue), 3° (green), or 6° (yellow) will be most efficiently converted only near the corresponding SLR wavelengths 1002 nm, 1032 nm, or 1067 nm, respectively. (b) The overall SFG response of the studied metasurface using the proposed scheme. Through the SLR-induced enhancement, all spectral components interact efficiently, resulting in a broadband frequency conversion with signal bandwidth $\Delta\lambda_{SFG} \approx 40$ nm (pump conversion bandwidth $\Delta\lambda \approx 75$ nm, 1020–1095 nm). All signals are normalized to the maximum SFG signal for the case where all spectral components arrive at $\theta = 0°$ (blue line).

components could interact with each other, resulting in numerous SFG signal wavelengths. However, efficient SFG occurs only when both pump fields are at the occurring SLR wavelength. Therefore, pumping at either 0°, 3°, or 6° results in strongest SFG emission at 500 nm, 516 nm, and 533 nm, respectively. At these strongest signal wavelengths, the SFG emission is enhanced by a factor of ~ 1000 when compared to the non-resonant situation. There are also weaker and broader emission peaks at longer wavelengths, for example, around 510 nm for illumination at $\theta = 0°$. These peaks arise from SFG processes where one of the pump fields is at the SLR wavelength while the other pump field is at an off-resonant wavelength.

Finally, we consider SFG emission for the situation with the proposed temporal focusing scheme (see figure 5(b)). We assume that the pulse is separated into 10 different spectral components each with a linewidth of 5 nm and constant and equal field amplitudes. Again, the spectral components arrive at the metasurface simultaneously, allowing them to interact with each other. This time, each component arrives at the metasurface at different incidence angles θ allowing each component to couple resonantly with an optimal SLR mode (see figure 2(b)). The occurring SLRs therefore enhanced the local fields at all the considered pump wavelengths, resulting in efficient SFG for numerous signal wavelengths. Remarkably, the numerous interactions combine to produce even stronger signal due to their cumulative nature. For example, the SFG process with the pump wavelengths $\lambda_1 = 1002$ nm and $\lambda_2 = 1100$ nm results in a nonlinear signal at the wavelength close to one gained with the process where $\lambda_1 = \lambda_2 = 1052$ nm, resulting

in stronger combined nonlinear emission near 525 nm. Due to the cumulative nature of the total SFG signal, the total SFG response is enhanced by an additional factor of 10, when compared to the calculated SFG spectra performed for individual angles of incidence. More importantly, the total SFG signal has a conversion bandwidth of $\Delta\lambda_{SFG} \approx 40$ nm (pump conversion bandwidth $\Delta\lambda \approx 75$ nm, 1020–1095 nm), indicating simultaneous resonance-enhanced and broadband frequency conversion of the initial laser pulse with $\Delta\lambda_L = 100$ nm. This conversion bandwidth $\Delta\lambda$ is almost 40 times broader than the linewidth $\Delta\lambda_{SLR} \approx 2$ nm associated with the normally incident SLR, suggesting a way to surpass the time–bandwidth limit by optimizing the way light is coupled into SLR-supporting metasurfaces.

We note that the simulated SFG emission spectrum would be narrower if we assumed Gaussian distribution for the incident broadband pulse. The spectral components at the pulse edges would have smaller amplitudes, reducing their nonlinear interaction strength and decreasing the SFG near 500 nm and 550 nm. Another factor that could considerably affect the SFG emission spectrum would be any possible chirp of the incident laser pulse. In that case, the different spectral components would not arrive at the metasurface simultaneously and could not interact efficiently with each other. The lack of interaction would limit the nonlinear processes to SHG, resulting in a nonlinear emission spectrum similar to one shown in figure 4. We note that even with these two limiting factors, the resulting overall nonlinear response would overcome the time–bandwidth limit associated with narrow resonances, such as SLRs.

The results above illustrate how our method results in broadband frequency conversion of light through the process of SFG. We believe that the method can be generalized to be applicable also for other nonlinear processes. For example, utilizing our approach for DFG or third-harmonic generation (THG), a broadband generation of THz or ultraviolet laser pulses could be achieved. We also note that the proposed method can be expected to be quite relevant when nonlinear responses of SLR-based metasurfaces with record-high Q-factors are investigated and utilized for frequency conversion applications [21].

As a whole, this numerical work proposes a novel methodology for broadband frequency conversion of light using metasurface-based high-Q resonators ($Q \approx 500$). Because the time–bandwidth limit restricts the conversion bandwidth and the achievable efficiency of resonant nonlinear devices, the proposed methodology could provide new possibilities for metasurface-based broadband frequency conversion of light.

3. Conclusions

To conclude, we have demonstrated a method for a broadband frequency conversion using a metasurface supporting high-Q SLRs ($Q \approx 500$). In our proposed setup design, different wavelength components are separated and guided on an SLR-supporting metasurface at different incident angles. Due to the spatial dispersion of SLRs, the scheme results in resonance-enhanced and broadband SFG response. Thus, our method is suitable for frequency conversion of both broadband laser pulses and of wavelength-tunable lasers with narrower spectral features. We have shown how the frequency conversion of an ultrashort laser pulse with a linewidth of 100 nm can be resonantly enhanced ($\sim$ 1000-fold) when comparing against non-resonant nonlinear response. Furthermore, a pump conversion bandwidth of $\Delta\lambda \approx 75$ nm is achieved, exceeding by almost a factor of 40 the linewidth (2 nm) of the SLR resonator. This result suggests a way to surpass the time–bandwidth limit associated with resonators by optimizing the way light is coupled into SLR-supporting metasurfaces. In addition to SFG and SHG, our method could be generalized for other frequency conversion processes, such as DFG and THG. Overall, our work opens new possibilities to perform broadband frequency conversion of light by utilizing high-Q metasurface resonators.

Acknowledgments

We acknowledge the support of the Academy of Finland (Grant No. 308596) and the Flagship of Photonics Research and Innovation (PREIN) funded by the Academy of Finland (Grant No. 320165). TS also acknowledges Jenny and Antti Wihuri Foundation for their PhD Grant.

Data availability statement

The data that support the findings of this study are available upon reasonable request from the authors.

Appendix A. Simulation methods

Linear FDTD simulations. The FDTD simulations were performed using lumerical FDTD solutions simulation software. We simulated the transmission spectra and local-field distribution for aluminum nanoparticles in homogeneous surroundings ($n = 1.51$). To investigate a periodic structure, we used periodic boundary conditions along the metasurface axes (x- and y-axes). The perfect-matching-layer (PML) conditions were used at the boundary along the initial propagation direction (z-axis). The PML profile was optimized for oblique-angle simulations. For simulations with $\theta \neq 0°$, we used the broadband fixed angle source technique (BFAST).

Nonlinear scattering theory. The nonlinear responses of our metasurface was evaluated using the presented nonlinear scattering theory and Lorentz reciprocity theorem [26, 27]. For simplicity, only the surface nonlinearities associated with metallic aluminum were considered. Furthermore, the component $\chi_{\perp\perp\perp}$ (all field components are perpendicular to the surface of the metal) was assumed to be the only non-zero susceptibility component describing the nonlinearities of the surfaces of the aluminum nanoparticles. We are not aware of studies reporting effective surface susceptibility tensor components for aluminum. Therefore, in this work the strength of the $\chi_{\perp\perp\perp}$ was set to unity, forcing also us to restrict to relative calculations. The calculations were performed with Matlab. There we used the local-field profiles simulated with FDTD as input values.

ORCID iDs

Timo Stolt https://orcid.org/0000-0002-0047-8536
Mikko J Huttunen https://orcid.org/0000-0002-0208-4004

References

[1] Maiman T H 1960 *Nature* **187** 493
[2] Boyd R W 2020 *Nonlinear Optics* 4th edn (New York: Academic) p 578
[3] Suchowski H, Oron D, Arie A and Silberberg Y 2008 *Phys. Rev.* A **78** 063821
[4] Suchowski H, Bruner B D, Ganany-Padowicz A, Juwiler I, Arie A and Silberberg Y 2011 *Appl. Phys.* B **105** 697
[5] Soukoulis C M and Wegener M 2011 *Nat. Photon.* **5** 523
[6] Klein M W, Enkrich C, Wegener M and Linden S 2006 *Science* **313** 502
[7] Alù A, Silveirinha M G, Salandrino A and Engheta N 2007 *Phys. Rev.* B **75** 155410
[8] Zhang S, Park Y-S, Li J, Lu X, Zhan W and Zhang X 2009 *Phys. Rev. Lett.* **102** 023901
[9] Genevet P, Capasso F, Aieta F, Khorasaninejad M and Devlin R 2017 *Optica* **4** 139
[10] Kauranen M and Zayats A V 2012 *Nat. Photon.* **6** 737
[11] Maier S A 2007 *Plasmonics: Fundamentals and Applications* (Berlin: Springer)
[12] Lapine M, Shadrivov I V and Kivshar Y S 2014 *Rev. Mod. Phys.* **86** 1093
[13] Butet J, Brevet P-F and Martin O J F 2015 *ACS Nano* **9** 10545
[14] Li G, Zhang S and Zentgraf T 2017 *Nat. Rev. Mater.* **2** 17010
[15] Li G *et al* 2017 *Nano Lett.* **17** 7974
[16] Rahimi E and Gordon R 2018 *Adv. Opt. Mater.* **6** 1
[17] Huttunen M J, Czaplicki R and Kauranen M 2019 *J. Nonlinear Opt. Phys. Mater.* **28** 1950001
[18] Wu T *et al* 2019 *Adv. Opt. Mater.* **7** 1900905
[19] Kravets V G, Kabashin A V, Barnes W L and Grigorenko A N 2018 *Chem. Rev.* **118** 5912
[20] Utyushev A D, Zakomirnyi V I and Rasskazov I L 2021 *Rev. Phys.* **6** 100051
[21] Bin-Alam M S *et al* 2021 *Nat. Commun.* **12** 974
[22] Michaeli L, Keren-Zur S, Avayu O, Suchowski H and Ellenbogen T 2017 *Phys. Rev. Lett.* **118** 243904
[23] Hooper D C, Kuppe C, Wang D, Wang W, Guan J, Odom T W and Valev V K 2018 *Nano Lett.* **19** 165
[24] Huttunen M J, Reshef O, Stolt T, Dolgaleva K, Boyd R W and Kauranen M 2019 *J. Opt. Soc. Am.* B **36** E30
[25] Fan S, Suh W and Joannopoulos J D 2003 *J. Opt. Soc. Am.* A **20** 569
[26] Roke S, Bonn M and Petukhov A V 2004 *Phys. Rev.* B **70** 115106
[27] O'Brien K, Suchowski H, Rho J, Salandrino A, Kante B, Yin X and Zhang X 2015 *Nat. Mater.* **14** 379
[28] Wang F, Martinson A B F and Harutyunyan H 2017 *ACS Photonics* **4** 1188
[29] Wu T, Luo Y, Maier S A and Wei L 2019 *Phys. Rev. Appl.* **11** 014049
[30] Noor A, Damodaran A R, Lee I-H, Maier S A, Oh S-H and Ciracì C 2020 *ACS Photonics* **7** 3333
[31] Huttunen M J, Dolgaleva K, Törmä P and Boyd R W 2016 *Opt. Express* **24** 28279
[32] Khlopin D *et al* 2017 *J. Opt. Soc. Am.* B **34** 691
[33] Oron D, Tal E and Silberberg Y 2005 *Opt. Express* **13** 1468
[34] Block E, Greco M, Vitek D, Masihzadeh O, Ammar D A, Kahook M Y, Mandava N, Durfee C and Squier J 2013 *Biomed. Opt. Express* **4** 831
[35] Wang F X, Rodríguez F J, Albers W M, Ahorinta R, Sipe J E and Kauranen M 2009 *Phys. Rev.* B **80** 4